

Use Authorization

In presenting this thesis in partial fulfillment of the requirements for an advanced degree at Idaho State University, I agree that the Library shall make it freely available for inspection. I further state that permission for extensive copying of my thesis for scholarly purposes may be granted by the Dean of the Graduate School, Dean of my academic division, or by the University Librarian. It is understood that any copying or publication of this thesis for financial gain shall not be allowed without my written permission.

Signature

Date

Computational and Experimental Analysis
for a Cross-flow Plate Type Oval-Twisted Tube Heat Exchanger

by

Kyle Schroeder

A thesis
submitted in partial fulfillment
of the requirements for the degree of
Master of Science in the Department of Nuclear Engineering
Idaho State University
Summer 2023

To the Graduate Faculty:

The members of the committee appointed to examine the thesis of Kyle Schroeder find it satisfactory and recommend that it be accepted.

Amir Ali, Ph.D.

Major Advisor, Committee Chair

Piyush Sabharwall, Ph.D.

Committee Member

Anish Sebastian, Ph.D.

Graduate Faculty Representative

Acknowledgements:

I would like to express my gratitude to my advisor Amir Ali, Ph.D., for his indispensable counsel and support throughout my master's program, his expertise and encouragement never failed.

A special thanks to the Center for Advanced Energies (CAES) Consortium for providing the facilities in which to construct the infrastructure required to complete these experiments.

I sincerely appreciate Piyush Sabharwall, Ph.D., for his sponsorship which allowed me to use the high performance computing (HPC) capabilities at the Idaho National Laboratory. Without this support the obstacles present in this thesis would have truly felt insurmountable.

I would also like to thank Anish Sebastian, Ph.D., for serving on my thesis committee and for providing helpful feedback and suggestions.

Of course the person I would like to thank the most is my beloved wife Kailey Schroeder, she certainly bore the brunt of the burden this thesis presented, especially at the end when she brought a new child into the world. She truly has felt, with many sleepless nights and tiresome days the exhaustive hours which this thesis has cost. I am indebted to her for her wonderful sacrifice during my constant abdication.

TABLE OF CONTENTS

List of Figures	xv
List of Tables	xvi
List of Abbreviations and Symbols	xvii
Abstract	xxii
Chapter I: Introduction	1
1.1 Heat Exchanger Technologies	1
1.1.1 Active and Passive Heat Transfer Amplification Methods	3
1.1.2 Twisted Tube Heat Exchangers	6
1.2 Numerical Methodology	8
1.2.1 Flow Imbalance	9
1.2.2 Number of Transfer Units	9
1.2.3 Entropy	10
1.3 The Role of Simulations	10
1.4 Project Objectives	11
1.5 Significance	12
Chapter II: Numerical Analysis of Novel Plate Type Heat Exchanger	13
2.1 Thermophysical Properties	13
2.2 Sensitivity Study	13
2.3 Model Selection	16
2.4 Parameter Selection and Case Outline	17
2.5 CFD Results	20
2.5.1 Imbalanced Flow	20
2.5.2 Balanced Flow	20

2.5.3	Entropy Generation	25
2.5.4	Number of Transfer Units	26
2.5.5	Temperature Distribution	28
Chapter III: Experimental Facility		34
3.1	Design	34
3.2	Component Description	34
3.3	Construction	34
3.4	Calibration	36
3.4.1	Standard Operating Procedures	40
3.5	Uncertainty Analysis	43
3.5.1	Data Acquisition - LabView	46
Chapter IV: Experimental Results		49
4.1	Fabrication	49
4.2	Design Dimensions	54
4.3	Installation	54
4.4	Operation Plots	57
4.5	Test Parameters	60
4.6	Results	61
4.6.1	Imbalanced Flow	61
4.6.2	Balanced Flow	62
4.6.3	Entropy Generation	66
4.6.4	Number of Transfer Units	68
4.6.5	Simulation and Experiment Comparison	69
Chapter V: Conclusion and Future Work		71
References		74

Appendix A: Mass Balance Data	82
Appendix B: Flowrate Approximation Code	84
Appendix C: Simulation and Experiment Comparison Plots	89

LIST OF FIGURES

Figure 1	Various types of shells for a shell and tube style HX. a) One pass shell, b) split flow, c) divided flow, d) two pass shell with baffle, e) double split flow, and f) cross flow	2
Figure 2	A generalized schematic of a plate type HX indicating the flow paths for hot and cold fluids provided by Alfa Laval [4].	3
Figure 3	Measuring the inlet and outlet flow rates of each flow channel indicates that the conservation of mass flow rate is acceptable measuring with the highest discrepancy of 3% as shown in Table 4 and Appendix A Tables 6-8.	19
Figure 4	With the cold side fixed at 0.03149 kg/s ($\approx 0.5 \text{ GPM}$) the oval twisted HX displays approximately 24% higher heat transfer than the circular counterpart.	21
Figure 5	With the cold side fixed at 0.2519 kg/s ($\approx 4 \text{ GPM}$) increases of 36% and 48% were experienced at the lowest and highest simulated flow rates respectively.	21
Figure 6	With the cold side fixed at 0.03149 kg/s ($\approx 0.5 \text{ GPM}$) the oval twisted HX displays Nu increases averaging 26% and 32% for the hot and cold sides respectively.	22
Figure 7	With the cold side fixed at 0.2519 kg/s ($\approx 4 \text{ GPM}$) Nu increases between 41% and 54% are experienced with the highest increases occurring in the cold side of the HX at high flow rates.	22

Figure 8	The wattage on the hot and cold sides of the HX is nearly identical. The average wattage for the oval twisted HX is approximately 18% - 33% higher when compared to the circular counterpart.	23
Figure 9	The difference in Nu on the hold and cold sides is due to differences in inlet thermal conductivity and heat transfer coefficient h. The increase in Nu number for the oval twisted HX compared to the circular is between 25% and 35%.	24
Figure 10	The overall heat transfer coefficient for the oval twisted type heat exchanger is an average of 25% higher at the lowest flow rate and 35% higher at the maximum flow rate.	25
Figure 11	The performance increase for the oval heat exchanger compared to the circular HX shows greater than 1 across all simulated flow parameters for balanced flow conditions.	26
Figure 12	Entropy generation number for the circular flow channel type HX shows higher values while effectiveness shows lower values when compared to the oval type HX in Figure 13, for $T_{hi}/T_{ci}=1.2$	27
Figure 13	The entropy generation number for the oval twisted type HX is lesser for both balanced and imbalanced flow parameters while simultaneously increasing effectiveness , for $T_{hi}/T_{ci}=1.2$	27
Figure 14	The NTU vs Effectiveness curves for the circular cross-section HX shows values shifted down 19% – 35% and to the left 25% – 35% when compared to an oval twisted counterpart.	29
Figure 15	The NTU vs Effectiveness curves for the oval cross-section HX shows values shifted up 19% – 35% and to the right 25% – 35% when compared to a circular flow channel counterpart.	29
Figure 16	An isometric view indicating where the temperature profiles are collected for the hot and cold sides of the HX.	30

Figure 17	The locations where the temperature profiles are measured at the mid-planes of the HX and across the center-lines of the flow regions with the cold side (top) and the hot side (bottom).	30
Figure 18	The temperature profile of the cold side of the HX with flow rates for the hot and cold side fixed at 0.03149 kg/s ($\approx 0.5 \text{ GPM}$). The temperature distribution for the oval and circular designs is very similar.	31
Figure 19	The temperature profile of the hot side of the HX with flow rates for the hot and cold side fixed at 0.03149 kg/s ($\approx 0.5 \text{ GPM}$). The amplitude of the temperature distribution slightly less for the oval twisted design, indicating more efficient heat transfer between the solid and fluid regions.	32
Figure 20	The temperature profile of the cold side of the HX with flow rates for the hot and cold sides fixed at 0.2519 kg/s ($\approx 4 \text{ GPM}$). The change in temperature between fluid and solid regions for the oval twisted design is much less than the circular design.	33
Figure 21	The temperature profile of the hot side of the HX with flow rates for the hot and cold side fixed at 0.2519 kg/s ($\approx 4 \text{ GPM}$). The change in temperature between fluid and solid regions for the oval twisted design is much less than the circular design.	33
Figure 22	A simplified schematic of the primary and secondary loop for the intermediate heat exchanger (IHX) test facility.	35
Figure 23	The test facility with certain components highlighted: 1) Expansion Tank, 2) Secondary loop flow meter, 3) Primary loop flow meter, 4) Secondary loop pump, 5) Location of the Secondary loop heat exchanger, 6) Location of the Test section, 7) 30 kW heater, 8) Primary loop pump. . . .	37

Figure 24	The flowmeter mA output vs flowrate trends show that signal noise dominates any measurement below 6 GPM. A different method for obtaining flowrate at these low values must be used.	39
Figure 25	The curves for VFD pump setting vs flowrate for the test facility at room temperature (20 °C) with the Kelvion HX installed as the test section. These curves will change when any modification is done to the facility or the temperature is changed.	41
Figure 26	The user must select desired loop, fluid temperature, and desired flowrate. The program uses calibration data from the hot and cold flowrate measurements to approximate the VFD setting required to operate the loop at the desired flowrate.	42
Figure 27	The maximum error for the temperature range in this study is ± 1 °C for a type T thermocouple measured using a NI-9214 with NI TB-9214 terminal block. The error in measurement above 130°C increases to $\pm 0.75\%$ of the reading.	44
Figure 28	The measurement error for devices read using NI 9207 with NI 9923 terminal block, pressure of the left (a) and flowrate on the right (b).	44
Figure 29	The front panel of the labVIEW program used to view live data for temperature, pressure, flowrate, and various wattages. The user may pause or resume data recording at any time using this panel.	47
Figure 30	The block diagram for the LabVIEW program used to handle the data obtained from the data acquisition hardware. This program reads, manipulates, outputs, and records various data of interest.	48
Figure 31	An isometric view of the entire assembly, the cold side is the top portion while the hot side is the bottom portion.	50

Figure 32	The positive and negative features machined into the parts are toleranced closely and filled with a small amount of sealant prior to assembly to ensure that there is no cross-flow between flow paths.	50
Figure 33	Two heat exchangers are to be fabricated, one with a circular flow path cross section (a) as the baseline, and one with oval twisted flow paths (b).	51
Figure 34	Details showing the marked difference between the circular cross section volume and the oval twisted cross section volume. Both volumes shown are the bottom (hot) fluid volumes.	51
Figure 35	The various components of the circular HX shown, the top volume (a) bottom volume (b), and fully assembled welded circular HX (c).	52
Figure 36	The various components of the oval twisted HX shown, the top volume (a) bottom volume (b), and fully assembled welded oval twisted design HX (c).	53
Figure 37	The outside dimensions for both the circular and oval twisted designs. .	54
Figure 38	The dimensions of the ellipse in the oval twisted design including spacing and arrangement to the top cold fluid volume.	55
Figure 39	The dimensions of the ellipse in the oval twisted design including spacing and arrangement to the bottom hot fluid volume.	55
Figure 40	A view of the top and bottom of the center plate to show the lengths of the flow paths. These lengths are the same for the oval twisted and circular designs.	56
Figure 41	A HX shown installed before insulating (a) and after insulation is applied (b).	57
Figure 42	The calibration curves for the primary and secondary loops at 20 and 80 °C with the circular heat exchanger installed.	58
Figure 43	The calibration curves for the primary and secondary loops at 20 and 80 °C with the oval twisted heat exchanger installed.	59

Figure 44	The difference in wattage between circular and oval twisted geometries is largely unnoticeable when the cold side flow rate is fixed at 0.0315 kg/s ($\approx 0.5 \text{ GPM}$).	61
Figure 45	When the cold side is fixed at 0.252 kg/s ($\approx 4 \text{ GPM}$). The improvement in wattage is drastic with increases between 13.7 and 19.7%.	62
Figure 46	When the cold side is fixed at 0.03149 kg/s the only noticeable difference in wattage occurs when at high hot side flow rates with the circular geometry showing slight improvements of approximately 10.7%.	63
Figure 47	When the cold side is fixed at 0.252 kg/s ($\approx 4 \text{ GPM}$). The improvement in Nu is drastic with increases between 14.9% and 19.2%	63
Figure 48	The difference in wattage between the hot and cold sides of the HX vary drastically with approximately 12% - 31% difference in the oval HX and 20% - 52% difference in the circular geometry.	64
Figure 49	The difference in Nu between the hot and cold sides of the HX vary drastically with approximately 23% - 44% difference in the oval HX and 31% - 67% difference in the circular geometry.	65
Figure 50	The oval twisted HX shows an increase in overall heat transfer coefficient between 15.6% and 25.1% when compared to the circular counterpart.	65
Figure 51	The increase in performance for U, Nu, and q are greater than unity for all cases. The highest performance increase of 1.2 noted here occurs at approximately 0.17 kg/s	66
Figure 52	The entropy generation number for the circular geometry HX follows the correct trend in approaching zero as effectiveness increases though the values presented here are much higher than one instance found in literature.	67
Figure 53	The entropy generation number for the oval twisted HX presents values approximately 24% lower than the circular HX.	68

Figure 54	The effectiveness vs NTU trend follows the appropriate pattern, additionally the effectiveness and NTU for the circular HX are significantly lower than the values for the oval twisted design.	69
Figure 55	The increase in effectiveness for the oval twisted geometry shown here is 9 - 41% greater than circular counterpart. Further it also present NTU values 11 - 48% greater than circular design.	70
Figure 56	The cold side of the HX is fixed at 0.03149 kg/s while the hot side is swept. The predicted wattage and increased performance assumed in the simulation does not match the measured values.	91
Figure 57	The cold side of the HX is fixed at 0.252 kg/s while the hot side is swept across the flow regime. The predicted wattage and increased performance assumed in the simulation does not match the measured values, however there is still marked performance increase for the oval twisted type HX. . .	92
Figure 58	The cold side of the HX is fixed at 0.0315 kg/s while the hot side is swept. Between HXs the experiment shows no change in Nu given these flow conditions.	92
Figure 59	The cold side of the HX is fixed at 0.252 kg/s while the hot side is swept. Though the simulation does not match the measured values there is still marked improvement in Nu for the oval twisted type HX.	93

Figure 60	The difference in measured wattages for the hot and cold side of the HX is apparent in the experiment data while not present in the simulation. Further work must be performed to capture this phenomena in the CFD simulations.	93
Figure 61	The difference in measured Nu for the hot and cold side of the HX is apparent in the experiment data while not present in the simulation. Further work must be performed to capture this phenomena in the CFD simulations.	94
Figure 62	The values obtained for overall heat transfer coefficient in the experiment and simulation do not match with high confidence. The trend in heat transfer coefficient between the data sets does not appear to match in characteristic shape indicating that real-life losses that occur in the experiment are not accounted for in the simulation.	94
Figure 63	The trends in performance increase between the simulation and the experiment are similar with the most drastic improvement occurring at approximately 0.17 and 0.18 kg/s for the measured and simulated data sets respectively.	95
Figure 64	The calculated entropy generation numbers for the circular HX experiment are significantly higher than the CFD results. This indicates that real-life losses are not adequately accounted for in the CFD work.	95
Figure 65	The calculated entropy generation numbers for the oval twisted HX experiment are significantly higher than the CFD results. This indicates that real-life losses are not adequately accounted for in the CFD work.	96
Figure 66	The effectiveness vs NTU curves for the circular geoemtry HX follow the same trends set forth in the CFD work. The CFD data over approximates the improvement in effectiveness vs NTU curves.	96

Figure 67 The effectiveness vs NTU curves for the oval twisted geometry follow the same trends set forth in the CFD work. The CFD data under approximates the improvement in effectiveness vs NTU curves. 97

LIST OF TABLES

Table 1	The discretization error in the circular cross section flow channel design varies between 10 to 21 % for the cold side, and between 4 to 20% for the hot side.	15
Table 2	The discretization error in the oval twisted cross section flow channel design varies between 0.6 to 3% for the cold side, and between 5 to 9% for the hot side.	16
Table 3	The simulation flow rates and respective Re numbers for the both the circular and oval twisted plate type heat exchanger.	18
Table 4	Mass balance values for Volume 1 and Volume 2 with total inlet flow rates of 0.2519 and 0.03149 kg/s respectively for the circular cross-section HX. . .	19
Table 5	A brief summary of the various components used in the IHX test facility.	36
Table 6	Mass balance values for Volume 1 and Volume 2 with total inlet flow rates of 0.03149 and 0.2519 kg/s respectively for the circular cross-section HX. . .	82
Table 7	Mass balance values for Volume 1 and Volume 2 with total inlet flow rates of 0.2519 and 0.03149 kg/s respectively for the oval twisted HX.	83
Table 8	Mass balance values for Volume 1 and Volume 2 with total inlet flow rates of 0.03149 and 0.2519 kg/s respectively for the oval cross-section HX.. . . .	83

List of Abbreviations

A	Amps
A_s	Heat transfer surface area
a	Measurement used in uncertainty calculations
BTU	British Thermal Units
b	Measurement used in uncertainty calculations
CAES	Center for Advanced Energy Studies
CFD	Computational Fluid Dynamics
c_i	Sensitivity Coefficient
CNC	Computer Numerically
C_{max}	Maximum heat capacity rate
C_{min}	Minimum heat capacity rate
C_p	Specific Heat
C_r	Heat capacity rate ratio
D	Hydraulic Diameter
EHD	Electrohydrodynamics
e_a^{21}	Approximate relative error
GCI	Grid convergence index

GCI_{fine}^{21} Fine grid conversion index

GPM Gallons per minute

h Heat transfer coefficient

HCHX Helically Coiled Heat Exchanger

h_{coarse} Coarse mesh size

h_{fine} Fine mesh size

h_{mesh} Mesh size

HX Heat Exchanger

Hz Hertz

IHX Intermediate Heat Exchanger

J Joule

K Kelvin

k Thermal Conductivity

kg Kilogram

kW Kilowatt

k_w Thermal conductivity of water

$k - \varepsilon$ EWT k-epsilon enhanced wall treatment

$k - \omega$ SST k-omega Menter shear stress transport

\dot{m} Mass flow rate

mA Milliamp

MHD	Magnetohydrodynamics
N	Number of Cells
NTU	Number of Transfer Units
Nu	Nusselt Number
N_{s1}	Entropy generation number
p	Apparent order
PEC	Performance Evaluation Criterion
psig	Gauge pressure
PCHX	Printed Circuit Heat Exchanger
PTOTHX	Plate type oval twisted heat exchanger
q	Wattage
Re	Reynolds Number
r	Grid refinement factor
r_{21}	Mesh size ratio h_2/h_1
r_{32}	Mesh size ratio h_3/h_2
\dot{S}_{gen}	Entropy generation rate
s	second
s	Value used to determine Monotonic/Oscillatory convergence
T	Temperature
T_{ci}	Cold fluid inlet temperature

T_{co}	Cold fluid outlet temperature
T_{hi}	Hot fluid inlet temperature
T_{ho}	Hot fluid outlet temperature
U	Overall heat transfer coefficient
u_a	uncertainty in measurement a
u_b	uncertainty in measurement b
u_c	Product uncertainty
$u_c(y)$	Combined Uncertainty via summation in quadrature
u_q	Uncertainty in wattage
$u(x_i)$	Standard Uncertainty
V	Volts
VFD	Variable Frequency Drive
$Y+$	Non-dimensional value used in mesh refinement
ΔT	Temperature Drop
ΔT_{LMTD}	Logarithmic mean temperature difference
ΔV_i	Cell volume

List of Symbols

ε	Effectiveness
ε_{21}	$\phi_2 - \phi_1$
ε_{32}	$\phi_3 - \phi_2$
μ_w	Dynamic viscosity of water
ϕ	Measurement value of interest used in the GCI method
ϕ_1	Corresponds to the measurement value of interest used in the GCI method for the fine mesh size
ϕ_2	Corresponds to the measurement value of interest used in the GCI method for the middle mesh size
ϕ_3	Corresponds to the measurement value of interest used in the GCI method for the coarse mesh size
Φ_{ext}^{21}	Extrapolated relative error
ρ	Fluid Density
ρ_w	Density of water
$^{\circ}\text{C}$	Degrees in Celsius
$^{\circ}\text{F}$	Degrees in Fahrenheit

Computational and Experimental Analysis for a Cross-flow Plate Type Oval-Twisted Tube Heat Exchanger

Thesis Abstract - Idaho State University (2023)

The present master's thesis focuses on conducting experimental investigations to compare the heat transfer performance of cross flow plate type heat exchangers featuring circular and oval twisted flow paths. Through simulations, the flow parameters of the experiment were defined, refining the size, layout, and configuration of the test sections. The experimental facility was successfully designed and constructed to meet the desired experimental requirements. Uncertainty analysis revealed the measurement uncertainties of wattage, Nusselt number, and heat transfer coefficient are all less than 5%. The experimental data obtained showcases that the oval twisted design outperforms the circular counterpart in terms of overall heat transfer coefficient, Nusselt number, and wattage. Moreover, improvements were observed in both balanced and imbalanced flow conditions. The oval twisted design demonstrates superior heat transfer efficiency and lower entropy generation compared to the circular design. The relationship between effectiveness and the number of transfer units was also investigated, indicating significant enhancements in effectiveness and NTU for the oval twisted design. While further work is needed to improve the accuracy of numerically generated data, this study provides valuable insights into the heat transfer performance of cross flow plate type heat exchangers with novel flow paths.

Chapter I: Introduction

1.1 Heat Exchanger Technologies

As in all electrical power production methods, the nuclear industry relies on transforming thermal energy into electrical energy via heat transfer. The methods of transmitting heat from fuel have and continue to be studied thoroughly. There are many and varied reactor designs that have employed countless numbers of heat exchangers (HX) to perform tasks as great as cooling the reactor fuel and as menial as heating a small valve. These tasks are completed using one of many well studied and complex cycles such as the Rankine, Brayton, and Carnot cycles to name just a few. Though in depth studies may be conducted concerning the intricacies of these cycles, this study will focus on the concepts used in heat exchanger design to accomplish steps of these cycles, and possible improvements to these designs.

One form of heat exchanger which is predominant in the nuclear industry is the shell and tube style heat exchanger [1]. This type of heat exchanger may vary greatly in design however the primary components remain the same, where one fluid flows through tubes inside a vessel while another fluid flows over the tubes. This may be varied to accommodate various fluids, pressures, temperatures, and operating environments [2]. The shell portion of this type of HX may be configured as a one pass shell, two pass shell, split flow, double split flow, divided flow, cross flow, and kettle type, some of which are depicted in Figure 1. Each of these shells may contain tubes organized in fixed tube-sheets, u-tube bundles, coils, or any combination of the previous. Additionally these tubes may be modified to amplify active and passive forms of heat transfer, which is covered in further detail in Section 1.1.1. In one study conducted by Al-Hadhrami [3] the traditional internal straight pipe components of a shell and tube HX are replaced with oval twisted tube inserts in a Naptha hydrotreating plant. This changeover resulted in flowrate increases of almost 8% and project cost payoff occurred in approximately 2 years.

Another type of HX commonly used in industry is the plate type heat exchanger. Though

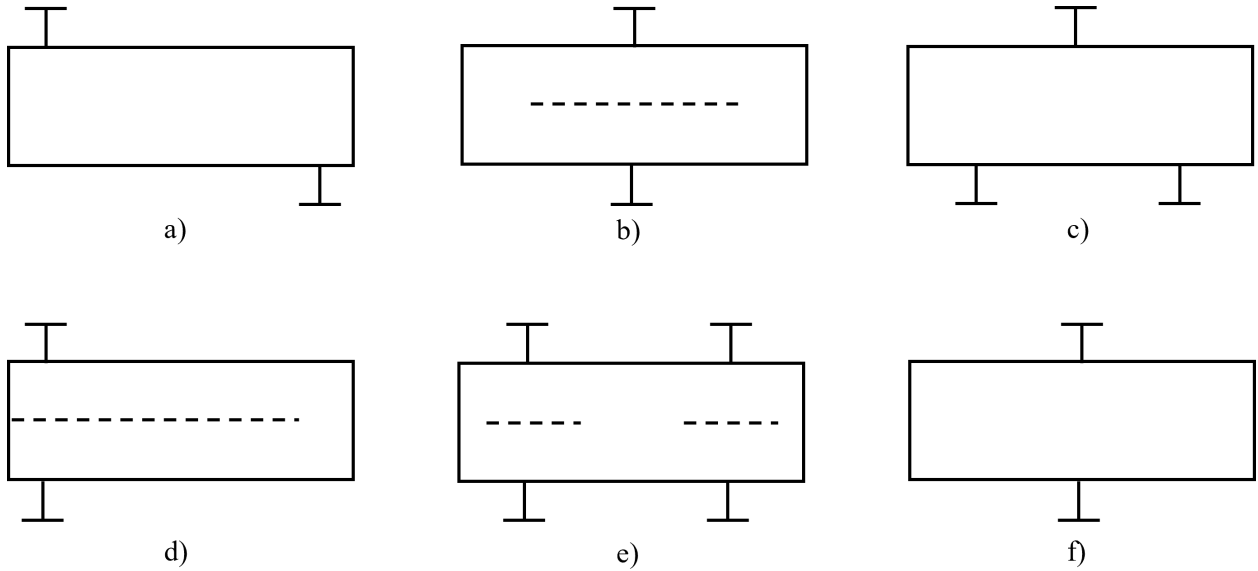


Figure 1: Various types of shells for a shell and tube style HX. a) One pass shell, b) split flow, c) divided flow, d) two pass shell with baffle, e) double split flow, and f) cross flow

the design of these HXs vary greatly the principle is the same, hot and cold fluids generally remain on separate sides of stacked plates as shown in Figure 2, provided by Alfa Laval [4]. Within these types of HXs there may be various pipe configurations, surface geometries, surface coatings, and flow configurations. These design changes are implemented with the goal of providing process critical heat transfer with the general aim of decreasing operation costs. The reduction of operation cost is four fold, including decreasing pumping requirements, increasing heat transfer, increasing HX lifetime, and decreasing HX manufacturing cost.

Helical coiled heat exchangers (HCHX) are often used in industry for their excellent power density. These types of heat exchangers have been studied greatly including the development of correlations for pressure drop, friction factor, and Nu all of which are mentioned in a review by Ali [5]. Studies in this field range in geometry, flow conditions, and working fluids, each of which can have a large impact on HX performance and design. One particular study conducted numerically by Wahlquist [6] focuses on the effect on heat transfer in a HCHX when an oval twisted cross section is employed. Initial findings indicate heat transfer increases from 46 - 56% when compared to an equivalent sized traditional HCHX. Many

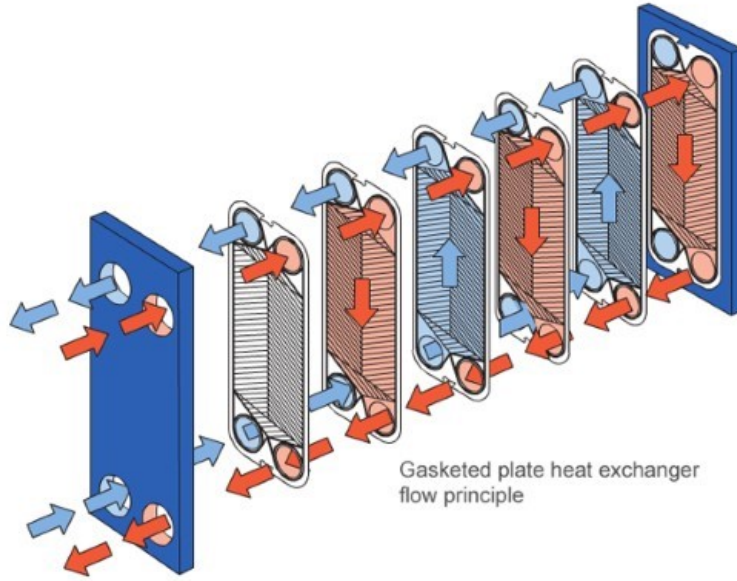


Figure 2: A generalized schematic of a plate type HX indicating the flow paths for hot and cold fluids provided by Alfa Laval [4].

other methods may be used to increase heat transfer in a HCHX such as inserting coiled tapes as studied by Kurnia [7] and Liaw et al. [8] or modifying cross section geometries as explored by Kurnia [9]. Though much work has been performed concerning traditional HCHX geometries, as outlined by Ferng [10], the study conducted by Wahlquist [6] is of great interest since little computational or experimental work has been performed concerning this type of geometrical modification, and is discussed in further detail in Section 1.1.2.

1.1.1 Active and Passive Heat Transfer Amplification Methods

Active Enhancement

Heat transfer enhancement via active methods can be as simple as increasing the flowrate by augmenting pumping power, however, there are other methods such as electrohydrodynamic (EHD), magnetohydrodynamics (MHD), or mechanical motion. These methods though often complex in nature allow for tailored and highly controllable heat transfer enhancement effects. These stand apart from passive heat transfer techniques in that each of them require external power to induce heat transfer enhancement. These methods are out-

lined in a review by Mousa [11]. Where EHD studies such as those conducted by Fernandez [12] prove that an electric field may be used to disturb the boundary layer of a dielectric fluid. These experiments reported increases in heat transfer of up to 20 times when compared to non-activated flow while the pressure losses only increase 3 fold.

An MHD study by Goharkan [13] shows that heat transfer enhancements up to 19% may be obtained by applying a constant or alternating magnetic field of 500 gauss to a working fluid imbued with magnetite nanoparticles. It is assumed that the enhancement occurs due to the disruption of the thermal boundary layer which increases mixing. Additional studies using various metallic nanofluids in numerous different working fluids have been studied, including the use of iron oxide in kerosene [14], and Alumina nanoparticle infused working fluids [15].

Mechanical motion may also be used for active heat transfer enhancement in various ways, one of note is fluid vibration, often called the pulsatile flow method. Nishimura and Matsune [16] investigate flow occurring through sinusoidally oscillating tubes, where these oscillations cause vortice generation in the accelerating and decelerating regions on the tube. This vortice generation increases with frequency up until a certain point, then the opposite effect occurs. Similarly Khosravi-Bizham et al. investigates this phenomena in helically coiled tubes [17] where the highest augmentation of heat transfer occurs in low Re flows, with an average enhancement of approximately 19% at a frequency of 4 Hz. Another Study concerning pulsatile flow was conducted by Jin et al. [18] where this phenomena was studied in a channel with triangular grooves. Enhancement in heat transfer up to 350% is reported at low Re flow parameters.

Other mechanical motion techniques such as rotating the tube, or other heat exchanger geometry have been explored, yet these methods of translating or rotating a heat exchanger section are considered among the most difficult to implement due to the complex nature of moving parts which usually contain working fluids inside a heated system.

Passive Enhancement

Though a comprehensive review of passive heat transfer enhancement techniques cannot be exhausted fully here, a brief review of several and varied techniques is presented. A review of note conducted by El-Genk [19] includes vast data for water, air, and ethylene glycol flows in 62 different coiled tubes. In this review various friction factors and Nu are compared at critical Re and are found to agree withing $\pm 20\%$. These are viable, and relatively well proven methods for passive heat transfer enhancement. Another method often used in passive heat transfer enhancement is the insertion of twisted tapes or other like components inside existing tubes. As presented by Fan [20], twisted tapes are inserted in an effort to minimise losses due to friction and increase heat transfer. The performance evaluation criterion (PEC) for this study is in the range of 1.67 – 2.06, which demonstrates the insert has preferred thermo-hydraulic performance. A similar study as presented by Kurnia [7] is conducted where twisted tape inserts are used in a helically coiled tube in the laminar flow regime. This numerical study anticipates heat transfer enhancement values up to four times greater than a traditional straight tube. Another technique explored by Guo [21], discusses the benefits of a twisted tape insert that is center cleared. This is a tape insert that does not block the center line flow within the tube. Heat transfer enhancements were found to be up to 20% while maintaining the pressure drop within the system. Promvonge similarly studies another insert type by combining conical-rings with twisted-tape inserts [22]. In the turbulent regime, Promvonge determines experimentally that increases in maximum heat transfer up to 367% can occur using these types of inserts, where the conical-rings provide up to 10% of that enhancement.

Another technique presented by Suresh [23] includes the use of water enhanced with nanofluids. This study, conducted using helical screw tape inserts in the laminar flow regime yields increased performance using a copper based nanofluid rather than an aluminum based nanofluid. Another technique used for passive heat transfer enhancement is the use of surface modifications, Eid [24] presents a study where the methods of obtaining various surface modifications are explored. The methods investigated include internal surface grooving on

conduit where key parameters including the depth, width, pitch, and inclination angle of the grooves are considered. Though this study largely concerned itself with the controllability and measureability of surface modifications, certain note is taken concerning the considerations for the pressure loss penalties of these types of surface modifications. In addition to surface modifications geometrical changes also affect passive heat transfer characteristics as studied by Kurnia [9], non-circular profiles are investigated numerically in helically coiled tubes. This method of enhancement focuses on inducing secondary flow via the helix of the tube as well as by the cross section. Though an exhaustive report of these methods would prove helpful and informative, the report compiled by Mousa [11] does an incredible job at outlining and referencing both experimental and numerical works concerning vortex ring inserts, twisted tape inserts, wire inserts, fins, dimples, baffles, ribs, and conical rings to name a few. Each of these methods are complex and often provide notable heat transfer enhancement, usually at the cost of additional pressure losses. Though there are countless methods for passive heat transfer enhancement the end goal is the same, to maximize heat transfer and minimise losses.

1.1.2 Twisted Tube Heat Exchangers

Countless experiments have been conducted concerning the use of non-circular cross-sections for heat transfer enhancement however, most of these experiments do not investigate the phenomena produced when a twist is introduced with a non-circular profile. One recent mostly comprehensive review in which twisted non-circular profiles are investigated is presented by Razzaq [25], in which twisted elliptical, square, triangular, and circular tubes are investigated alongside several insert type turbulence inducers such as twisted tape and conical ring inserts. Findings in this review report improved heat transfer performance for twisted square and oval tubes. Additional findings include increased pressure losses with increases in twist pitch to tube diameter ratio. Lastly, the final conclusion made by this review is that many topics concerning twisted tube heat exchangers are unstudied and open for research activity.

Some studies do exist, such as one provided by Tan et al. [26], which numerically investigates oval twisted tube bundles and compares their performance to available experimental data. Findings include a disparity up to 4% between experimental and computational results. Cheng et al. [27] similarly numerically investigates the performance of a single oval twisted tube with a twist pitch of 0.33 m and a height to width ratio of 2. These investigations occurred at low Re values under 500.

Another investigation conducted by Tan et al. [28] experimentally and numerically explores the phenomena of heat transfer and the increase in friction factor as a function of twist pitch in small arrays of oval twisted tubes. Zhang et al. [29] experimentally investigates the condensation heat transfer coefficient in oval twisted tubes of varying twist pitch for use in sub-cooling. Various numerical studies concerning the change in twist pitch and ellipticity include those conducted by Luo et al. [30], Ebrahimi and Roohi [31], Guo and Wang [32], Promthaisong et al. [33]. Other numerical studies wherein the oval twisted tube is explored mostly include studies concerning their use in shell and tube type HXs such as those presented by Li et al. [34], and Gu et al. [35] [36]. One set of experimental data of note is produced by Liu et al. [37], in which a shell and tube style HX with an oval twisted tube bundle is used. Findings here indicate non-noticeable increases in pressure drop on the shell side of the HX.

Gaps in Current Research

There is a large deficit of experimental data in the study of the heat transfer performance for oval twisted tubes. Though some experimental data does exist most of this work is tailored to uses in shell and tube style HXs. There is currently no data concerning the use of these oval twisted tube geometries for use in plate type HXs. The generation of experimental data for these types of exchangers may aid in paving the way for new, higher efficiency plate type HXs including uses in areas such as printed circuit heat exchangers (PCHX) and stacked plate type HXs including: counter-flow, cross-flow, and concurrent flow types. Additionally with the emergence of additive manufacturing technologies, new heat exchanger types may

be produced with torturous flow paths in which the oval twisted tube may be used.

1.2 Numerical Methodology

Though many of the equations herein are commonplace, a review of equations and variables in use in this study are presented. A more comprehensive review of specific, less common equations used herein will be covered in subsequent sections within the chapters as needed.

The wattage output q is calculated as

$$q = \dot{m}C_p\Delta T \quad (1)$$

where \dot{m} is the mass flow rate, C_p is the specific heat, and ΔT is the temperature change across the HX. The Nusselt number Nu is defined as

$$Nu = \frac{hD}{k} \quad (2)$$

where h is the heat transfer coefficient, D is the hydraulic diameter at the inlet, and k is the thermal conductivity. The heat transfer coefficient is calculated as

$$h = \frac{q}{A_s\Delta T_{LMTD}} \quad (3)$$

where A is the heat transfer surface area and ΔT_{LMTD} is the logarithmic mean temperature difference. The logarithmic mean temperature difference is presented as

$$\Delta T_{LMTD} = \frac{(T_{hi} - T_{co}) - (T_{ho} - T_{ci})}{\ln\left(\frac{(T_{hi} - T_{co})}{(T_{ho} - T_{ci})}\right)} \quad (4)$$

where T_{hi} , T_{ho} , T_{ci} , and T_{co} are the fluid temperatures at the hot inlet, hot outlet, cold inlet and cold outlet respectively.

1.2.1 Flow Imbalance

The ratio of heat capacity rates C_r proves helpful when HXs are analyzed with different mass flow rates and or working fluids on each side of the heat exchanger. This ratio is defined as

$$C_r = \frac{C_{min}}{C_{max}} = \frac{(C_p \dot{m})_{min}}{(C_p \dot{m})_{max}} \quad (5)$$

Where C_{min} in a unmixed HX corresponds to fluid with the smaller heat capacity rate and C_{max} corresponds to working fluid with the larger heat capacity rate. In this study the working fluid is water for both sides of the HX and the change in specific heat between the hot and cold fluids is less than 0.5%. Since the specific heat is essentially constant this ratio becomes

$$C_r = \frac{\dot{m}_{min}}{\dot{m}_{max}} \quad (6)$$

1.2.2 Number of Transfer Units

The number of transfer units (NTU) provides insight into the performance of the HX. This may be determined using the common equation

$$NTU = \frac{UA_s}{C_{min}} \quad (7)$$

where U is the overall heat transfer coefficient and A is the surface area of the HX where the heat transfer is occurring. The heat transfer coefficient may be determined by solving for NTU using a relation defined by Incropera [38],

$$\varepsilon = 1 - \exp \left[\left(\frac{1}{C_r} \right) (NTU)^{0.22} \{ \exp [-C_r (NTU)^{0.78}] - 1 \} \right] \quad (8)$$

where effectiveness is,

$$\varepsilon = \frac{T_{co} - T_{ci}}{T_{hi} - T_{ci}} = \frac{1}{C_r} \frac{T_{hi} - T_{ho}}{T_{hi} - T_{ci}} \quad (9)$$

1.2.3 Entropy

Neglecting the entropy generation due to pressure drop entropy generation is defined as,

$$\dot{S}_{gen} = C_{min} \ln \left(\frac{T_{co}}{T_{ci}} \right) + C_{max} \ln \left(\frac{T_{ho}}{T_{hi}} \right) \quad (10)$$

this however proves an unwieldy variable when comparison between unlike HXs is desired. Though there are several ways to non-dimensionalize entropy generation, a modern approach provided by Hesselgreaves [39] which accounts for flow imbalance is defined as

$$N_{s1} = \frac{T_{ci} \dot{S}_{gen}}{q} \quad (11)$$

where N_{s1} is the entropy generation number. This calculation allows for the comparison of entropy generation in different heat exchangers, one variable usually presented alongside the entropy generation number is the ratio of inlet fluid temperatures T_{hi}/T_{ci} . This is added to the presentation of the entropy generation number since the number defined by Hesselgreaves only employs the cold fluid inlet temperature T_{ci} for non-dimensionalization.

1.3 The Role of Simulations

Simulations will play a key role in both refining the design of the HX and selecting flow parameters for the experiments conducted. The initial stage of the project include using simulations to approximate the performance of various designs of cross flow plate type oval twisted tube heat exchangers (PTOTHX). Problems such as flow path wet out, ensuring the temperature drop across the HX is measureable, plenum mixing, and mass balance characteristics are addressed and resolved within a reasonable time frame and economical limits using simulations. Employing simulations in the early stages of the project allows for fast and inexpensive iterations, since the manufacture of components for use in the test facility is costly and time consuming. Additionally at the conclusion of the project the test

data and simulation data will be available for future comparison and the accurizing of CFD data.

1.4 Project Objectives

Though studies may be completed in any one of the aforementioned topics this study will focus on quantifying the improvement induced by passive forms of heat transfer enhancement on a cross-flow arrangement heat exchanger using only internal geometric changes. Due to the cost of producing test sections for use in the test facility this project will be limited to the construction of one baseline HX with a more traditional geometry and the construction of another more complex passive heat transfer enhanced HX. The project will focus on maintaining key geometrical and flow parameters to ensure that the comparison between the two HXs is fair, unbiased, and of high fidelity.

As part of the project a test facility must be constructed to accommodate both the HXs designed in this project, as well as a wide range of future HXs. For this reason a wide range of operating flow parameters and working fluids must be accommodated. Goals for this project include: designing the test facility to operate with water or Dowtherm-A as a working fluid, heating the working fluid to at least 80° C, and cooling the secondary working fluid to at least 20°C. Capabilities for operating temps up to 260°C should be kept in mind for future testing with other working fluids. The test facility design will be such that the capability of adding a covering gas, and pressuriser system should be easily integrated in future modifications.

The facility will be calibrated and the uncertainty of the system will be analyzed. Standard operating procedures will be outlined for future use of the system and a data acquisition software will be constructed and programmed to gather key measurements such as flowrate, temperature, and pressure.

1.5 Significance

The construction of this test facility will allow for subsequent testing of small intermediate scale HXs and the resultant CFD validation for years to come. In the nuclear industry it is of great import that high fidelity heat exchanger testing capabilities be accessible worldwide, by various organizations. This allows for the contribution of many different entities to add to the wealth of knowledge which is currently lacking in many niches. The development of heat exchanger technologies will propel the power production industry to new heights, where heat transfer capabilities we can now only dream of will exist and be commonplace. This development can only occur if there are driven individuals with access to the required infrastructure to accomplish research. Though the contribution of a new test facility is a milestone in itself, the experimental research presented here will cover a niche of heat transfer performance study that has previously been unexplored.

Chapter II: Numerical Analysis of Novel Plate Type Heat Exchanger

2.1 Thermophysical Properties

To increase simulation fidelity temperature dependent thermophysical properties for water are employed as obtained from Kurnia et al. [7], [9], and [40]. These values provide accurate thermophysical properties within a temperature range of 283-373 K with errors less than 1%, and are provided as:

$$\rho_w = -3.57 \times 10^{-3}T^2 + 1.88T + 753.2 \quad (12)$$

$$\mu_w = 2.59 \times 10^{-5} \times 10^{\frac{238.3}{T-143.2}} \quad (13)$$

$$k_w = -8.35 \times 10^{-6}T^2 + 6.53 \times 10^{-3}T - 0.6 \quad (14)$$

while the specific heat C_p is kept constant at $4181.72 \text{ J kg}^{-1} \text{ K}^{-1}$. These values are all within the range expected for the experiment parameters.

2.2 Sensitivity Study

The meshing strategy includes separate meshing models for the solid fluid regions of the geometry. The Solid region employs a tetrahedral mesh and surface remesher. The fluid region includes tetrahedral mesh, surface remesher, and a prism layer mesh. Calculations concerning $Y+$ were performed to ensure that the prism layer mesher with 4 layers and a stretching factor of 1.2 would capture the boundary layer effects. It should be stated that several meshing strategies including polyhedral meshes, various methods of surface size control, and growth rate modifications were explored in the initial stages of simulations. However, it was decided to maintain a tetrahedral mesh with mostly default characteristics and a prism layer mesher for the interface region, since this mesh displayed the most favorable convergence for the energy term. Other meshes with various turbulence models exhibited poor residuals, rarely reaching convergence below 0.01.

The grid convergence index (GCI) method [41], based on the older Richardson Extrapolation method was used to determine the error due to mesh sensitivity. According to the GCI method the mesh size for a three dimensional grid is defined as

$$h_{mesh} = \left[\frac{1}{N} \sum_{i=1}^N (\Delta V_i) \right]^{1/3} \quad (15)$$

where ΔV_i is the cell volume and N is the total number of cells. Three different mesh sizes must be used in the GCI method where all variables other than mesh size are kept constant. The ratio of mesh sizes called the grid refinement factor $r = h_{coarse}/h_{fine}$ should be greater than or equal to 1.3. The value p is used to define the apparent order and is calculated using the following:

$$p = \frac{1}{\ln(r_{21})} |\ln |\varepsilon_{32}/\varepsilon_{21}| + q(p)| \quad (16)$$

$$q(p) = \ln \left(\frac{r_{21}^p - s}{r_{32}^p - s} \right) \quad (17)$$

$$s = 1 \cdot \text{sgn}(\varepsilon_{32}/\varepsilon_{21}) \quad (18)$$

where $r_{21} = h_2/h_1$, $r_{32} = h_3/h_2$, $\varepsilon_{21} = \phi_2 - \phi_1$, $\varepsilon_{32} = \phi_3 - \phi_2$, and ϕ is the measurement value of interest. The apparent order p is used to determine the type of convergence, and can be solved for using a fixed-point iteration including equations 16-18. If the value is positive then the convergence is monotonic, if the value is negative the convergence is oscillatory. The apparent order is used to determine the extrapolated values between mesh sizes and is defined as

$$\phi_{ext}^{21} = \frac{r_{21}^p \phi_1 - \phi_2}{r_{21}^p - 1} \quad (19)$$

This value may be used to calculate the extrapolated relative error as,

$$e_{ext}^{21} = \left| \frac{\phi_{ext}^{21} - \phi_1}{\phi_{ext}^{21}} \right| \quad (20)$$

Table 1: The discretization error in the circular cross section flow channel design varies between 10 to 21 % for the cold side, and between 4 to 20% for the hot side.

Re	Volume 1 (cold)		Volume 2 (hot)	
	1250	10000	3550	28300
r_{21}	1.5	1.5	1.5	1.5
r_{32}	1.3	1.3	1.3	1.3
ϕ_1	7.98	14.75	7.25	13.56
ϕ_2	7.47	15.19	6.80	13.87
ϕ_3	7.01	15.60	6.37	14.21
p	0.776	0.801	0.818	1.28
GCI_{fine}^{21}	21.4%	9.72%	19.9%	4.23%

This value differs from the approximate relative error,

$$e_a^{21} = \frac{\phi_1 - \phi_2}{\phi_1} \quad (21)$$

The apparent order p , approximate relative error e_a^{21} , and mesh size ratio r_{21} are used to determine the fine-grid conversion index,

$$GCI_{fine}^{21} = \frac{1.25e_a^{21}}{r_{21}^p - 1} \quad (22)$$

The base mesh size values of 4, 6, and 8mm were selected for this study, these values allow for r_{21} and r_{32} values greater than 1.3, which is stated to be desirable in common practice when using the GCI method. A summary of the values for the circular and oval twisted designs determined through the GCI method are provided in Tables 1 and 2.

The values for ϕ_1 , ϕ_2 , and ϕ_3 were obtained through calculating the Nusselt number for hot and cold working fluids at the minimum and maximum values of Re. The error in the oval twisted cross section displays more favorable discretization error than the circular non-twisted counterpart. This apparent difference is likely due to the model selected for this study, see Section 2.3 for more details.

Residuals for continuity, momentum, energy, specific dissipation rate, and turbulent kinetic energy were set to a minimum stopping criteria of 1E-6 for all simulations although

Table 2: The discretization error in the oval twisted cross section flow channel design varies between 0.6 to 3% for the cold side, and between 5 to 9% for the hot side.

Re	Volume 1 (cold)		Volume 2 (hot)	
	1250	10000	3550	28300
r ₂₁	1.5	1.5	1.5	1.5
r ₃₂	1.3	1.3	1.3	1.3
ϕ_1	10.49	22.64	9.11	20.76
ϕ_2	10.89	23.25	9.73	21.02
ϕ_3	11.51	23.30	10.48	21.16
p	2.288	4.617	1.590	0.663
GCI _{fine} ²¹	3.13%	0.61%	9.3%	5.1%

the energy criterion rarely converged to a value less than 1E-3.

2.3 Model Selection

Several models were considered for the purposes of this study and a brief summary is presented herein. One model often used to capture turbulent flow characteristics in the k-epsilon enhanced wall treatment model ($k - \varepsilon$ EWT). This model focuses on enhancing the prediction of turbulent flow where increases in separated and secondary flow are present. It also attempts to capture boundary layer effects by employing a 2-layer model catering towards enhanced wall treatment. This model provided by Shih et al. [42] aides in resolving the mean flow characteristics for complex structures and is given as.

$$\nabla \cdot (\rho k \mathbf{u}) = \nabla \cdot \left[\left(\mu + \frac{\mu_t}{\sigma_k} \right) \nabla k \right] + G_k + G_b + \rho \varepsilon - Y_M + S_k \quad (23)$$

$$\nabla \cdot (\rho \varepsilon \mathbf{u}) = \nabla \cdot \left[\left(\mu + \frac{\mu_t}{\sigma_\varepsilon} \right) \nabla \varepsilon \right] + \rho C_1 S_\varepsilon - \rho C_2 \frac{\varepsilon^2}{k + \sqrt{\nu \varepsilon}} + C_{1\varepsilon} \frac{\varepsilon}{k} C_{3\varepsilon} G_b + S_\varepsilon \quad (24)$$

Where k is the turbulent kinetic energy, ε is the turbulent dissipation rate, G_k is the turbulent kinetic energy generation produced due to the mean velocity gradient, G_b is the buoyancy produced by turbulent kinetic energy, Y_M is the varying amplification in compressible turbulence which advances dissipation. The variables S_k and S_ε are user defined, σ_k and σ_ε are turbulent Pr numbers for the turbulent kinetic energy and turbulent dissipation rate

respectively, and the constants $C_{1\varepsilon}$, C_2 , σ_k , and σ_ε are 1.44, 1.9, 1.0, and 1.2 respectively.

The model selected for this study is the Menter Shear Stress Transport k - Ω ($k - \omega$ SST) turbulence model originally developed by Menter [43]. This model was selected for the enhanced ability to capture near wall regions of turbulent flow while combining this behavior with the free stream k -Epsilon behavior. The turbulent kinetic energy and specific rate of dissipation transport equations defined by Rotta [44] are given as

$$\nabla(\rho k \mathbf{u}) = P_k - \beta^* \rho \omega + \nabla [(\mu + \sigma_k \nu_T) \nabla k] \quad (25)$$

$$\nabla(\rho \omega \mathbf{u}) = \alpha \rho S^2 - \beta \rho \omega^2 + \nabla [(\mu + \sigma_\omega \mu_T) \nabla \omega] + 2(1 - F_1) \rho \sigma_{\omega 2} \frac{1}{\omega} \nabla k \cdot \nabla \omega \quad (26)$$

the kinematic eddy viscosity $\mu_T = \rho a_1 k / \max(a_1 \omega, SF_2)$, and constants a_1 , a_2 , β_1 , β_2 , β^* , σ_{k1} , σ_{k2} , $\sigma_{\omega 1}$, $\sigma_{\omega 2}$ are 0.556, 1.9, 0.075, 0.0828, 0.09, 0.085, 1.0, 0.5, and 0.856 respectively.

Though some parameters outlined for the study do not traditionally indicate turbulent flow, it is anticipated that the oval twisted heat exchanger arrangement induces secondary flow and therefore more turbulence within the flow conditions outlined in section 2.4. For this reason, even with Reynolds numbers as low as 1200 turbulent flow characteristics are anticipated for the oval twisted heat exchanger. Additionally since most of the fluid flow parameters demarcated in this study are in the traditionally accepted turbulent flow regime it follows that an enhanced turbulence model be employed. It should be noted that the flow characteristics for the circular profile heat exchanger may be laminar for select cases wherein the Re number is less than 2300 and that uncertainty in these cases is increased. This is apparent in the sensitivity study given in Section 2.2 where for the circular cross section heat exchanger the uncertainty is higher when the Reynolds numbers are lower.

2.4 Parameter Selection and Case Outline

With objective of comparing simulation and test results, the parameters for the simulations were selected with test facility constraints in mind. The facility constraints include the

Table 3: The simulation flow rates and respective Re numbers for the both the circular and oval twisted plate type heat exchanger.

Flow Rate (kg/s)	Re	
	(20 °C)	(80 °C)
0.03149	1252	3542
0.06298	2504	7084
0.12600	5010	14172
0.18893	7513	21251
0.25190	10017	28333

ability to:

1. Measure the change in temperature across the HX with acceptable uncertainty.
2. Maintain feasible steady inlet temperatures.
3. Maintain steady measureable flow rates.

Further information concerning uncertainty may be found in Section 3.5, for this study it was determined that a minimum temperature drop of 2 °C is acceptable across the HX. Early simplified simulations were conducted with varied flow rates and heat exchanger geometries to refine the test section sizing and approximate desired flow rates. These simulations also considered and preserved the attainability and measureability of facility flow rates and temperatures. It was determined that the cold and hot side inlets of the HX should be 20 °C and 80 °C respectively, and the mass flow rates should be between 0.03 and 0.25 kg/s as outlined in Table 3.

After basic simulations were conducted verifying measureable flow rates and temperatures, further simulations were conducted on the geometry of interest to verify the mass balance properties of the test section. Calculations for one case with respective cold volume 1 and hot volume 2 flow rates of 0.2519 and 0.03149 kg/s respectively may be found in Table 4. The mass flow rates for the inlet and outlet values in this table were obtained from the computational software at 6.4 mm from the inlet and outlet of the interior flow channels as indicated in Figure 3. The conservation of mass for the circular and oval twisted geometry

Table 4: Mass balance values for Volume 1 and Volume 2 with total inlet flow rates of 0.2519 and 0.03149 kg/s respectively for the circular cross-section HX.

Volume 1					Volume 2				
#	Inlet (kg/s)	Outlet (kg/s)	% of Total	Mass Balance	#	Inlet (kg/s)	Outlet (kg/s)	% of Total	Mass Balance
1	0.01414	0.01417	5.6%	0.16%	17	0.00391	0.00390	12.4%	0.34%
2	0.01505	0.01502	6.0%	0.19%	18	0.00379	0.00379	12.0%	0.04%
3	0.01388	0.01399	5.5%	0.77%	19	0.00448	0.00450	14.2%	0.61%
4	0.01408	0.01410	5.6%	0.18%	20	0.00362	0.00362	11.5%	0.05%
5	0.01578	0.01590	6.3%	0.77%	21	0.00356	0.00356	11.3%	0.02%
6	0.01780	0.01780	7.1%	0.02%	22	0.00438	0.00440	13.9%	0.41%
7	0.01914	0.01954	7.6%	2.09%	23	0.00375	0.00374	11.9%	0.28%
8	0.01467	0.01436	5.8%	2.08%	24	0.00384	0.00382	12.2%	0.63%
9	0.01543	0.01505	6.1%	2.49%					
10	0.01993	0.02005	7.9%	0.61%					
11	0.01766	0.01772	7.0%	0.29%					
12	0.01548	0.01544	6.1%	0.27%					
13	0.01402	0.01408	5.6%	0.41%					
14	0.01362	0.01385	5.4%	1.69%					
15	0.01435	0.01442	5.7%	0.52%					
16	0.01472	0.01464	5.8%	0.58%					

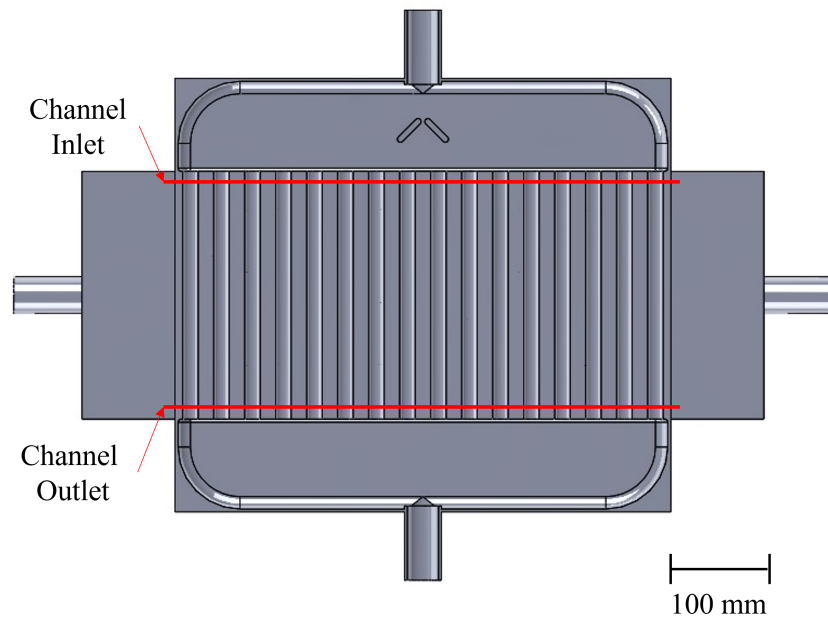


Figure 3: Measuring the inlet and outlet flow rates of each flow channel indicates that the conservation of mass flow rate is acceptable measuring with the highest discrepancy of 3% as shown in Table 4 and Appendix A Tables 6-8.

configurations was calculated for each flow channel at flow rates of 0.2519 and 0.03149 kg/s for both the hot and cold side of the HX. The values confirming the conservation of mass can be found in Appendix A, Tables 6-8, these tables confirm that the measured mass flow out of each channel is within at least 3% of the inlet mass flow rate.

2.5 CFD Results

2.5.1 Imbalanced Flow

Analyzing imbalanced flow conditions where the ratio of heat capacity rates C_r varies allows for the projection of HX characteristics across the many possible real life flow parameters. In Figure 4 the flow rate on the cold side is fixed at 0.03149 kg/s (≈ 0.5 GPM) while the mass flow rate on the hot side sweeps across all flow parameters. The average increase in q is approximately 24% for the oval twisted HX when compared to the circular type. In Figure 5 the flow rate on the cold side is fixed at 0.2519 kg/s (≈ 4 GPM) and the increases in q range from 36 - 48%. When Figures 4 and 5 are considered together it can be inferred that for any combination of flow rates an increase in wattage between 24 - 48% is expected for the oval twisted type HX.

In Figure 6 the flow rate on the cold side is fixed at 0.03149 kg/s (≈ 0.5 GPM) while the mass flow rate on the hot side sweeps across all flow parameters. The average increase in Nu is between 26% and 32% for the oval twisted HX when compared to the circular type. In Figure 7 the flow rate on the cold side is fixed at 0.2519 kg/s (≈ 4 GPM) and the increases in Nu range from 41 - 54%. When Figures 6 and 7 are considered together it can be inferred that for any combination of flow rates an increase in Nu between 26% - 54% is expected for the oval twisted type HX when compared to the circular counterpart.

2.5.2 Balanced Flow

In balanced flow conditions where the mass flow rate of the hot and cold side of the heat exchanger is equal, calculated values for total wattage q , Nu, and overall heat transfer

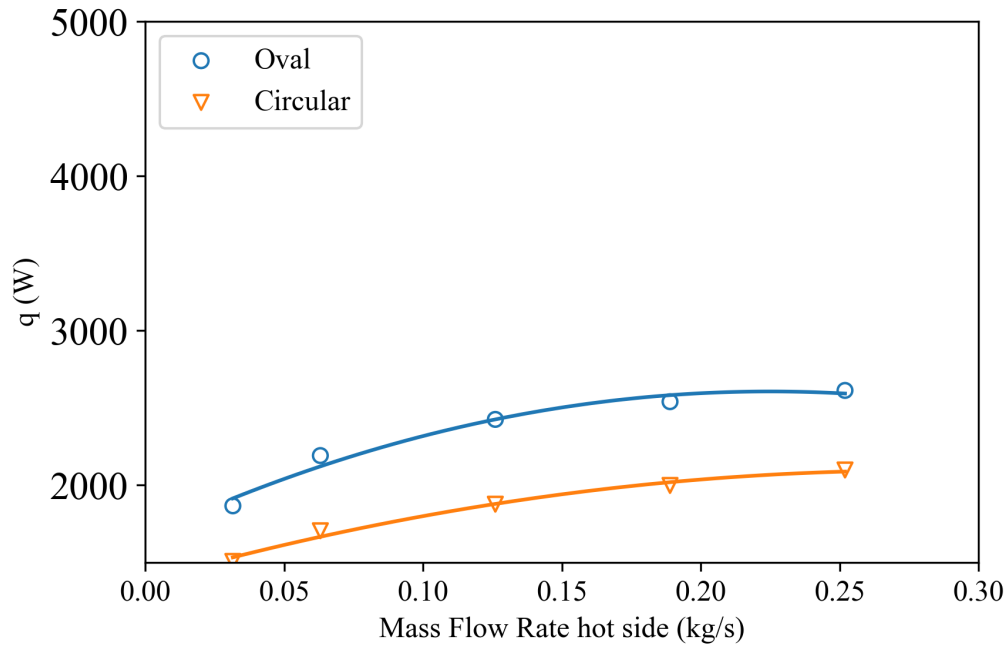


Figure 4: With the cold side fixed at 0.03149 kg/s ($\approx 0.5 \text{ GPM}$) the oval twisted HX displays approximately 24% higher heat transfer than the circular counterpart.

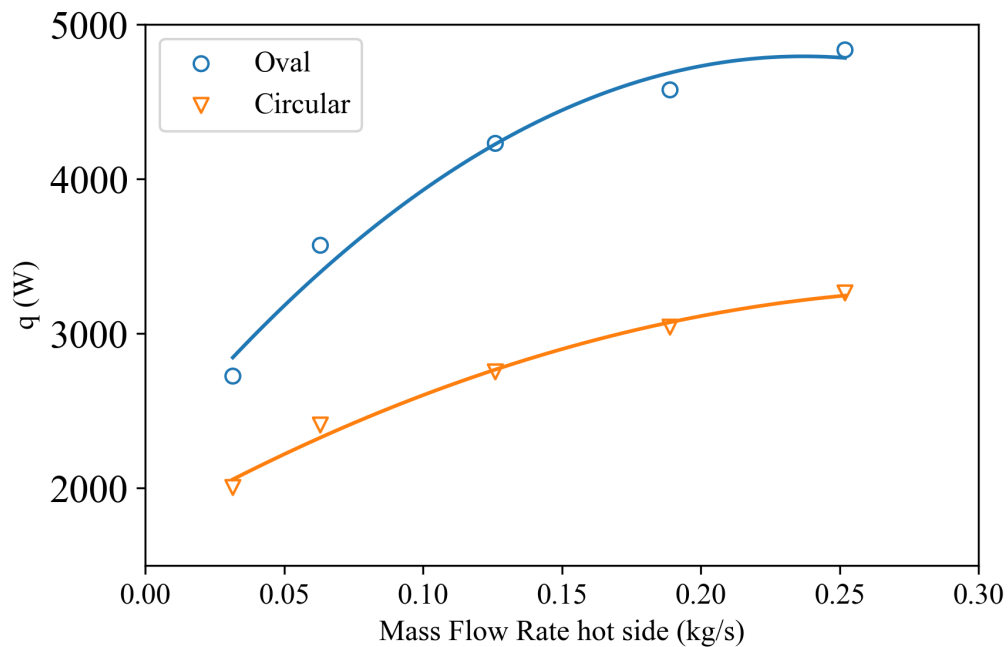


Figure 5: With the cold side fixed at 0.2519 kg/s ($\approx 4 \text{ GPM}$) increases of 36% and 48% were experienced at the lowest and highest simulated flow rates respectively.

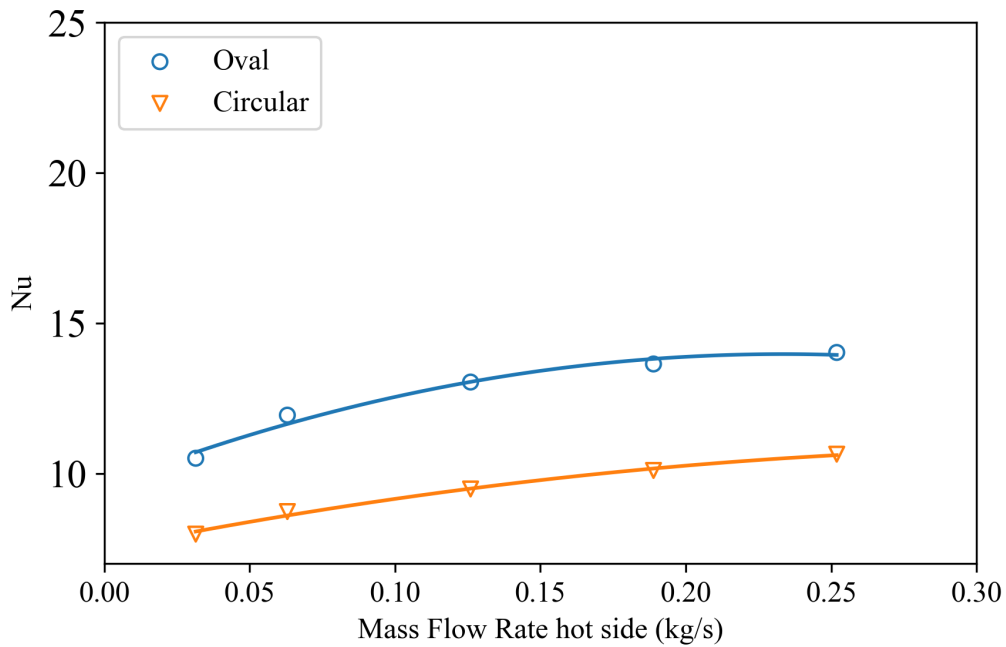


Figure 6: With the cold side fixed at 0.03149 kg/s ($\approx 0.5 \text{ GPM}$) the oval twisted HX displays Nu increases averaging 26% and 32% for the hot and cold sides respectively.

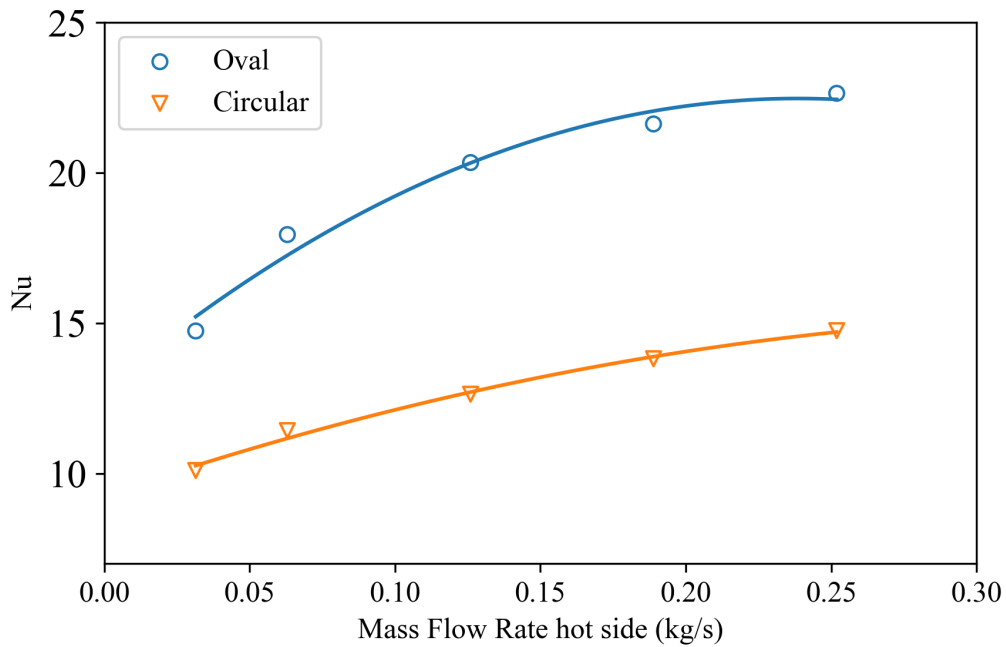
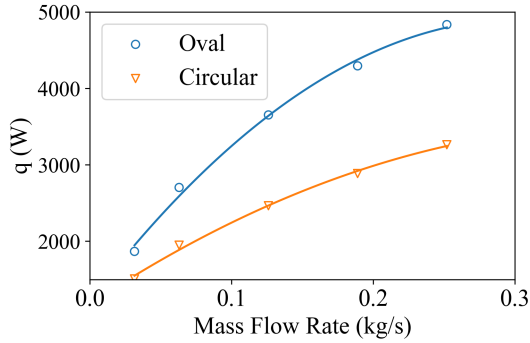
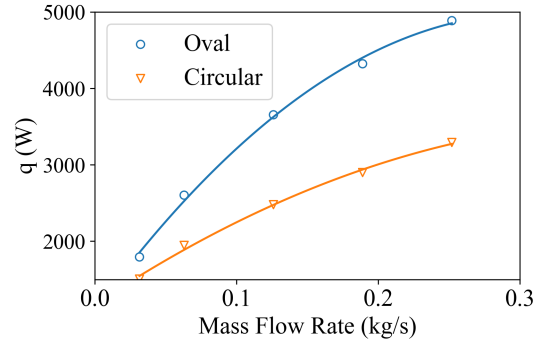


Figure 7: With the cold side fixed at 0.2519 kg/s ($\approx 4 \text{ GPM}$) Nu increases between 41% and 54% are experienced with the highest increases occurring in the cold side of the HX at high flow rates.



(a) The calculated wattage gathered from simulations for the cold side of the HX.



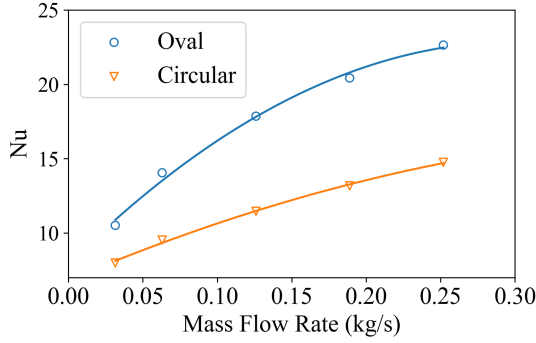
(b) The calculated wattage gathered from simulations for the hot side of the HX.

Figure 8: The wattage on the hot and cold sides of the HX is nearly identical. The average wattage for the oval twisted HX is approximately 18% - 33% higher when compared to the circular counterpart.

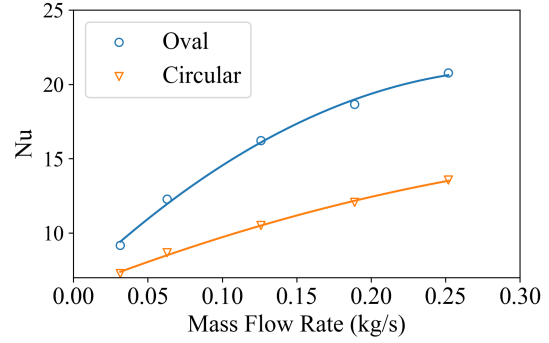
coefficient U are analyzed. All values for these variables saw increases between 18-35% when the HX design was changed from circular flow paths to oval twisted flow paths.

The heat transfer versus mass flow rate for balanced flow conditions is plotted in Figure 8. At the lowest measured flow rate the simulations of the oval twisted type HX anticipate an increase of 18% over the circular type HX. These improvements in overall wattage grow with flowrate, where the highest simulated values for a flowrate of 0.252 kg/s show improvements of approximately 33%. In this Figure it is also noted that there is a slight difference between the wattage in the cold and hot sides of the heat exchanger. These differences in wattages are due to conduction in the metal body of the HX and losses due to entropy generation in the fluid. The trend in this data shows that as flow rates increase the difference in wattage between the hot and cold sides of the HX becomes less apparent. This is because entropy generation decreases with effectiveness, more on this may be discussed in section 2.5.3. It may also be noted that the amount of losses due to conduction and entropy become smaller - relative to the heat transfer, as the amount of heat transfer performed by the bulk fluid climbs.

The Nusselt number also improves when oval twisted flow paths are used instead of



(a) The Nusselt number calculated for the cold side in the heat exchanger is significantly higher than the Nu number on the hot side.



(b) The Nu number on the hot side of the HX is smaller than the Nu number on the cold side.

Figure 9: The difference in Nu on the hold and cold sides is due to differences in inlet thermal conductivity and heat transfer coefficient h . The increase in Nu number for the oval twisted HX compared to the circular is between 25% and 35%.

circular. In Figure 9, there is an average increase between 22% and 35% where the Nu for both hot and cold sides of the HX is plotted. In this case the difference in Nu between the hot and cold side is due to a change in heat transfer coefficient h , and thermal conductivity k . The respective thermal conductivity's for the hot and cold inlets are 0.665 and 0.596 $Wm^{-1}K^{-1}$. The change in heat transfer coefficient between the hot and cold sides for the circular HX is between 1% and 3% with the hot side generally having a higher heat transfer coefficient. The oval HX experienced a change in heat transfer coefficient between the hot and cold sides of approximately 0% - 5% with the hot side usually having a higher heat transfer coefficient. With this taken into consideration the change in Nu between the hot and cold side of the HX is largely due to the difference in thermal conductivity between the hot and cold sides.

A useful variable to consider is the overall heat transfer coefficient as calculated from Eq. 7, shown versus mass flow rate in Figure 10. For balanced flow conditions the gain in heat transfer coefficient is between 25% and 35% when an oval twisted flow path is used instead of a circular flow path. Since C_{min} and the heat transfer surface areas are the same for the circular and oval twisted designs, any rise in overall heat transfer coefficient is due

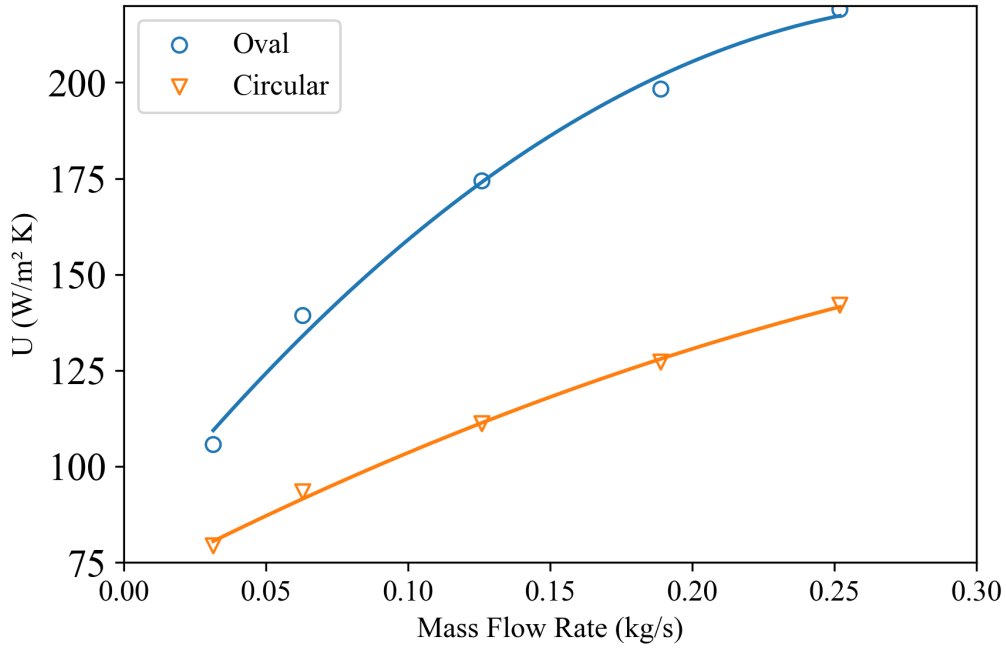


Figure 10: The overall heat transfer coefficient for the oval twisted type heat exchanger is an average of 25% higher at the lowest flow rate and 35% higher at the maximum flow rate.

to a proportional increase in number of transfer units. Since NTU is calculated using Eq. 8 and Eq. 9, and C_r is fixed, the increase in NTU is directly tied to increases in effectiveness.

Considering all of the aforementioned variables together allows for an easy observation of performance. Balanced flow conditions are shown in Figure 11 where the oval performance increase ratios of U_{oval}/U_{circ} , Nu_{oval}/Nu_{circ} , and q_{oval}/q_{circ} are plotted against mass flow rate. Across all flow parameters for this study the performance increase ratios for U, Nu, and q are greater than unity. This provides high confidence levels that the heat transfer properties of the oval twisted HX outperforms the circular counterpart.

2.5.3 Entropy Generation

This study neglects the contribution of entropy generation due to pressure drop as given in Eq. 10. As shown in Figure 12 the Effectiveness vs entropy generation number curves for the circular design follow trends similar to those found in literature. Though the slope of the line found in literature is different, this is expected since the non-dimensionalization of entropy

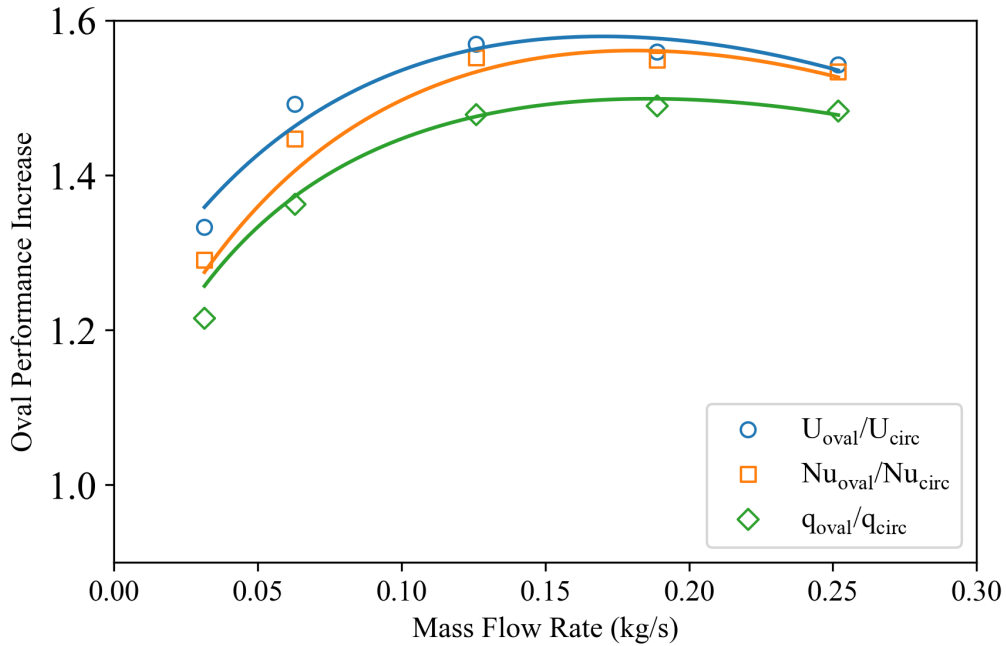


Figure 11: The performance increase for the oval heat exchanger compared to the circular HX shows greater than 1 across all simulated flow parameters for balanced flow conditions.

generation allows for the comparison of unlike HXs; and Hesselgreaves [39] does not mention the type of HX in the analysis provided. Prior analysis and this, provide corroboration that as C_r decreases, the slope of the effectiveness vs N_{s1} plot trends towards zero. This tendency is noted in both the circular and oval twisted design as shown in Figure 13. The oval twisted design however presents lower entropy generation and higher effectiveness values for the flow parameters considered in this numerical study. The increase in effectiveness for the oval twisted design is found to be between 20% and 30% whereas the decrease in entropy generation is between approximately 1 - 6%.

2.5.4 Number of Transfer Units

The number of transfer units NTU provides insight into the HX's ability to transfer heat and is often tied to surface area. A larger HX with the same overall heat transfer coefficient as another will have a larger NTU than a smaller HX. However if the HXs both have the same heat transfer surface area and flow parameters, any change in overall heat transfer coefficient

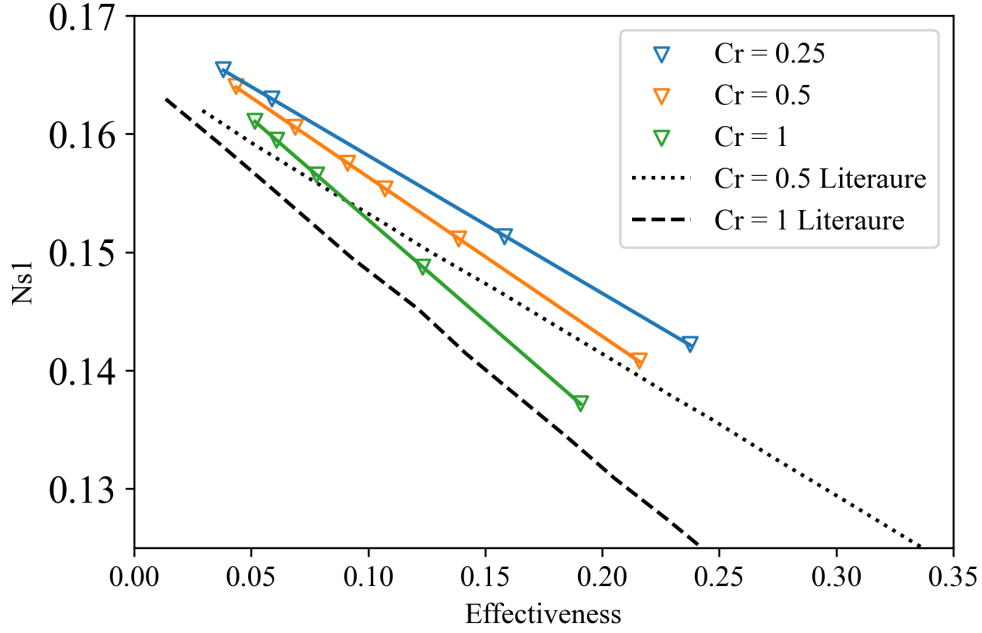


Figure 12: Entropy generation number for the circular flow channel type HX shows higher values while effectiveness shows lower values when compared to the oval type HX in Figure 13, for $T_{hi}/T_{ci}=1.2$.

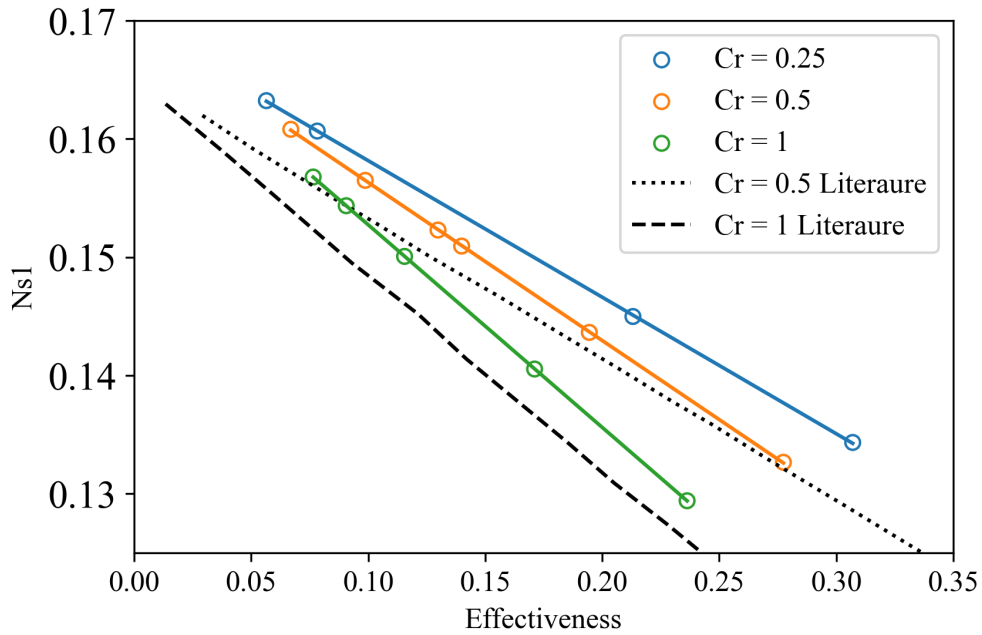


Figure 13: The entropy generation number for the oval twisted type HX is lesser for both balanced and imbalanced flow parameters while simultaneously increasing effectiveness, for $T_{hi}/T_{ci}=1.2$.

will result in a proportional rise in NTU as shown in Eq. 7. In this study, the surface area of the circular and oval twisted design are maintained within 0.6% of each other, the heat transfer surface area is 0.4143 m^2 for the circular design and 0.4115 m^2 for the oval twisted design. This results in simulation designs where the hydraulic diameters for the internal flow channels in the circular design are different than the hydraulic diameters in the oval twisted design. This design choice does bias other flow characteristics and parameters such as internal local Re number. However for NTU and entropy analysis, maintaining the heat transfer surface area between designs proves necessary.

As expected in Figure 14, NTU grows with increases in effectiveness; and there are slight increases in effectiveness as C_r decreases. When circular and oval designs are compared, as shown in Figures 14 and 15, improvements in both effectiveness and NTU are noted for the oval twisted design. The enhancement for the oval twisted design ranges between 19% - 35% for effectiveness and between 25% - 35% for NTU. Since the flow parameters and heat transfer surface area are the same, these improvements are directly tied to the flow intensification from geometrical design changes.

2.5.5 Temperature Distribution

The temperature distribution provides valuable information concerning the characteristics of heat transfer between the fluid and solid regions. Figures 16 and 17 indicate where the temperature profiles were obtained, these line probes are located at the mid-planes of each respective flow region.

The temperature profile for balanced flow conditions at a flowrate of 0.03149 kg/s ($\approx 0.5 \text{ GPM}$) is shown for the cold and hot sides in Figures 18 and 19 respectively. At this low flow rate the temperature distribution for the oval and circular HXs is very similar. In Figure 19 however, the amplitude of the temperature distribution for the oval HX is smaller than the circular design. This indicates that the fluid is providing more heat transfer to the surrounding metal, thus increasing the temperature of the adjacent metal. This phenomena

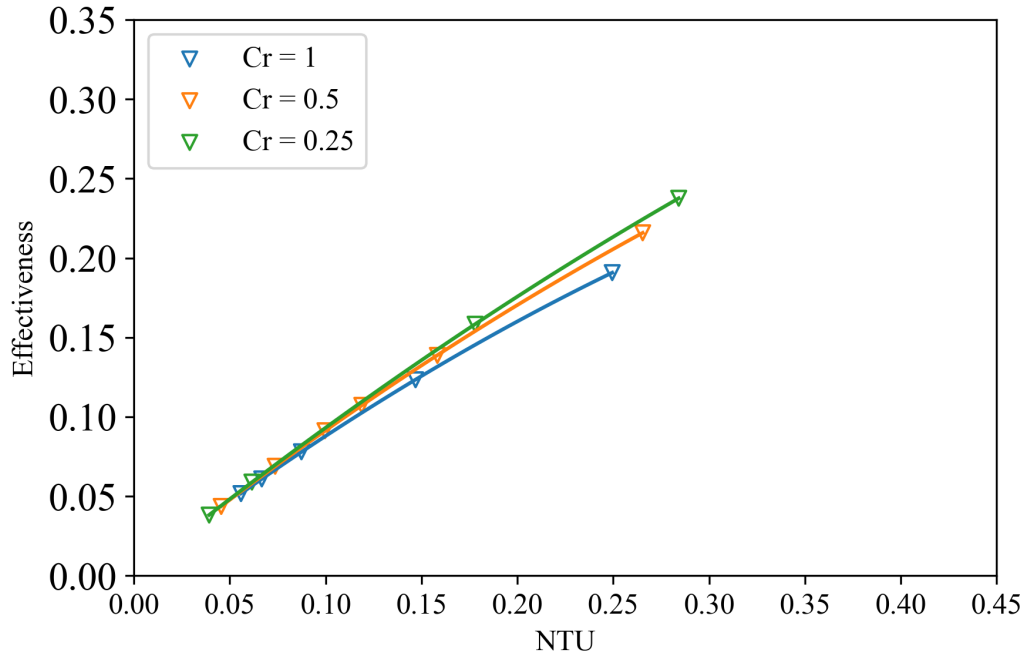


Figure 14: The NTU vs Effectiveness curves for the circular cross-section HX shows values shifted down 19% – 35% and to the left 25% – 35% when compared to an oval twisted counterpart.

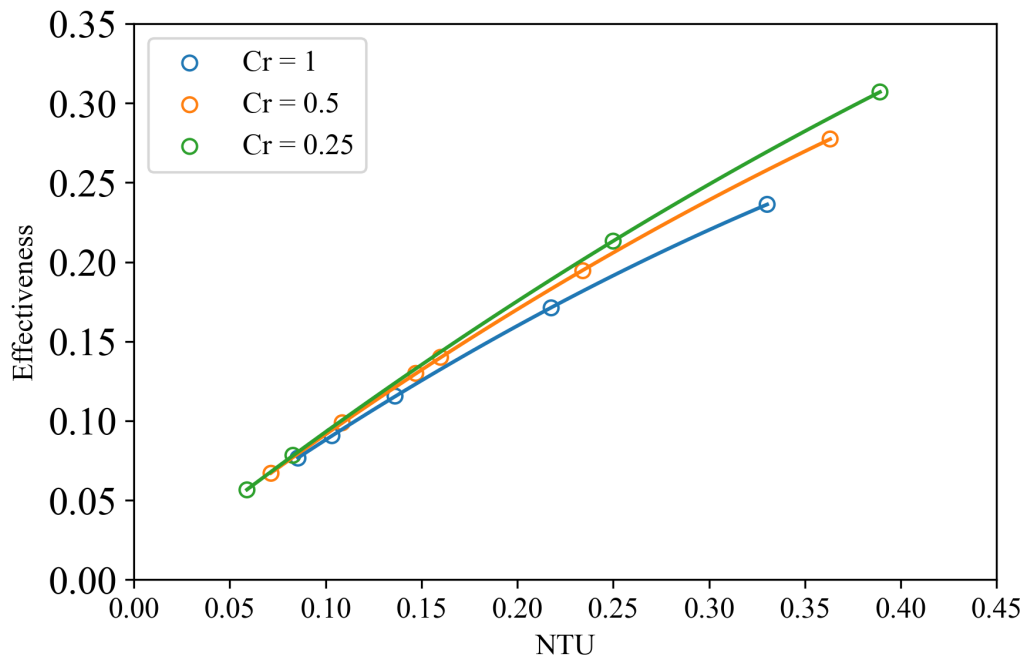


Figure 15: The NTU vs Effectiveness curves for the oval cross-section HX shows values shifted up 19% – 35% and to the right 25% – 35% when compared to a circular flow channel counterpart.

Simcenter STAR-CCM+



Figure 16: An isometric view indicating where the temperature profiles are collected for the hot and cold sides of the HX.

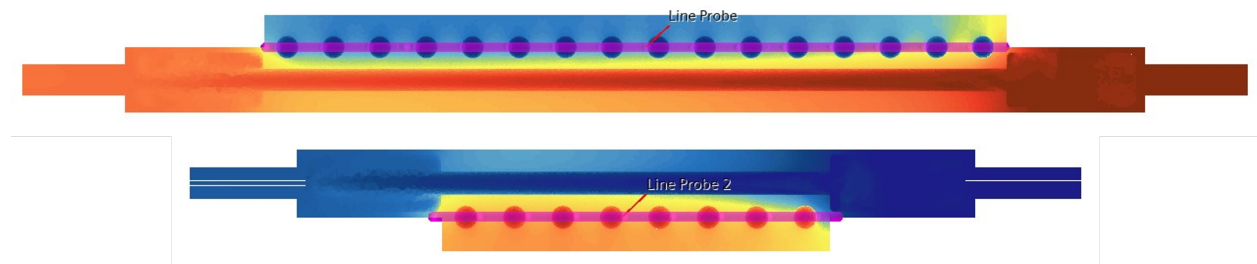


Figure 17: The locations where the temperature profiles are measured at the mid-planes of the HX and across the center-lines of the flow regions with the cold side (top) and the hot side (bottom).

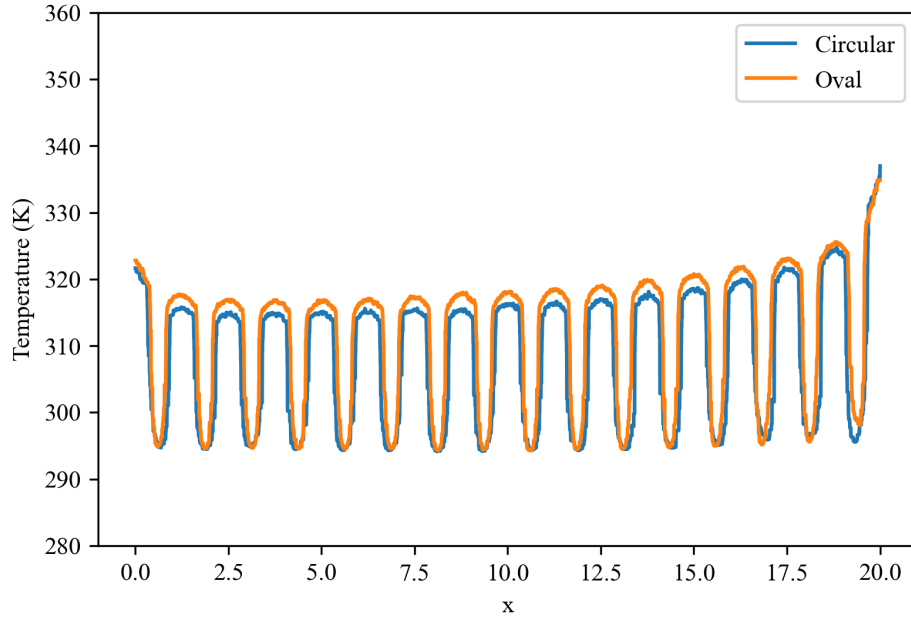


Figure 18: The temperature profile of the cold side of the HX with flow rates for the hot and cold side fixed at 0.03149 kg/s ($\approx 0.5 \text{ GPM}$). The temperature distribution for the oval and circular designs is very similar.

becomes more apparent as flow rates increase as shown in Figures 20 and 21 where the mass flow rate equals 0.2519 kg/s .

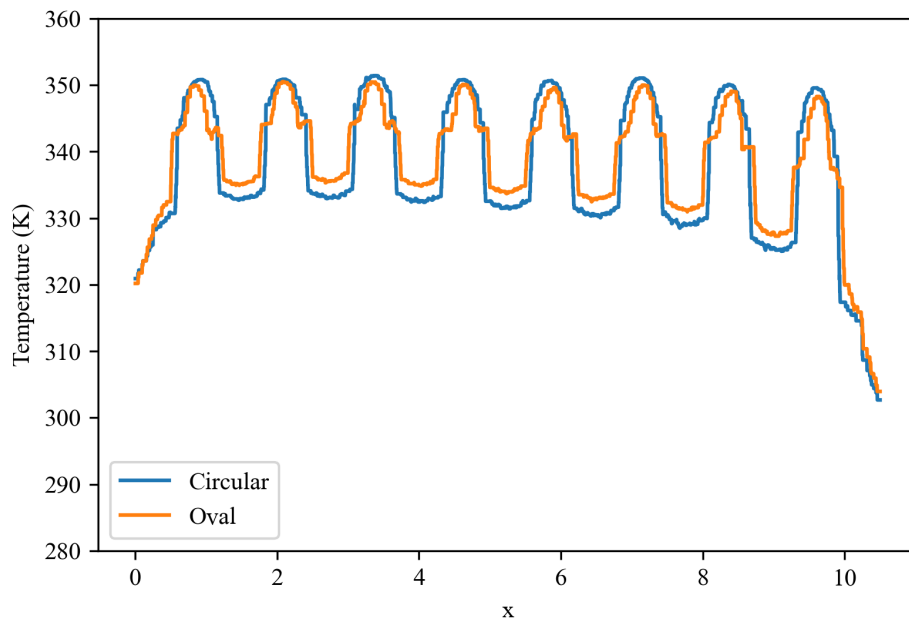


Figure 19: The temperature profile of the hot side of the HX with flow rates for the hot and cold side fixed at 0.03149 kg/s ($\approx 0.5 \text{ GPM}$). The amplitude of the temperature distribution slightly less for the oval twisted design, indicating more efficient heat transfer between the solid and fluid regions.

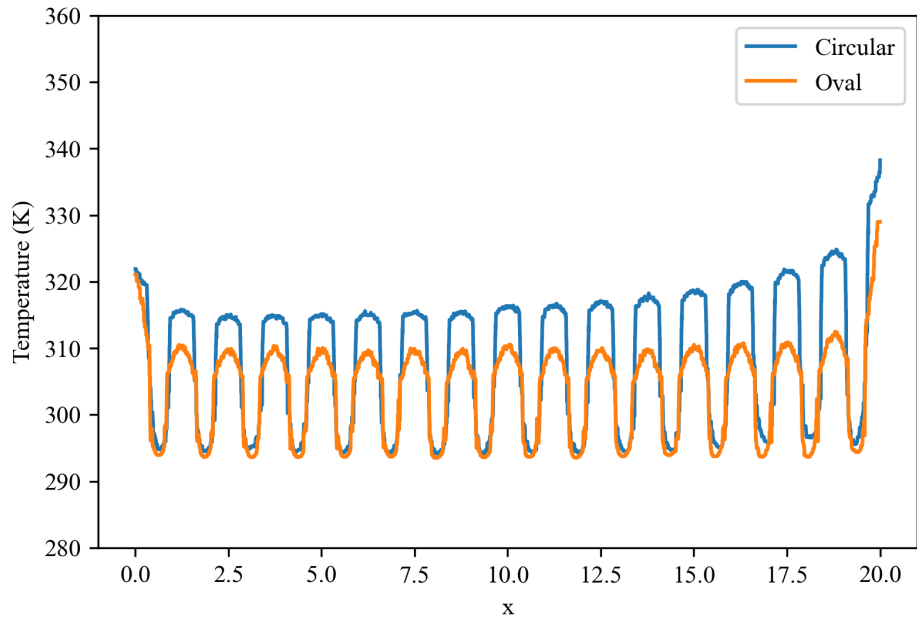


Figure 20: The temperature profile of the cold side of the HX with flow rates for the hot and cold sides fixed at 0.2519 kg/s ($\approx 4 \text{ GPM}$). The change in temperature between fluid and solid regions for the oval twisted design is much less than the circular design.

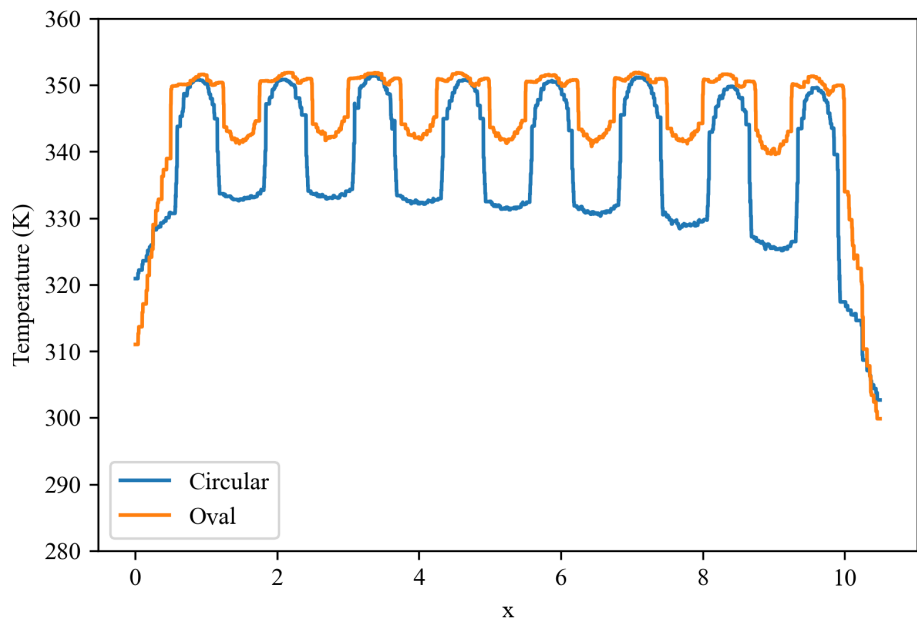


Figure 21: The temperature profile of the hot side of the HX with flow rates for the hot and cold side fixed at 0.2519 kg/s ($\approx 4 \text{ GPM}$). The change in temperature between fluid and solid regions for the oval twisted design is much less than the circular design.

Chapter III: Experimental Facility

3.1 Design

The test facility is designed to operate with several different fluids in the liquid state. For this study deionized water is used for both primary and secondary loops. The Primary loop pictured in Figure 22 on the left contains a 30 kW heater, flowmeter, expansion tank, pump, expansion joint, various thermocouples, various valves, a pressure transducer, and the hot fluid side of a heat exchanger test section. The secondary loop replaces the heater with a secondary liquid cooled heat exchanger and no thermal expansion joint, this secondary HX is included to maintain the cold operating temperature of the secondary loop. This secondary heat exchanger is cooled using cold industrial water which remains unmixed with the deionized water in the secondary loop. Thermocouples for both loops are located at various points to obtain temperature readings at critical locations. The valves in both loops are located in various positions to allow for refined flowrate and temperature adjustments by creating back-flow, restricting flow, and or blocking flow. The temperature, pressure, and flowrate readings are intended to be acquired through LabVIEW and exported to Microsoft Excel in real time, more specifics on this are found in Section 3.5.1. After construction was completed, a readiness review was held following the Center for Advanced Energy Studies (CAES) protocols and found ready for safe operation.

3.2 Component Description

The IHX test facility was constructed using various components for pumping, heating, and to gather various measurements. These off-the-shelf components are outlined in Table 5 .

3.3 Construction

The structural components of the facility were constructed employing channel strut assembled over a drip pan to contain any leaking fluids. Modular channel strut was selected since

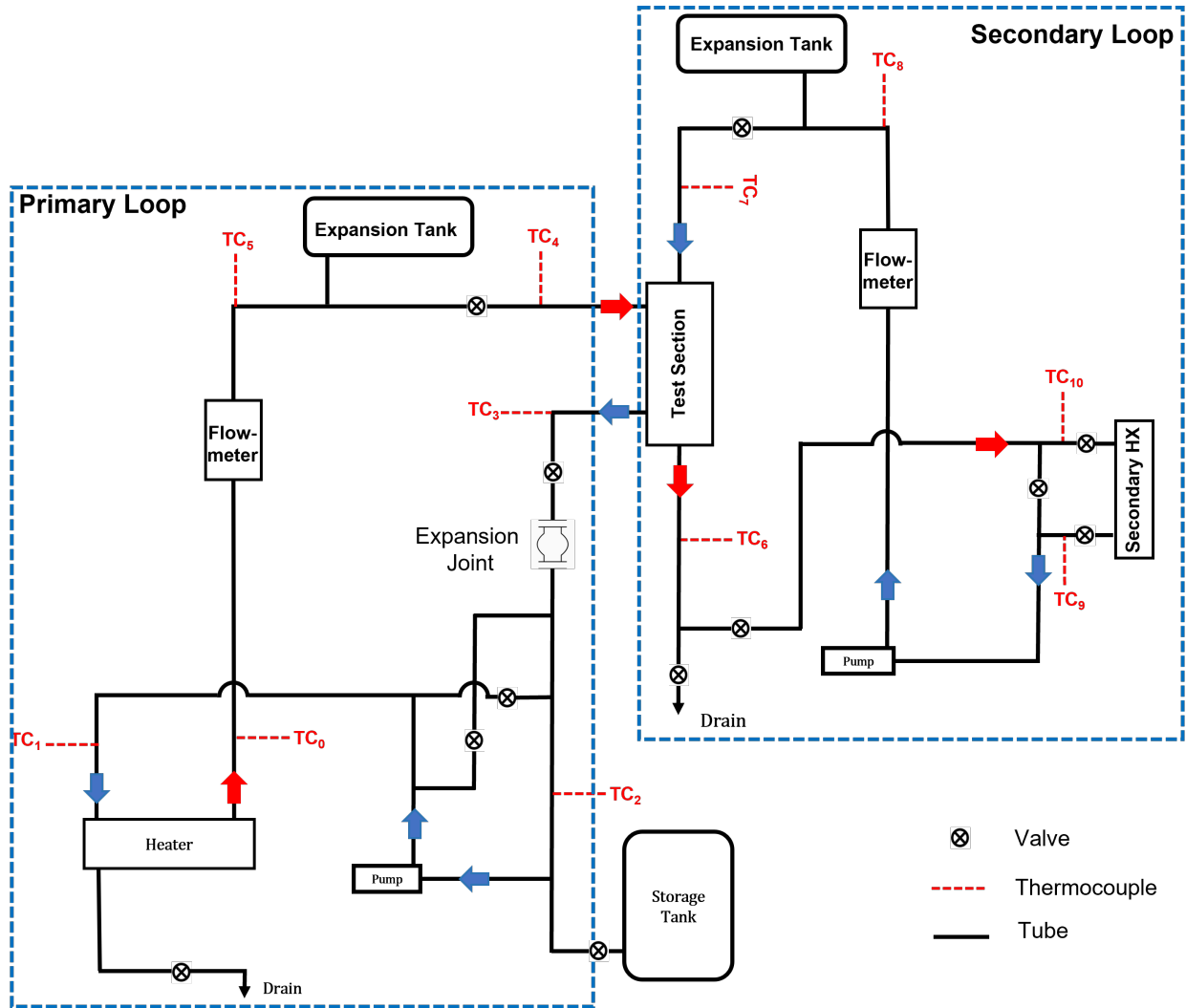


Figure 22: A simplified schematic of the primary and secondary loop for the intermediate heat exchanger (IHX) test facility.

Table 5: A brief summary of the various components used in the IHX test facility.

Part	Description	Serial/Part No.
Pumps	Price Pump Co. Centrifugal Pump	HP75SS-600-212764-100-18-3T6
Flowmeters	OPTISONIC 3400C, 0-250 GPM	Primary: A21041040 Secondary: A21041039
Thermocouples	OMEGA Type J stainless steel sheath	TQSS-14U-6 TQSS-18U-6
Secondary HX	KELVION Plate Type 31 bar	GBS 400H-60
Pressure	OMEGA 0-50 psig	PX309-050GI
Heater	INDEECO 30 kW, 3 phase, 2 stage, 160 psig, -20-250 °F	350-324685
Control Panel	INDEECO 34.5 kW, 208 V, 3 phase, 95.8 A	837U-324655
Data Acquisition	National Instruments CompactDAQ and terminal blocks	cDAQ-9174 Temp: NI 9214 Temp: NI TB-9214 Psi/flow: NI 9207 Psi/flow: NI 9923
Pump Control	Mitsubishi Electric VFD D700 3 phase, 200 V	V12R6H

the facility may often require reconfiguration when new heat exchangers are installed. The drip pan was also required to contain any fluids which may leak during reconfiguration of the loops, this is required since any spills are tightly monitored in the lab space.

The fluid flow portion of the facility is constructed using stainless steel Swagelock components for one inch Swagelock stainless steel tube which is used exclusively for both loops. Areas in which potential for vibration is high are insulated from the structural members using polymer dampeners. The fully constructed facility is shown in Figure 23 with various components highlighted.

3.4 Calibration

Before the test sections are placed in the IHX test facility it is necessary to determine the standard operating procedures and accuracy of the system, various initial tests aide in the refinement of these factors. Flowmeters and pressure transducers arrived from the suppliers

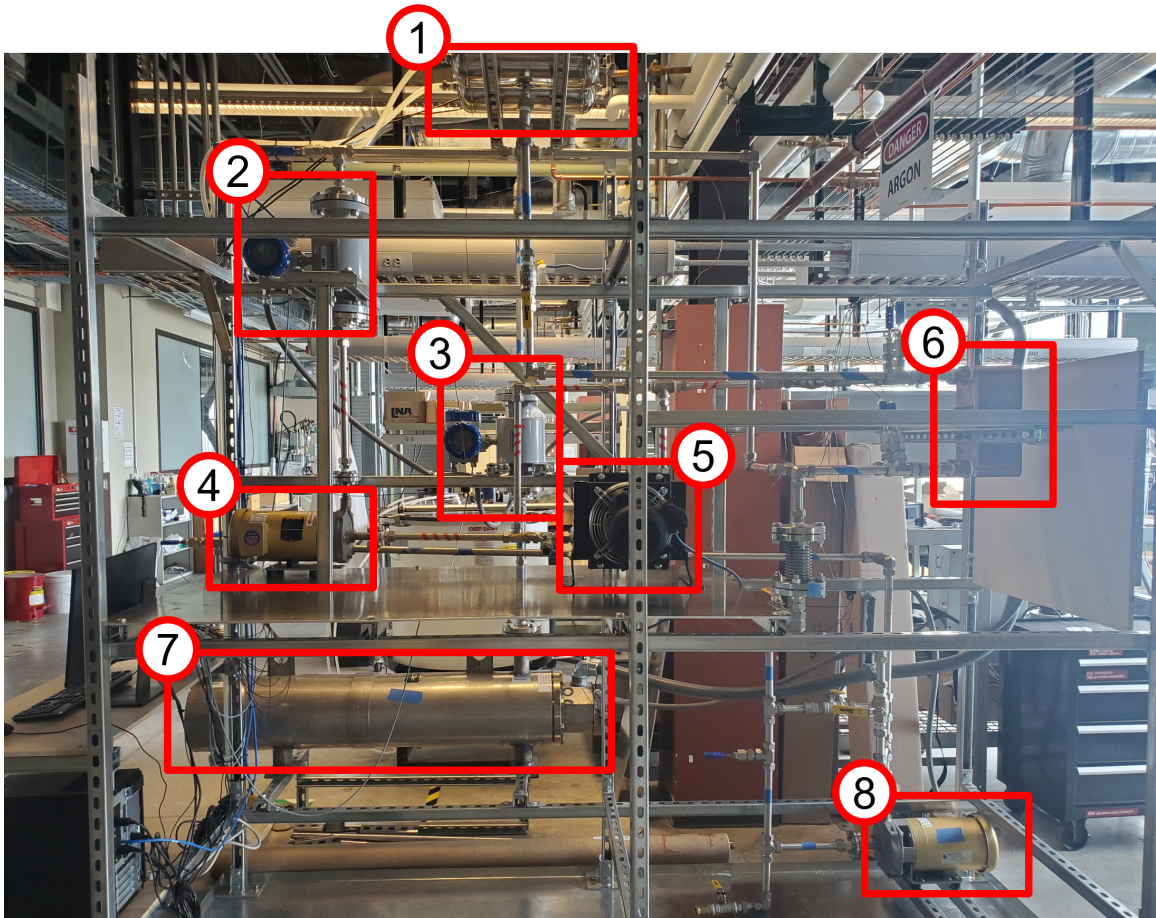


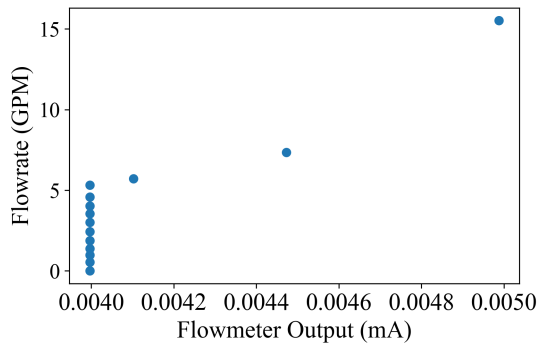
Figure 23: The test facility with certain components highlighted: 1) Expansion Tank, 2) Secondary loop flow meter, 3) Primary loop flow meter, 4) Secondary loop pump, 5) Location of the Secondary loop heat exchanger, 6) Location of the Test section, 7) 30 kW heater, 8) Primary loop pump.

with calibration data paperwork. The thermocouples were purchased from a reputable vendor and conform to ASTM E230 - ANSI MC 96.1 standards.

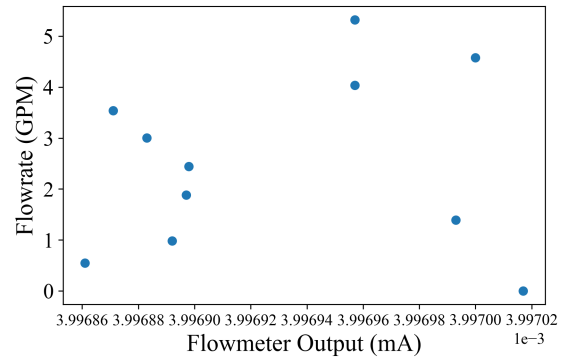
A benchmark test of the pumps include running at various VFD motor settings from the minimum of 3 Hz to a maximum of 60 Hz. During these runs it was observed that the flowrate output into the data acquisition software was different than the digital readout on the face of the flowmeter. It was determined that a calibration curve for the flowmeter should be determined in house. This calibration was done in 40 minute measurements at room temperature following the steps outlined below:

1. The pump is operated at the desired frequency for at least 10 minutes to ensure steady state conditions are met.
2. The data acquisition software is enabled recording the output of the flowmeter in mA.
3. An operator takes a manual reading from the digital screen on the flowmeter every 60 seconds.

The average value for flowrate was recorded at VFD settings of 0, 3, 5, 7, 9, 11, 13, 15, 17, 19, 21, 23, 30, and 60 Hz and are presented against the average flowmeter milliamp output in Figure 24a. This calibration curve using NI-9207 and NI-9923 parts to read the output of the flowmeter shows that below approximately 6 GPM the slope of the milliamp output vs flowrate trend appears extremely steep. Upon further investigation shown in Figure 24b it is apparent that signal noise convolutes the measurement for any flowrates below 6 GPM. Due to concerns for signal noise these measurements were repeated several times with varied results. It was determined that the error in measurement for flowrates below 6 GPM was inconsistent. This error is likely due to the noise in the signal, though it cannot be stated for certain without more advanced measurement devices and techniques. Though the signal noise is likely present in all of the outputs from the flowmeter, at the smaller mA outputs the influence of noise on the reading is amplified. For low flowrates, under 6 GPM the data



(a) The slope of the output vs flowrate for the flowmeter below 6 GPM appears extremely steep, the change in mA output at these ranges is heavily influenced by signal noise.



(b) A closeup of the first 11 measurements in (a), shows that the noise between these measurements is appreciable.

Figure 24: The flowmeter mA output vs flowrate trends show that signal noise dominates any measurement below 6 GPM. A different method for obtaining flowrate at these low values must be used.

acquisition method used displays low fidelity, for this reason a new method for gathering flowrate was used.

The method used for measuring flowrate in the facility is as follows. When a new heat exchanger is placed in the system or the loop is modified, manual measurements are taken. The manual measurements for pump VFD settings should be taken at minimum incremental values of 3, 7, 15, 30, and 60 Hz. For the target temperatures in subsequent experiments, further discretized measurements may be taken to refine the curves further if desired. For instance, if the test section is to be tested with hot and cold side temperatures of 80 °C and 20 °C respectively, then the loop should be maintained at 20 °C and manual measurements should be taken at VFD settings of 3, 7, 15, 30, and 60 Hz. The loop should then be heated to 80 °C and measured at the same frequencies. This will allow the operator to select the VFD setting on the motor for a desired flowrate. An example of this is depicted in Figure 25, where a specific flowrate of 6 GPM is highlighted on the primary loop flowrate Hz curve. These figures are presented in gallons per minute vs motor setting (Hz) for the operators ease of use since the flowmeters on the system readout in units of GPM. Some error may be introduced

here if the bulk temperature of the coolant in the respective loop is between the upper and lower range of experiment settings. To mitigate some of the error possibly introduced via this flowrate approximation a linear interpolation between hot and cold coolant flowrates is used. As shown in Figure 26, code was developed to increase operator ease of use. After the calibration values are input into the code directly, the program requires the user to select the desired loop, temperature of the fluid, and desired flowrate. Once these are selected the code uses linear interpolation to evaluate the motor setting value between the hot and cold flowrate calibration curves. These curves are fit to the calibration values using a second order polynomial. The program will then output graphically and numerically the VFD setting required so the loop will operate at the desired flowrate. For reference the code for this user interface is found in Appendix 4.6.5, calibration curve for this code were measured at 20 °C and 80 °C with a commercially available HX installed in place of the test section. The calibration curves for the new experimental HXs are reported in their respective topical sections.

3.4.1 Standard Operating Procedures

Standard operating procedures for the startup of the IHX facility are simplified and outlined as follows:

1. Verify all valves are in the desired position.
2. Verify the heater control panel is in the off position.
3. Verify all of the components are energized including pumps, flowmeters, VFDs, heater control panel, and computer.
4. Turn on flowmeters.
5. Activate LabVIEW to monitor operation values.
6. Run primary loop VFD at desired frequency/flowrate.

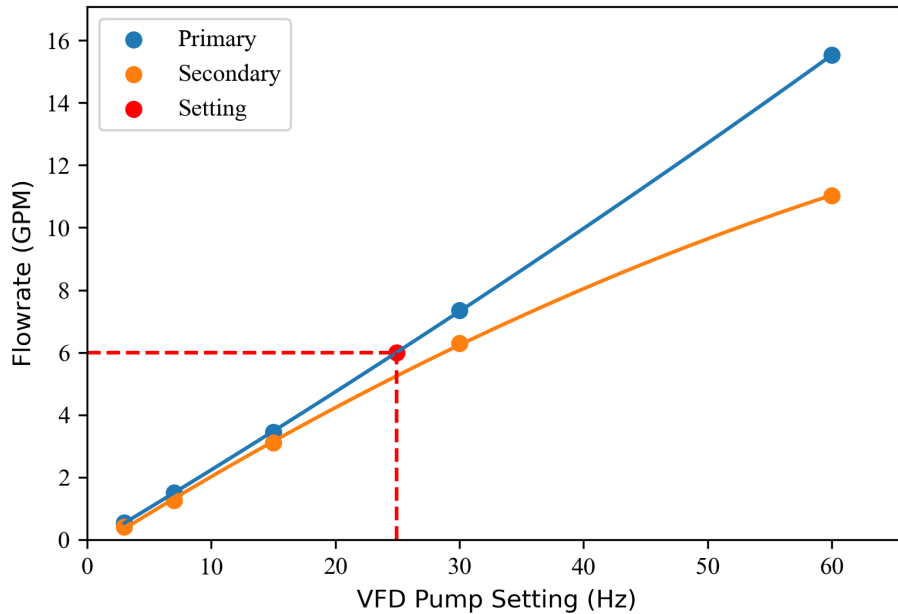


Figure 25: The curves for VFD pump setting vs flowrate for the test facility at room temperature (20 °C) with the Kelvion HX installed as the test section. These curves will change when any modification is done to the facility or the temperature is changed.

7. Verify flow is occurring by checking flowmeter readouts.
8. Turn on heater at control panel (Control Limit should be set to 50-100 °C above the heater set point).
9. Allow the primary loop to reach the set temperature and reach thermal equilibrium.
10. Turn on the cold water supply for the secondary loop.
11. Run the secondary loop VFD at the desired frequency/flowrate.

The shutdown of the facility may be conducted in several manners depending on the desired outcome. If no more testing is to be completed the heater must be turned off first then the rest of the components may be de-energized. It is important that the heater only be operated while the primary loop is full of coolant and running otherwise damage to the heater may occur.

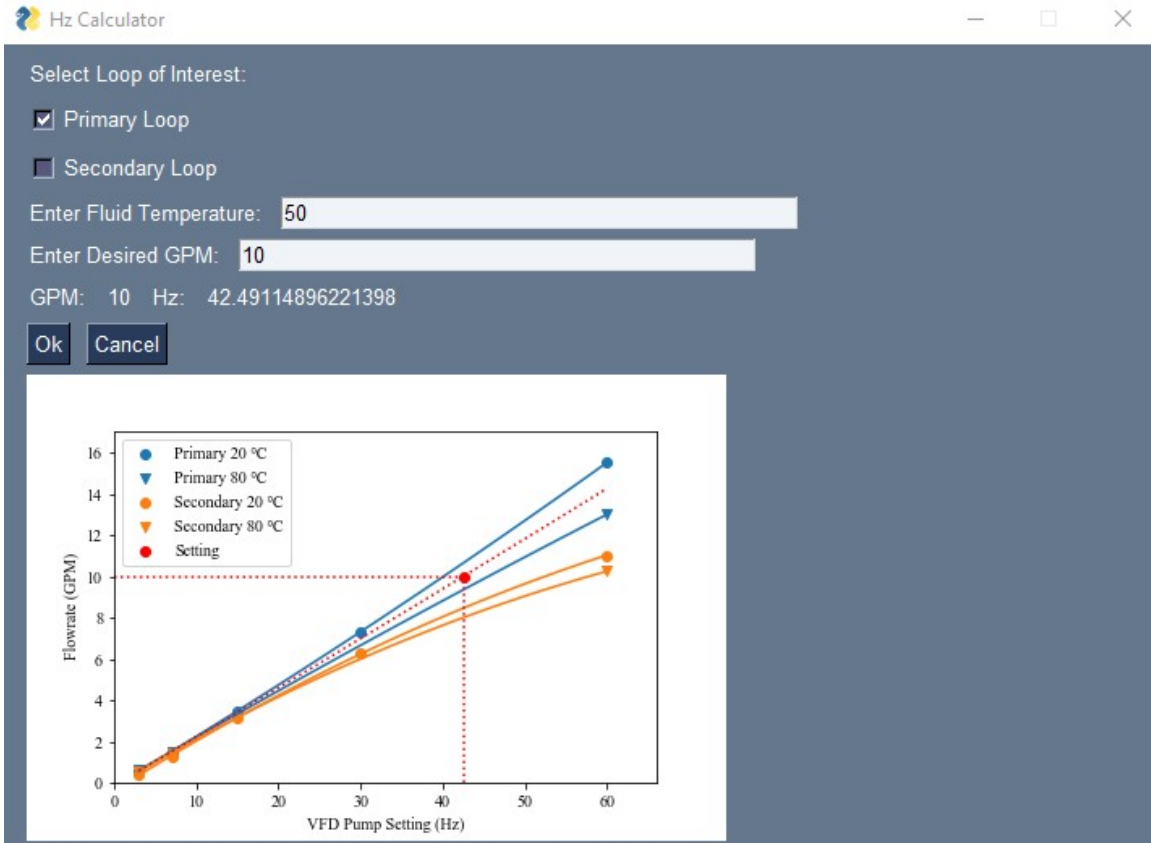


Figure 26: The user must select desired loop, fluid temperature, and desired flowrate. The program uses calibration data from the hot and cold flowrate measurements to approximate the VFD setting required to operate the loop at the desired flowrate.

1. The entire test facility is allowed to heat for approximately 2 hours with the test section operating at the desired hot and cold side temperatures.
2. The motors are set to the desired flowrate settings.
3. The hot and cold test section inlet temperatures are adjusted until the readings match the target values for the experiment.
4. Assuming that a steady state test is desired, the experiment will remain at the target operating setting until steady state conditions are reached.
5. Data acquisition is performed.

The directions above are generic and can be used in the design of experiment for future work with this test facility. Additional experiments should be considered to ensure that steady state conditions are reached. For further information concerning the steps taken during the measurements obtained in this study see Section 4.5.

3.5 Uncertainty Analysis

The uncertainty in thermocouple measurement shown in Figure 27 was provided by National Instruments NI-9214 specifications [45] and standard type T thermocouple uncertainties complying to ASTM E230 - ANSI MC 96.1. Values for type T thermocouple uncertainty are ± 1 °C or $\pm 0.75\%$ of the reading, whichever is greater. The uncertainty in pressure and flowrate measurements shown in Figure 28 was calculated using the gain and offset errors provided in National Instruments' documentation [46]. The calculation used to determine total error neglecting linearity error is

$$TotalError = GainError + OffsetError \quad (27)$$

where the values for gain error and offset error are $\pm 0.87\%$ of the reading and $\pm 0.05\%$ of the range respectively.

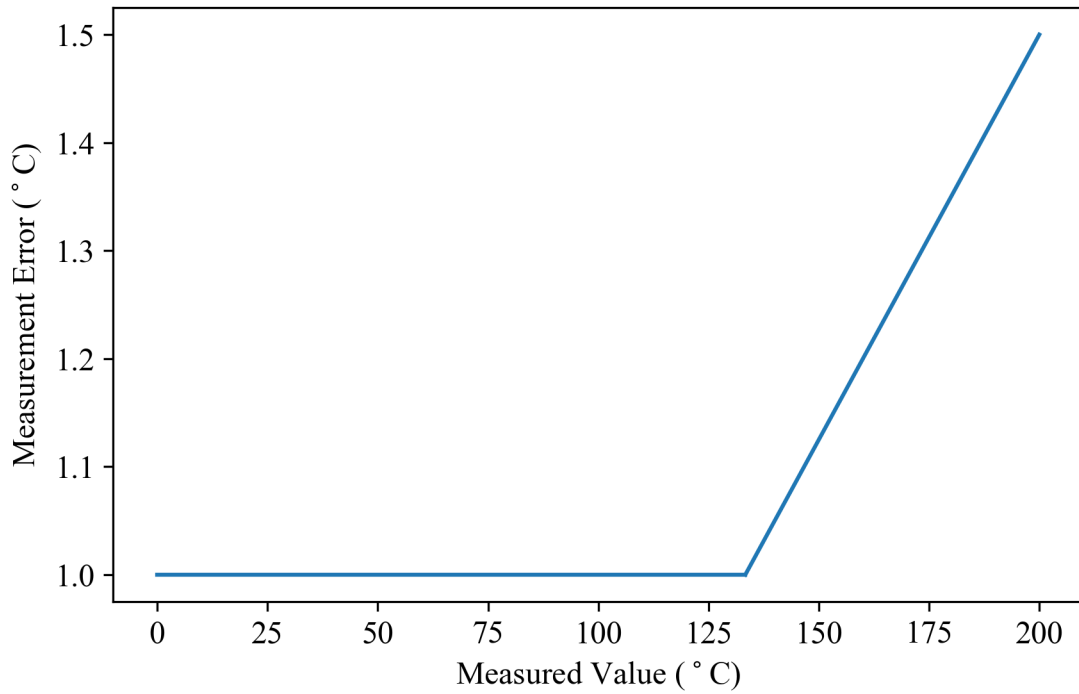
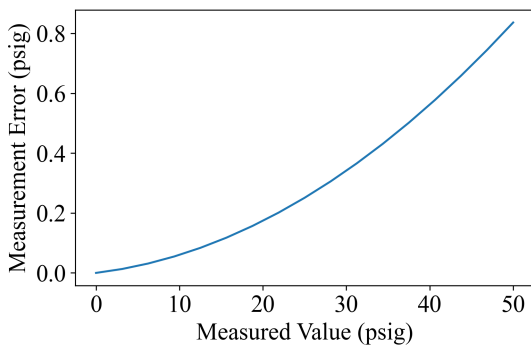
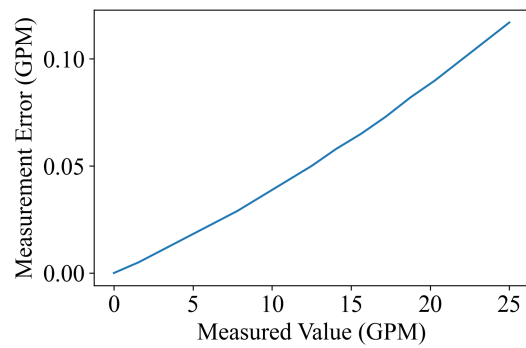


Figure 27: The maximum error for the temperature range in this study is ± 1 °C for a type T thermocouple measured using a NI-9214 with NI TB-9214 terminal block. The error in measurement above 130°C increases to $\pm 0.75\%$ of the reading.



(a) The measurement error in pressure is between 0 - 0.8 psig for the range of the sensor.



(b) The maximum measurement error at 25 GPM is approximately 0.117 GPM for the facility.

Figure 28: The measurement error for devices read using NI 9207 with NI 9923 terminal block, pressure of the left (a) and flowrate on the right (b).

Uncertainty propagation is of interest in this study since multiple temperature and flowrate measurements are used to obtain performance data. Since the performance of the heat exchanger is the main interest of this study, the uncertainties for wattage is of interest. The uncertainties in these values may be obtained using the product rule, which states that if $c = ab$ then the upper bound of uncertainty may be obtained using,

$$u_c = \left(\frac{u_a}{a} + \frac{u_b}{b} \right) 100 \quad (28)$$

where u_c is the uncertainty of the product of measured values a and b where each have respective uncertainties u_a and u_b . Since wattage is obtained using Eq. 1 the product rule applies. Since the uncertainty in wattage is only introduced through measurements of temperature and flowrate the uncertainty of wattage u_q may be defined as

$$u_q = \left(\frac{u_{\dot{m}}}{\dot{m}} + \frac{u_{\Delta T}}{\Delta T} \right) 100 \quad (29)$$

where $u_{\dot{m}}$ is the uncertainty in mass flow rate and $u_{\Delta T}$ is the uncertainty in temperature reading. For this case maximum uncertainty values of $7.36\text{E-}3 \text{ kg/s}$ (0.117 GPM) and 1°C were used for $u_{\dot{m}}$ and $u_{\Delta T}$ respectively. When paired with maximum anticipated mass flow rate and temperature drop values of 0.2519 kg/s (4 GPM) and 60°C respectively this equates to a maximum error in calculated wattage of 4.59%.

This however is a high estimate of uncertainty, the summation in quadrature method may provide a more accurate yet less conservative estimation of uncertainty. This is defined as

$$u_c(y) = \left[\sum_{i=1}^n [c_i u(x_i)]^2 \right]^{1/2} \quad (30)$$

where u_c is the combined uncertainty, c_i is the sensitivity coefficient, and $u(x_i)$ is the standard uncertainty. The maximum uncertainty in this case may be obtained using the theoretical minimum HX efficiency on the hot side of the HX, assuming an inlet and outlet temperature

of 80°C. The total combined uncertainty temperature drop across the HX for this case is 0.0906 °C. The total combined uncertainty for flowrate taken at the maximum of 0.2519 kg/s is 0.0008 kg/s. The uncertainty in flowrate and temperature combine to an equivalent uncertainty in wattage of 0.49%. With the estimation of uncertainty obtained via summation in quadrature being the least conservative estimation of uncertainty and the first method shown being the most conservative, it may be stated that the uncertainty in wattage measured in the system for water at a maximum temperature of 80 °C and flowrate of 0.2519 kg/s (4 GPM) is between 0.49% and 4.6%.

The uncertainty in reported values of heat transfer coefficient Nu may be similarly reported. Since Nu is defined as found in Eq. 2 the provisional rule applies. The uncertainty in h is calculated as

$$u_h = \left(u_q + \frac{u_{\Delta T}}{\Delta T} \right) 100 \quad (31)$$

using the values above the uncertainty in h is found to be a minimum of 0.64% and a maximum of 5.59%. Since in this case h is the only measured value with appreciable error the uncertainty in Nu is the same as h .

3.5.1 Data Acquisition - LabView

The commercial software LabVIEW is used to monitor, record, and manipulate the data from the IHX test facility. The front panel shown in Figure 29 displays live values for flowrate, temperature, and pressure at discrete points in the system. The locations of temperatures displayed here are approximately the same as those in the actual facility. The block diagram shown in Figure 30, shows the display, manipulation, and storage steps used for data handling. The block diagram shows that the time indexed data for temperature, wattage, flowrate, and temperature are exported to a .csv type data format to the users desired directory. The data recording feature of the program may be halted and resumed at any time during operation, though it is recommended that a new save file be initiated at the beginning of each experiment.

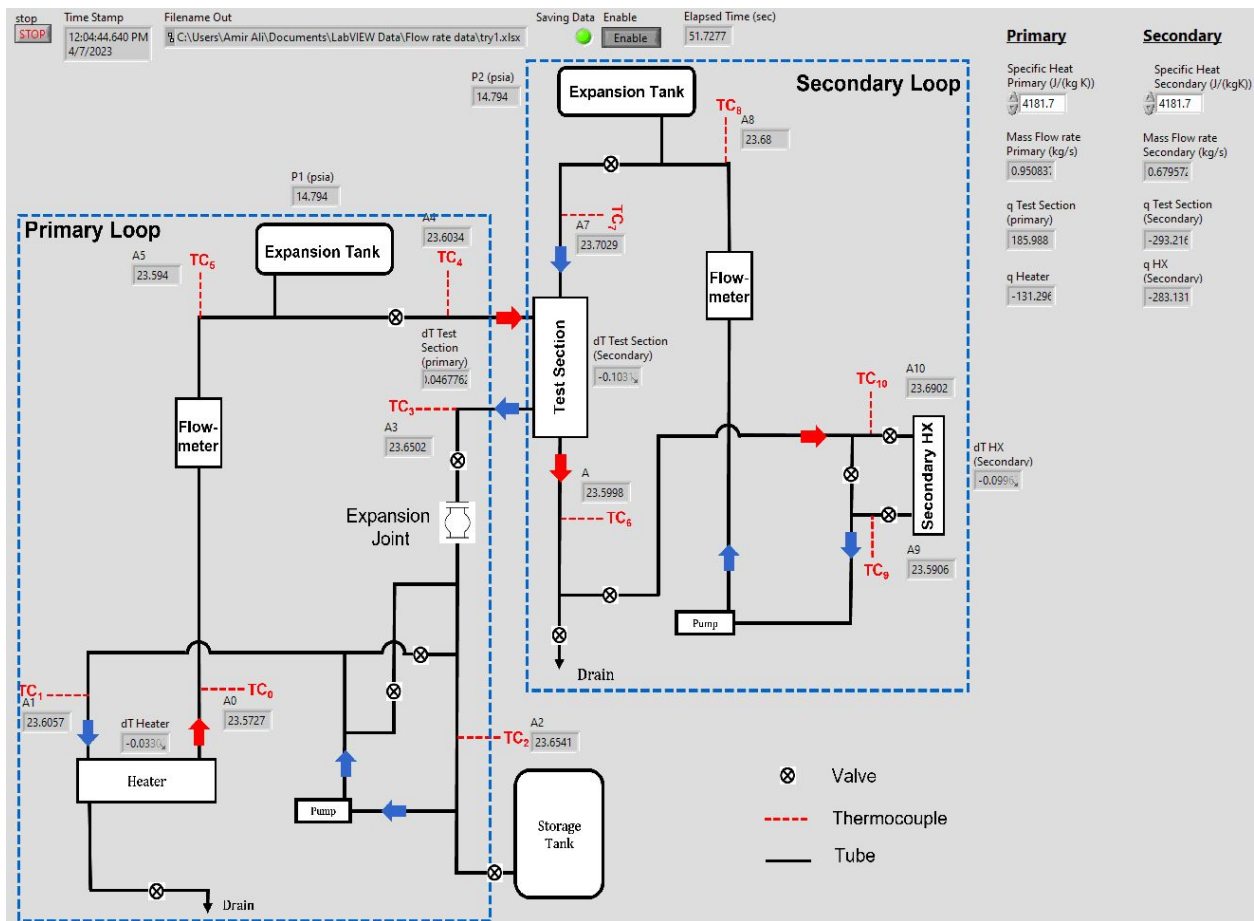


Figure 29: The front panel of the labVIEW program used to view live data for temperature, pressure, flowrate, and various wattages. The user may pause or resume data recording at any time using this panel.

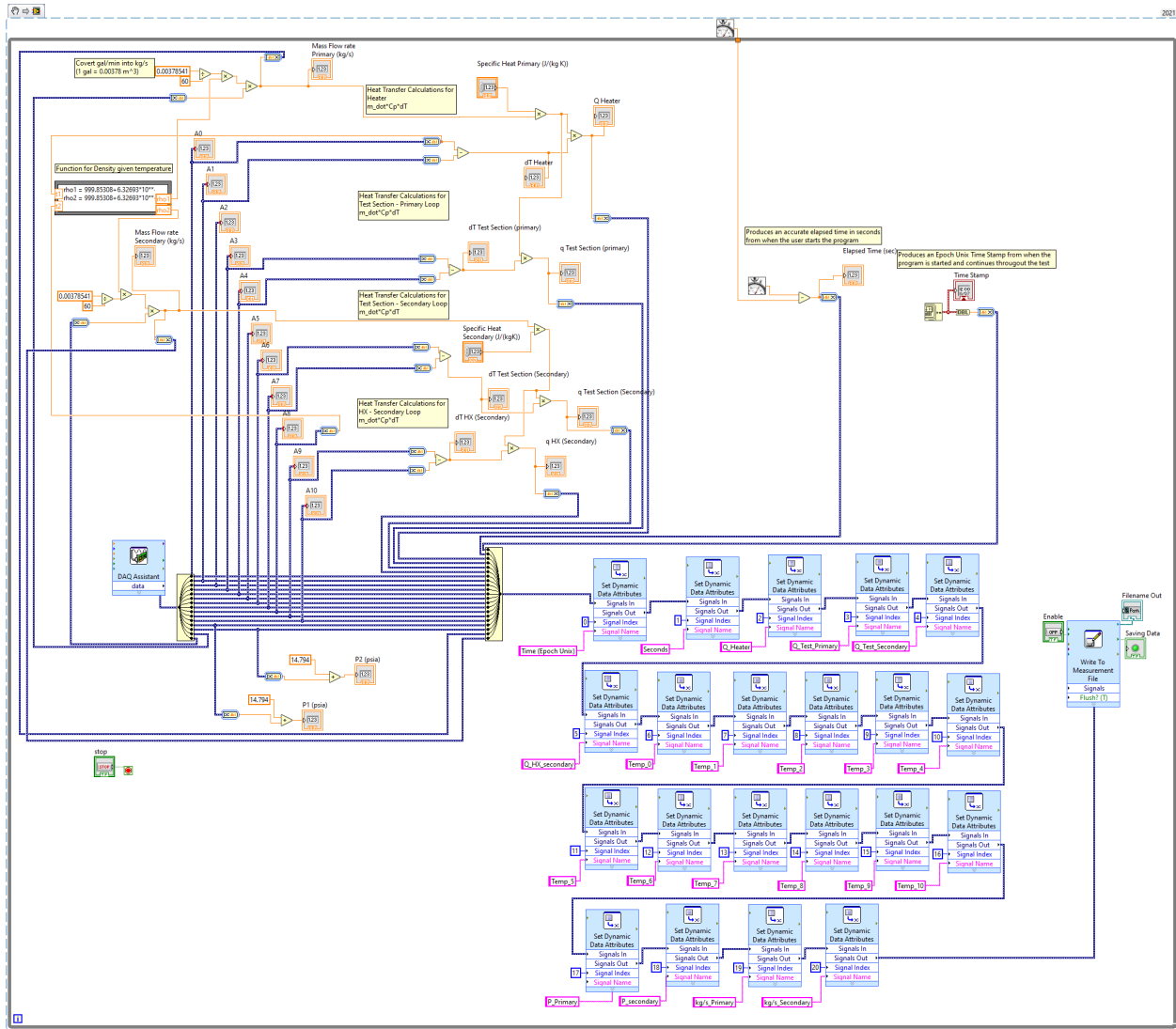


Figure 30: The block diagram for the LabVIEW program used to handle the data obtained from the data acquisition hardware. This program reads, manipulates, outputs, and records various data of interest.

Chapter IV: Experimental Results

4.1 Fabrication

Initial efforts were made for fabrication to be completed using the direct metal laser sintering (DMLS) process. Several quotes were obtained, however, it was deemed that the DMLS process would not be able to economically produce a HX of viable size for testing. The traditional manufacturing method of computer numerically controlled (CNC) machining was selected for manufacture. The HXs were designed in three main parts, top, center, and bottom components as shown in Figure 31. Flow guide vanes were also incorporated in the inlet plenum region to aid in dividing the flow between the various flow paths. To ensure that there is no flow passing between channels positive features were incorporated into the top and bottom components which mate to negative features in the center component as shown in Figure 32. The assembly is designed to have sealant applied in the negative features on the center plate prior to assembly. The top and bottom plates will then be bolted together and welded along the periphery. The guide vanes and bolt ends are also welded to ensure a water tight fit.

This design will produce fluid volumes as shown in Figures 33 and 34. The cost to manufacture the oval twisted geometry in this size was approximately 67% more than the circular counterpart.

The parts were manufactured out of 316L stainless steel using CNC machining with basic tolerancing of approximately ± 0.005 inches. Instrumentation to measure surface roughness was not available. Visual inspection was completed before assembly to ensure no burrs, excessive chatter, or large surface defects were present. Images of the fully machined components in unassembled and assembled configurations are shown in Figures 35 and 36.

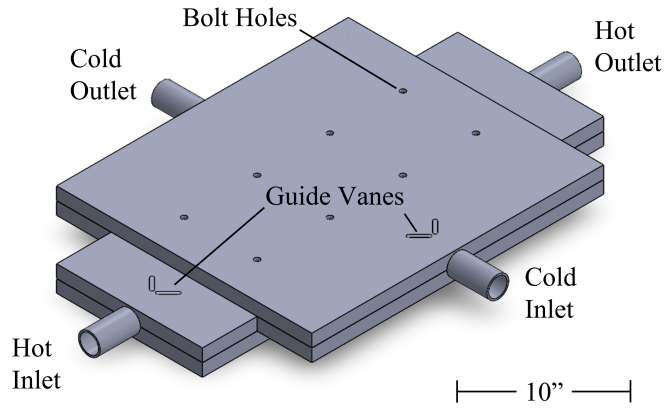


Figure 31: An isometric view of the entire assembly, the cold side is the top portion while the hot side is the bottom portion.

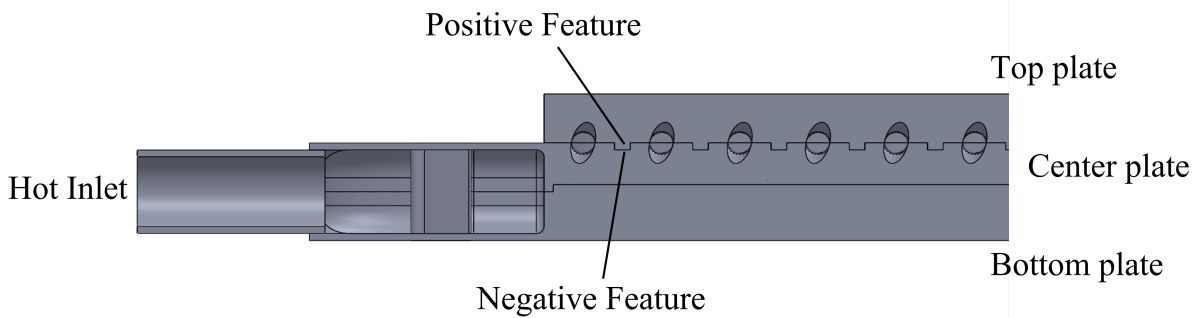
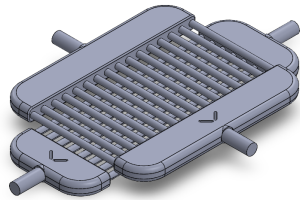
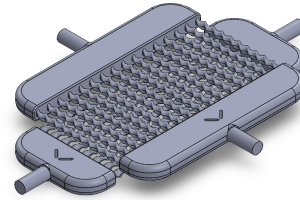


Figure 32: The positive and negative features machined into the parts are toleranced closely and filled with a small amount of sealant prior to assembly to ensure that there is no cross-flow between flow paths.

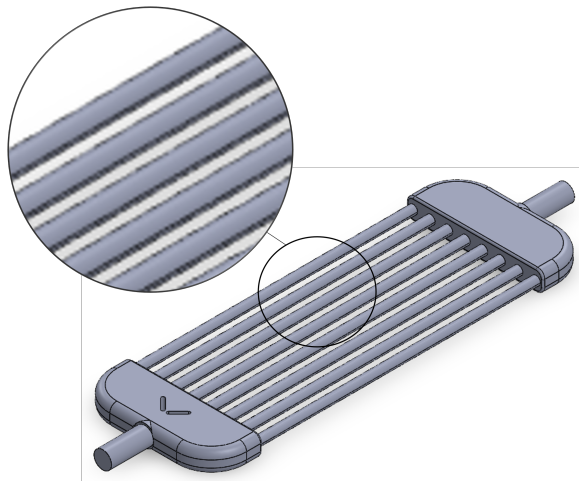


(a) Detail of the circular profiled HX top and bottom volumes.

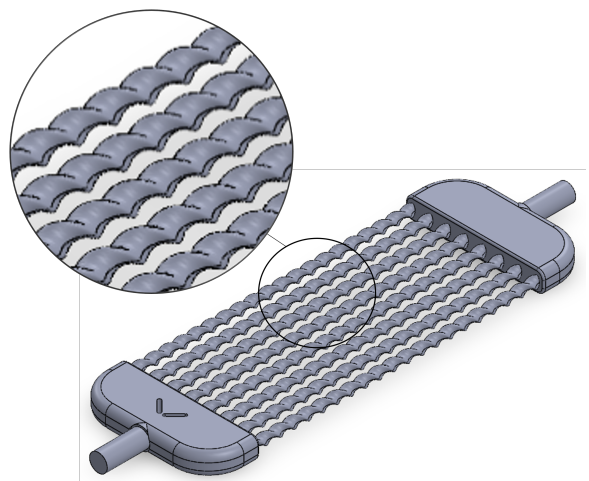


(b) Detail of the oval twisted HX top and bottom volumes.

Figure 33: Two heat exchangers are to be fabricated, one with a circular flow path cross section (a) as the baseline, and one with oval twisted flow paths (b).



(a) A close detail showing the circular cross section flow paths.



(b) A close detail showing the oval twisted cross section flow paths.

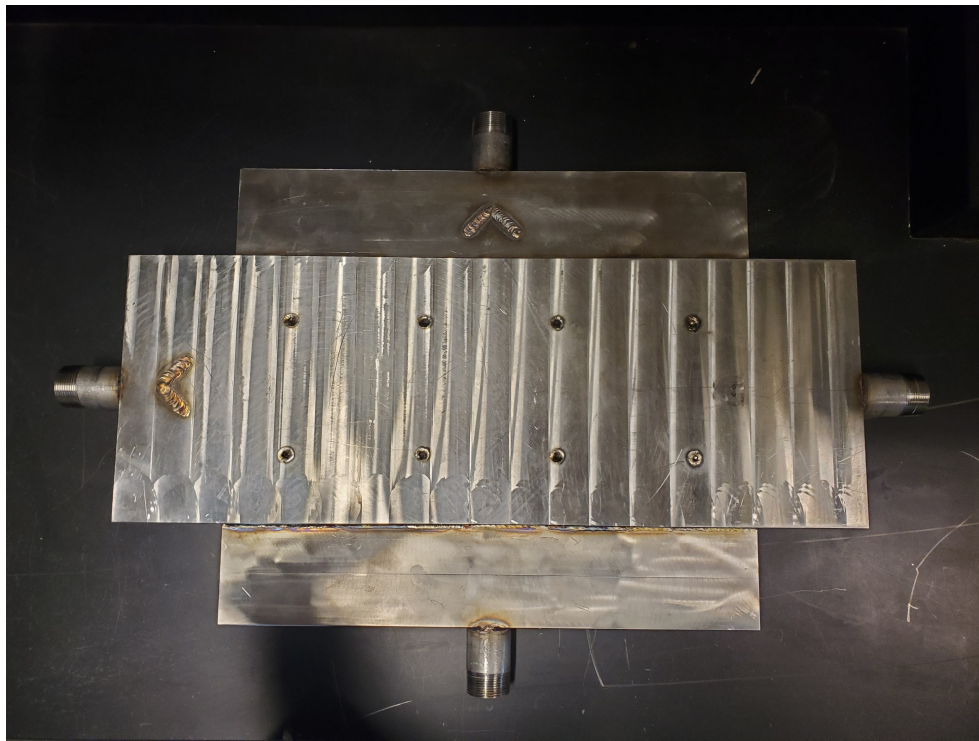
Figure 34: Details showing the marked difference between the circular cross section volume and the oval twisted cross section volume. Both volumes shown are the bottom (hot) fluid volumes.



(a) Top volume of the circular flow path HX shown before welding. The top plate (top) and center plate (bottom) are shown here.



(b) Bottom volume of the circular flow path HX shown before welding. The bottom plate (top) and center plate (bottom) are shown here.



(c) The fully assembled and welded circular cross section HX show prior to installation in the test facility.

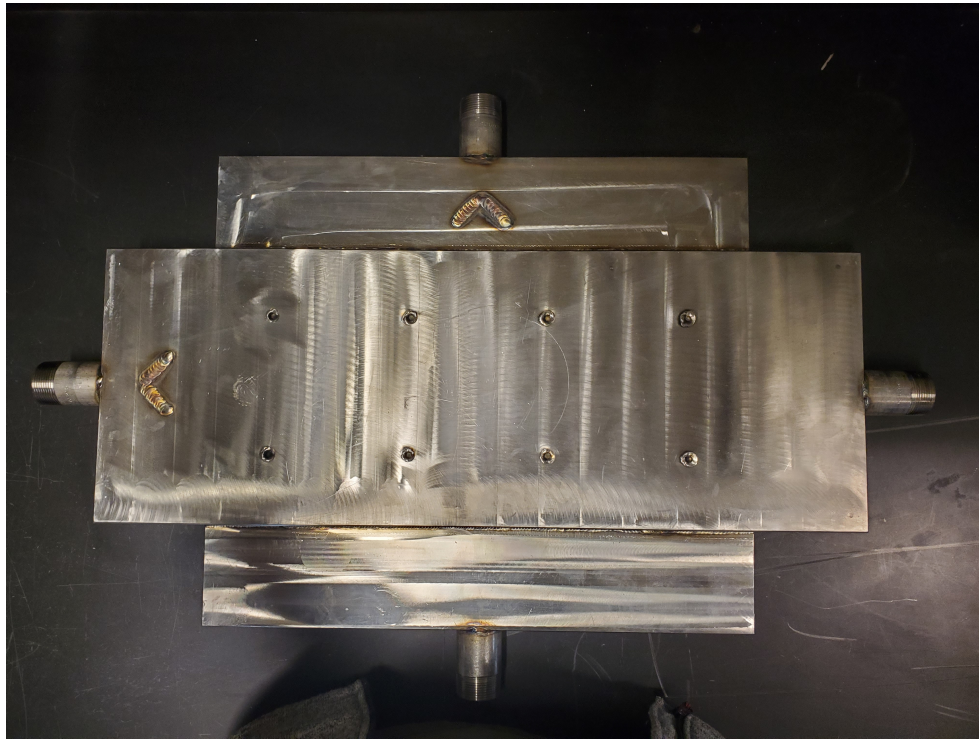
Figure 35: The various components of the circular HX shown, the top volume (a) bottom volume (b), and fully assembled welded circular HX (c).



(a) Top volume of the oval twisted flow path HX shown before welding. The top plate (top) and center plate (bottom) are shown here.



(b) Bottom volume of the oval twisted flow path HX shown before welding. The bottom plate (top) and center plate (bottom) are shown here.



(c) The fully assembled and welded oval twisted design HX shown prior to installation in the test facility.

Figure 36: The various components of the oval twisted HX shown, the top volume (a) bottom volume (b), and fully assembled welded oval twisted design HX (c).

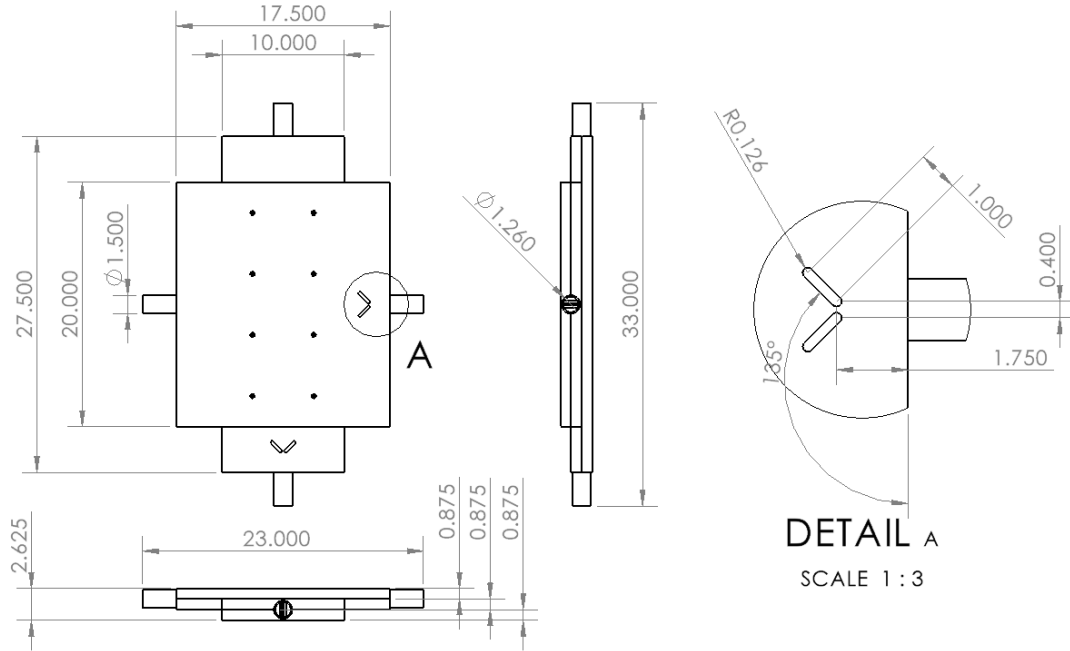


Figure 37: The outside dimensions for both the circular and oval twisted designs.

4.2 Design Dimensions

The dimensions of the oval twisted design as shown in Figures 37 - 40 and the circular design are identical, with the exception of the internal tubes. The diameter of the internal tubes for the circular geometry HX are 0.624154 in. and 0.624239 in. for the top and bottom tubes respectively. These diameters are the diameters for the circular tubes which produce a surface area equal to the surface area of the corresponding oval twisted tubes. The oval twisted tube twist pitch is 2 in. as shown in Figure 40 the pitch is the same for the top and bottom oval twisted tubes.

4.3 Installation

The facility was designed to support easy installation of new heat exchangers for testing. The heat exchanger were installed, insulated and tested one at a time as shown in Figure 41. It should be noted that other than at the inlet and outlet pipes the heat exchanger at no point is contacting a highly conductive material. The test section is resting on a piece of

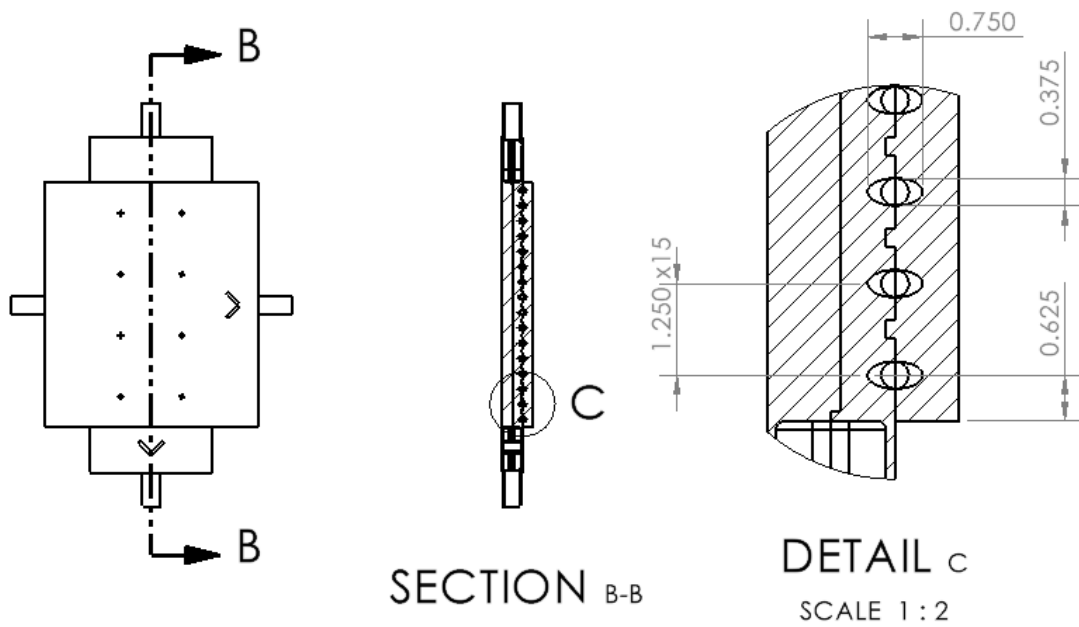


Figure 38: The dimensions of the ellipse in the oval twisted design including spacing and arrangement to the top cold fluid volume.

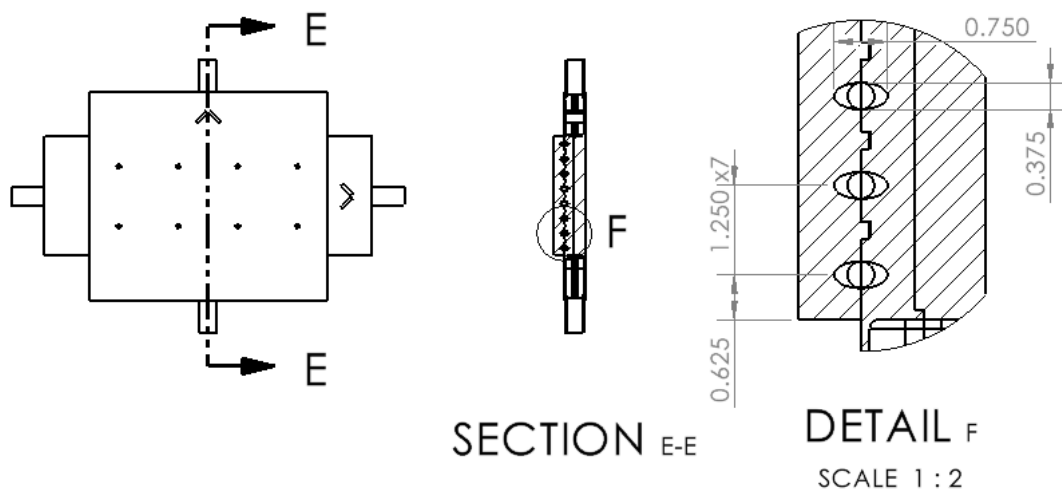


Figure 39: The dimensions of the ellipse in the oval twisted design including spacing and arrangement to the bottom hot fluid volume.

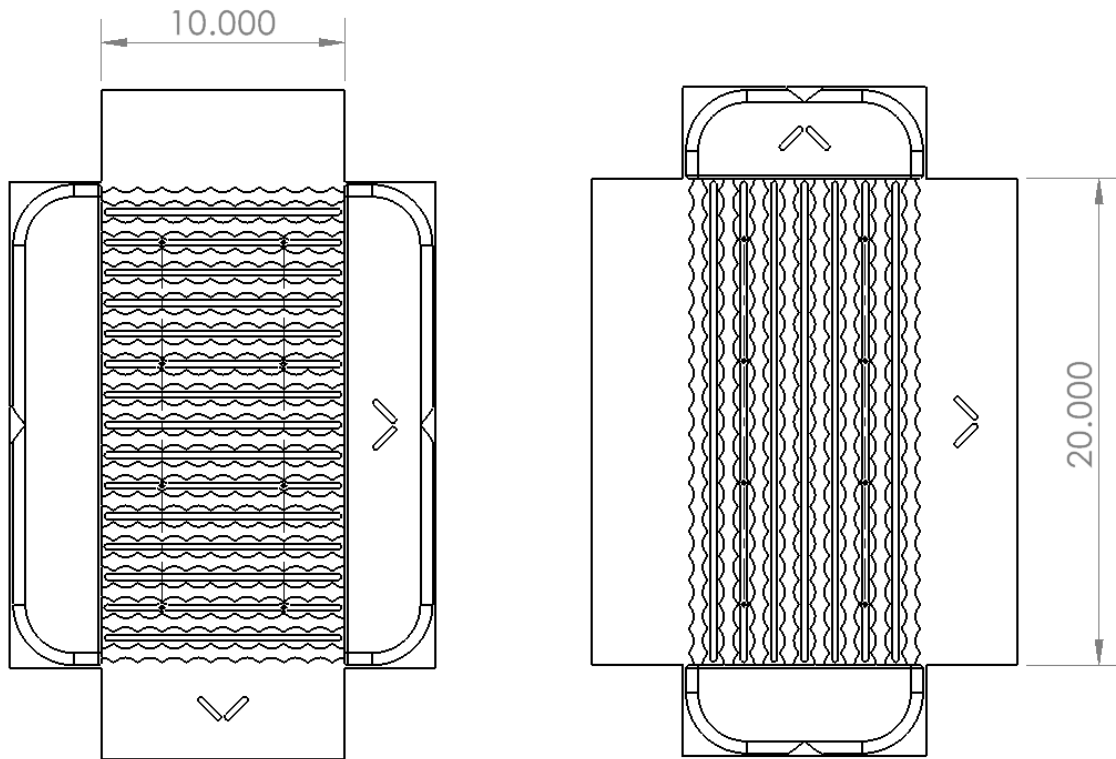


Figure 40: A view of the top and bottom of the center plate to show the lengths of the flow paths. These lengths are the same for the oval twisted and circular designs.



(a) A test section shown installed and uninsulated.



(b) A test section shown installed and insulated with two sheets of fiberglass insulation top and bottom.

Figure 41: A HX shown installed before insulating (a) and after insulation is applied (b).

rigid foam measuring approximately 3x3x3 inches to support the assembly weight. All other surfaces of the HX are covered in two layers of fiberglass insulation sheets with a density of 0.95 lbs./cu.ft. and single sheet heat flow rate of 0.26 BTU at 75 °F. The inlets and outlets of the HX are covered past the location where inlet and outlet temperatures are measured.

4.4 Operation Plots

The flowrates at motor settings of 3, 7, 15, and 30 Hz were manually recorded at hot and cold operating conditions. The manual recording occurred taking a visual measurement of the flowmeter every 30 seconds for 20 minutes. These measurements stopped at a VFD motor setting of 30 Hz since this motor setting was adequate to reach the maximum test flowrate of 0.2519 kg/s . A second order polynomial with linear interpolation between temperatures is used to approximate the motor setting at the desired flowrate, see section 3.4 and Appendix B for more information on the program and calculations used to accomplish this. As shown

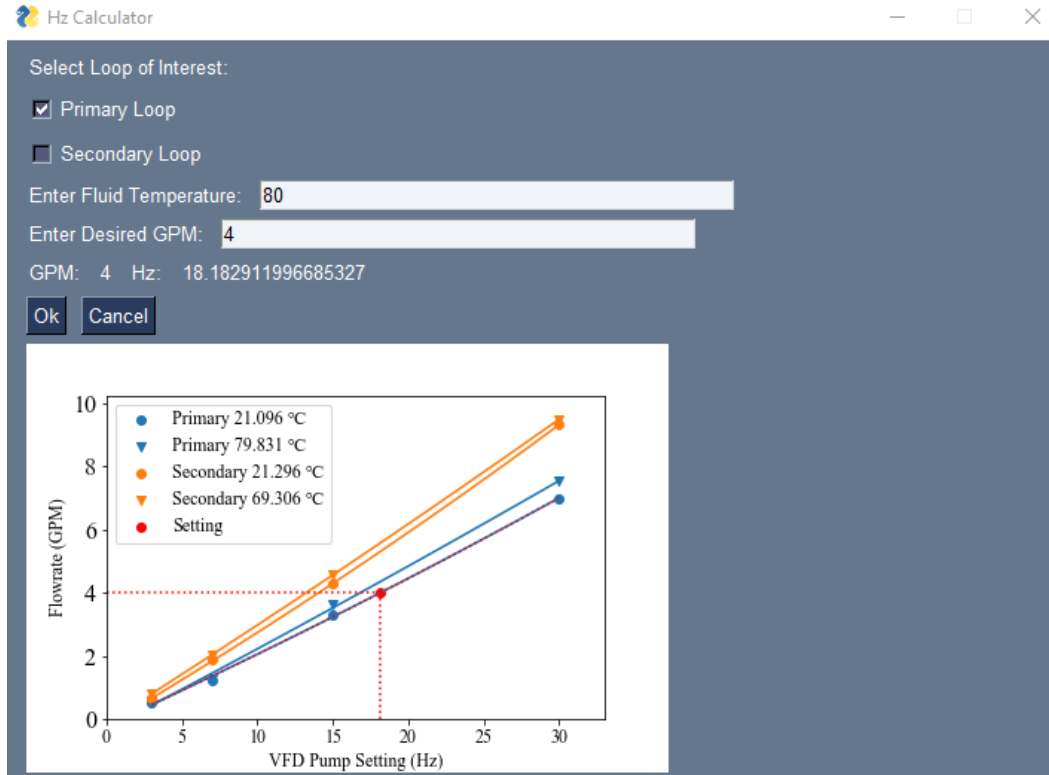


Figure 42: The calibration curves for the primary and secondary loops at 20 and 80 °C with the circular heat exchanger installed.

in Figures 42 and 43, the flowrate calibration curves for the circular and oval twisted test sections prove to follow a clear trend, and the curves used to determine flow rate between measured motor settings fit well for the secondary loop cold working fluid. However, the curves for the primary loop at high operation temperatures and low flow rates prove to be sporadic. Though this occurs for both circular and oval twisted assembly flowrate measurements, this is more clear in Figure 43 in the bottom left hand corner where it is apparent that the flowrate measured at 80 °C below 0.063 kg/s (1 GPM) does not fall on the proposed calibration curve. This point was measured several times and yielded continually inaccurate readings. As tests were completed in the future it was made apparent that flowrate measurements in this region on the hot side of the HX are not sufficiently reliable. For this reason any data generated including a hot side flow rate under 0.063 kg/s is not reported.



Figure 43: The calibration curves for the primary and secondary loops at 20 and 80 °C with the oval twisted heat exchanger installed.

4.5 Test Parameters

For the duration of the experiments data was gathered as follows:

1. The entire test facility is allowed to heat under flowing conditions for approximately 2 hours with the test section hot inlet operating at 80 °C and the test section cold inlet operating at 20 °C.
2. The motors are set to the desired flowrate settings.
3. The hot and cold test section inlet temperatures are adjusted until the readings are 80 ± 0.5 °C and 20 ± 0.5 °C respectively.
4. These settings are monitored for at least 5 minutes and must remain within the set range during this interval.
5. Data acquisition begins and occurs every second for a period of 10 minutes (600 measurements).
6. If the maximum or minimum value in inlet temperatures is without of ± 0.5 °C of the desired temperature the experiment restarts at step 3.
7. The standard deviation is calculated for each temperature measurement; if the standard deviation is greater than 0.5 the test is restarted at step 3.
8. The average values for T_{hi} , T_{ho} , T_{ci} , T_{co} are calculated from the separate 600 measurements. These averaged values are used for further calculations.

To ensure that steady state conditions are reached this procedure was used exclusively. The dwell time of 5 minutes at temperature prior to data acquisition as stated in step 4) was deemed adequate to reach steady state conditions through a series of separate tests. At the lowest and highest combination of flow rates a set of data was gathered using the steps listed above. At the conclusion of the test the system settings were not changed and the

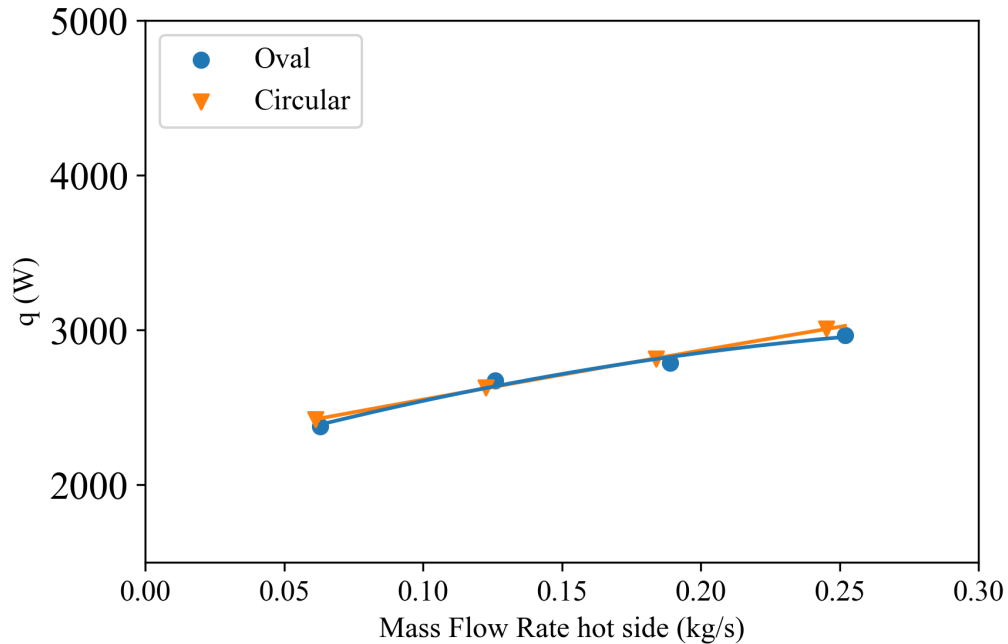


Figure 44: The difference in wattage between circular and oval twisted geometries is largely unnoticeable when the cold side flow rate is fixed at 0.0315 kg/s ($\approx 0.5 \text{ GPM}$).

system was allowed to run for over 1 hour. At the conclusion of an hour another 10 minute measurement was taken. These long dwell time measurements are accurate to within 0.1 % of the 5 minute dwell time measurements. This indicates that a dwell time of 5 minutes at target temperature is sufficient to reach steady state conditions.

4.6 Results

4.6.1 Imbalanced Flow

When the heat capacity ratio C_r varies this accurately reflects many real-world flow parameters. In Figure 44, the cold side of the HX is fixed at 0.03149 kg/s and the hot side of the HX is swept from $0.06298 - 0.2519 \text{ kg/s}$. At this low cold side flow rate the wattage for the oval twisted and circular geometries is the mostly identical. The trend of increased wattage with increases in hot side flow rate is expected, here the limiting factor for wattage is the cold side flow rate. When the cold side is fixed at 0.2519 kg/s as shown in Figure 45 there is

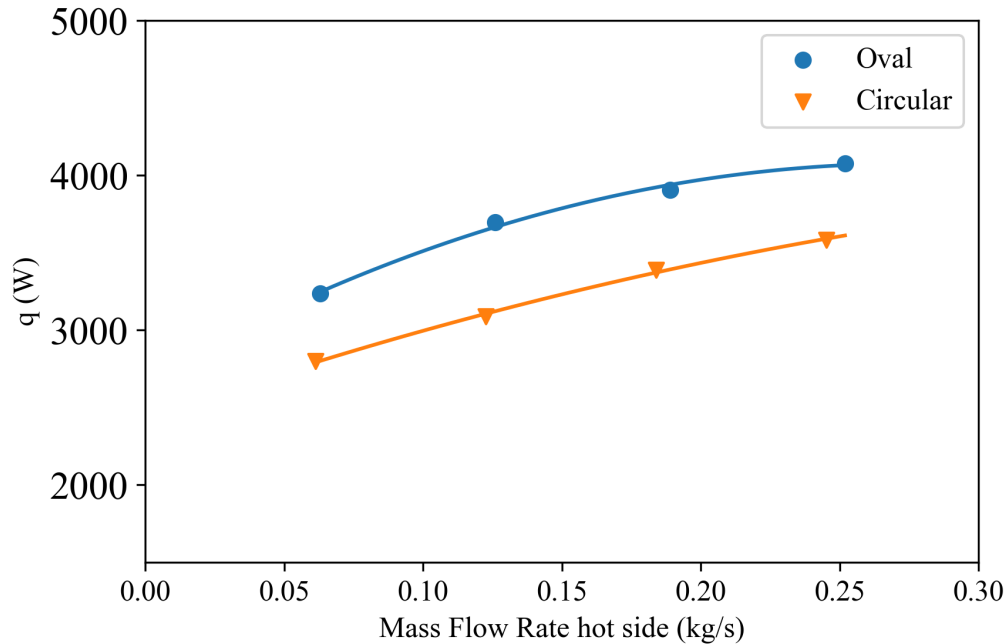


Figure 45: When the cold side is fixed at 0.252 kg/s ($\approx 4 \text{ GPM}$). The improvement in wattage is drastic with increases between 13.7 and 19.7%.

a noticeable improvement in wattage for the oval twisted geometry compared to the circular geometry. The improvements in wattage when changing from circular to oval twisted flow paths is between 13.7 - 19.7%.

The values for Nu may also be considered since it takes into account the thermal conductivity of the fluid and the heat transfer coefficient. When the cold side flow rate is fixed at 0.03149 kg/s as shown in Figure 46 the improvement in Nu is not noticeable. However as with wattage, when the cold side is fixed at 0.2519 kg/s as shown in Figure 47 the oval twisted geometry again displays heat transfer improvements over the circular geometry. These improvements range between 14.9 and 19.2% indicating superior heat transfer performance at higher flow rates.

4.6.2 Balanced Flow

When the heat capacity ratio is equal to one, comparison of the cold and hot sides of the HX become more clear. As shown in Figure 48, the cold side 48a and hot side 48b present

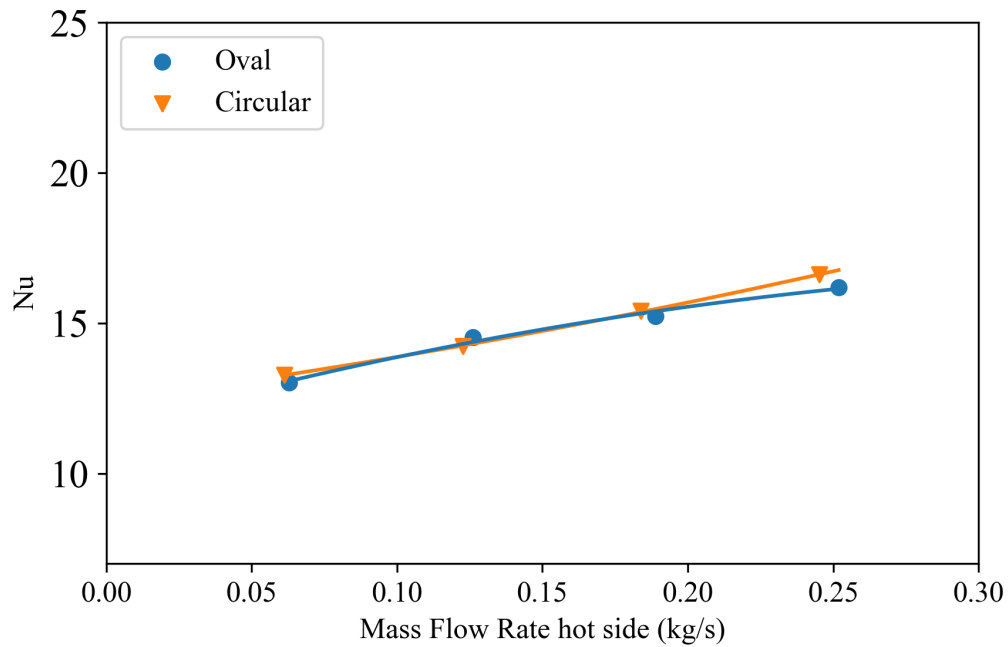


Figure 46: When the cold side is fixed at 0.03149 kg/s the only noticeable difference in wattage occurs when at high hot side flow rates with the circular geometry showing slight improvements of approximately 10.7%.

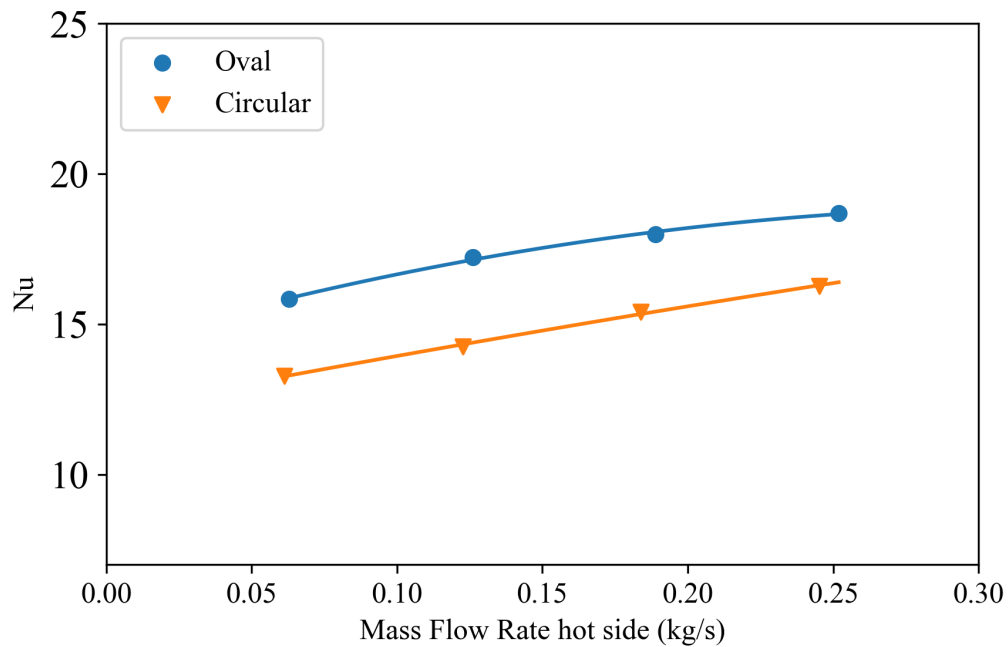
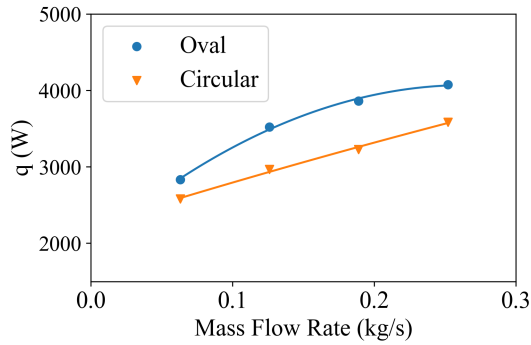
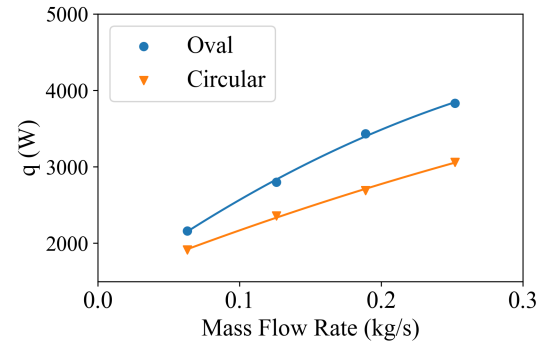


Figure 47: When the cold side is fixed at 0.252 kg/s ($\approx 4 \text{ GPM}$). The improvement in Nu is drastic with increases between 14.9% and 19.2%



(a) The improvement in wattage for the cold side of the HX for the oval twisted geometry is between 9.9% and 18.5% when compared to the circular geometry.



(b) The improvement in wattage for the hot side of the HX for the oval twisted geometry is between 13.1% and 24.9% when compared to the circular geometry.

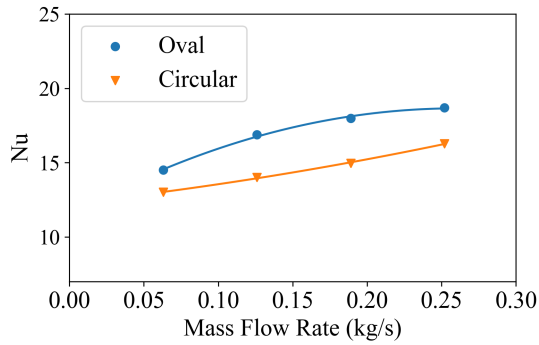
Figure 48: The difference in wattage between the hot and cold sides of the HX vary drastically with approximately 12% - 31% difference in the oval HX and 20% - 52% difference in the circular geometry.

drastically varied wattages. These wattages vary approximately 12 - 52% with the cold side presenting higher wattages in each case. It can be noted though that the improvement in wattage is evident in both the hot and cold sides of the HX. On the cold side of the HX the oval twisted geometry shows a maximum improvement of 18.5% over the circular geometry, the hot side similarly shows a maximum improvement of 25%.

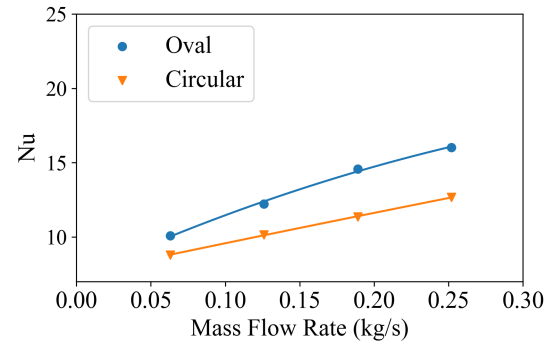
The analysis of Nu shows similar results as shown in Figure 49 where the hot and cold side Nu vary. The difference in Nu between hot and cold sides is between 23% and 67%. The trend in improvement for the oval twisted geometry remains and is between 11.5% and 28.3%.

Overall heat transfer coefficient plotted against mass flow rate in balanced flow conditions shown in Figure 50, indicates marked improvement when compared to the circular flow path geometry. Improvements between 15.6% and 25.1% are experienced for the oval twisted design.

Each of these parameters may be presented in terms of performance increase. This is done by calculating the ratio of performance; for wattage this is $q_{oval}/q_{circular}$, Nu is



(a) The improvement in Nu for the cold side of the HX for the oval twisted geometry is between 11.5% and 20.6%



(b) The improvement in Nu for the hot side of the HX for the oval twisted geometry is between 14.7% and 28.3%

Figure 49: The difference in Nu between the hot and cold sides of the HX vary drastically with approximately 23% - 44% difference in the oval HX and 31% - 67% difference in the circular geometry.

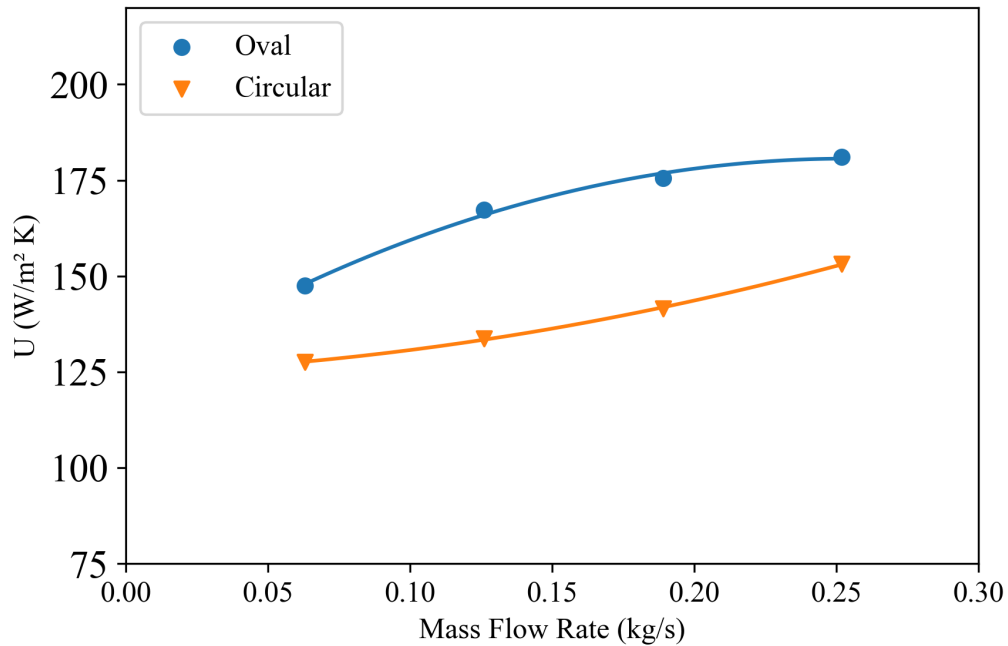


Figure 50: The oval twisted HX shows an increase in overall heat transfer coefficient between 15.6% and 25.1% when compared to the circular counterpart.

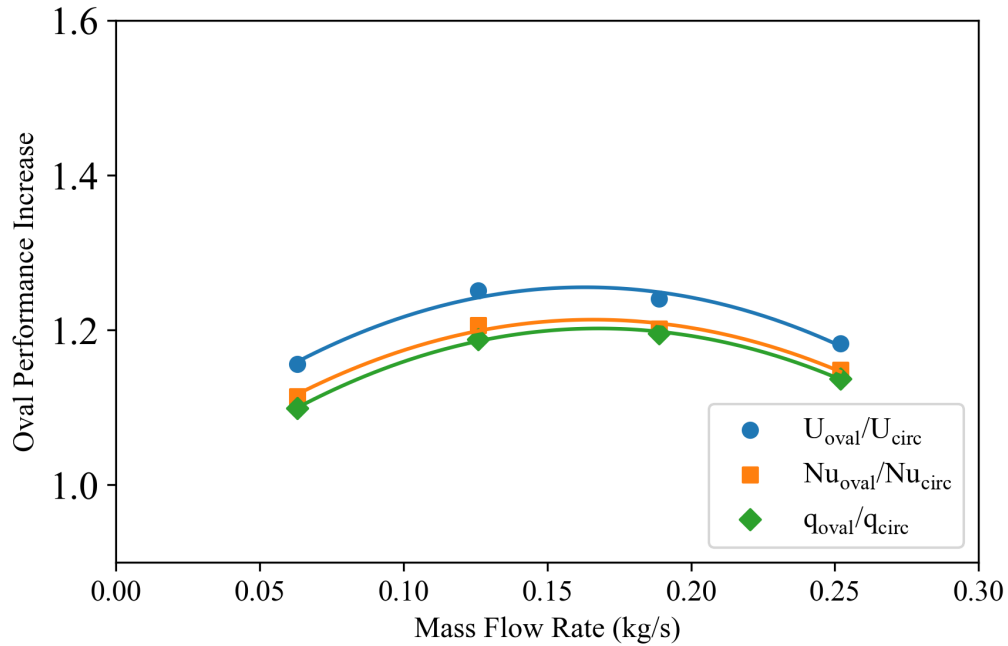


Figure 51: The increase in performance for U , Nu , and q are greater than unity for all cases. The highest performance increase of 1.2 noted here occurs at approximately 0.17 kg/s .

$Nu_{\text{oval}}/Nu_{\text{circular}}$, and U is $U_{\text{oval}}/U_{\text{circular}}$. As shown in Figure 51 the oval twisted HX outperforms the circular counterpart in every parameter. Since the curve trends downwards at lower and higher flowrates it may be stated that the maximum performance increase occurs at 0.17 kg/s .

4.6.3 Entropy Generation

The calculated entropy generation number as shown in Figure 52 is much higher than anticipated in the CFD work and in literature [39]. Though the slope of the line found in literature is different, this is expected since the non-dimensionalization of entropy generation allows for the comparison of unlike HXs; and Hesselgreaves does not mention the type of HX in the analysis provided. Prior analysis and this provide corroboration that as C_r decreases the slope of the effectiveness vs N_{s1} plot trends towards zero. This tendency is noted in both the circular and oval twisted design as shown in Figures 52 and 53. With values maxing out at approximately 240% - 350% higher than the CFD values. These high losses due to entropy

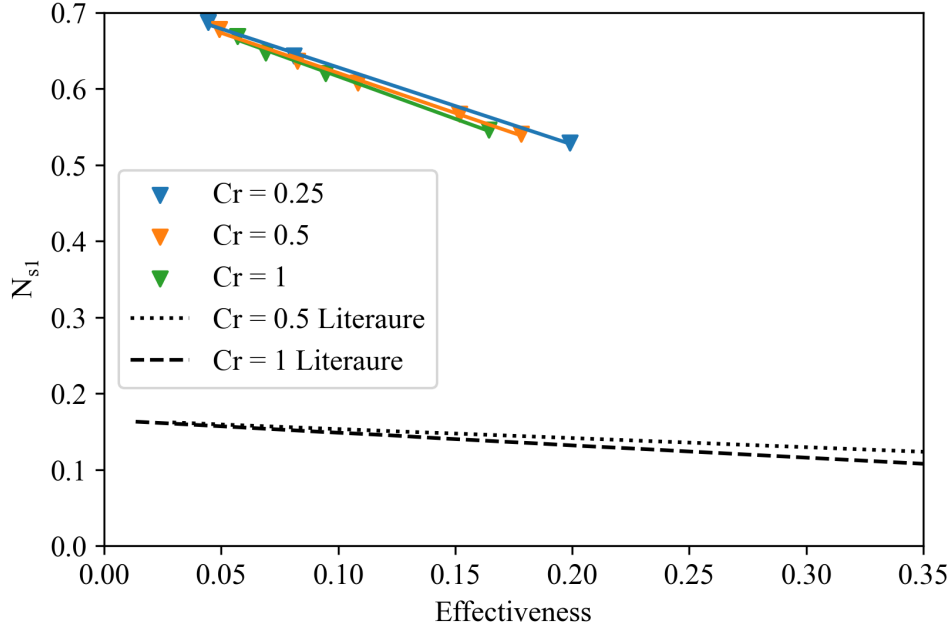


Figure 52: The entropy generation number for the circular geometry HX follows the correct trend in approaching zero as effectiveness increases though the values presented here are much higher than one instance found in literature.

in the system may account for the large differences in measured wattage and Nu between the hot and cold sides of the heat exchanger, as depicted in Figures 48 and 49.

The oval twisted HX experienced similarly large values for entropy generation number providing measured values as high as 190 - 355% greater than anticipated. Though these values are higher than Hesselgreaves examples, the entropy generation number for the oval twisted geometry is significantly less than than the N_{s1} for the circular HX. As shown in Figure 53 the entropy generation number is up to 24% lower than the circular geometry. Figures 52 and 53 were gathered at corresponding flow parameters indicating that the oval twisted geometry provides higher effectiveness and lower entropy generation than the circular counterpart.

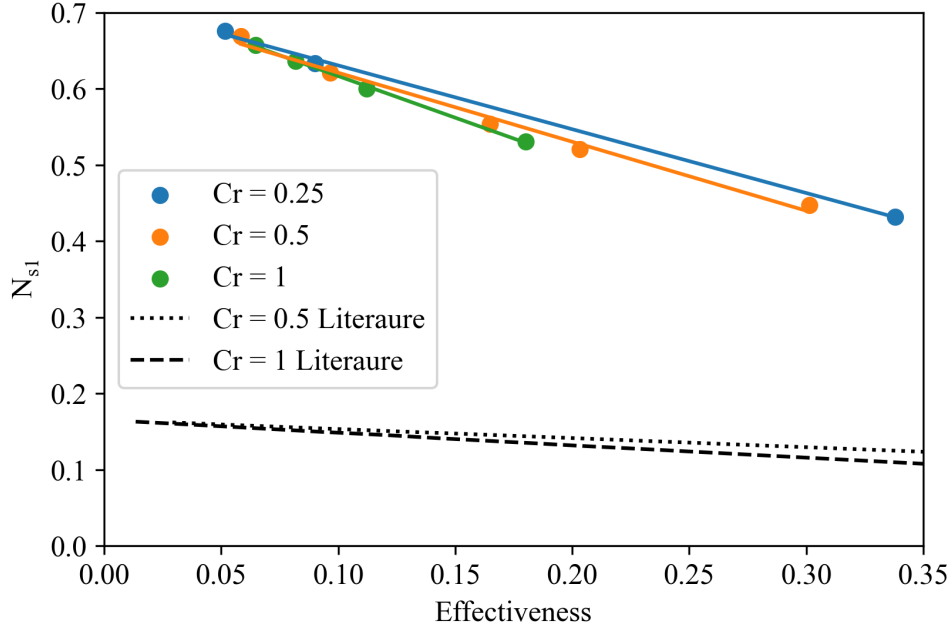


Figure 53: The entropy generation number for the oval twisted HX presents values approximately 24% lower than the circular HX.

4.6.4 Number of Transfer Units

The number of transfer units NTU provides insight in the HX ability to transfer heat and is often tied to surface area. A larger HX with the same overall heat transfer coefficient as another will have a larger NTU than a smaller HX. However if the HXs both have the same heat transfer surface area and flow parameters as shown in Eq. 8, any change in overall heat transfer coefficient will result in a proportional rise in NTU. In this study, the surface area of the circular and oval twisted design was maintained within 0.6%, the heat transfer surface area is 0.4143 m^2 for the circular design and 0.4115 m^2 for the oval twisted design. This results in simulation designs where the hydraulic diameters for the internal flow tubes in the circular design are different than the hydraulic diameters in the the oval twisted design. This design choice does bias other flow characteristics and parameters such as internal local Re number. However for heat transfer and entropy analysis, maintaining the heat transfer surface area between designs proves necessary.

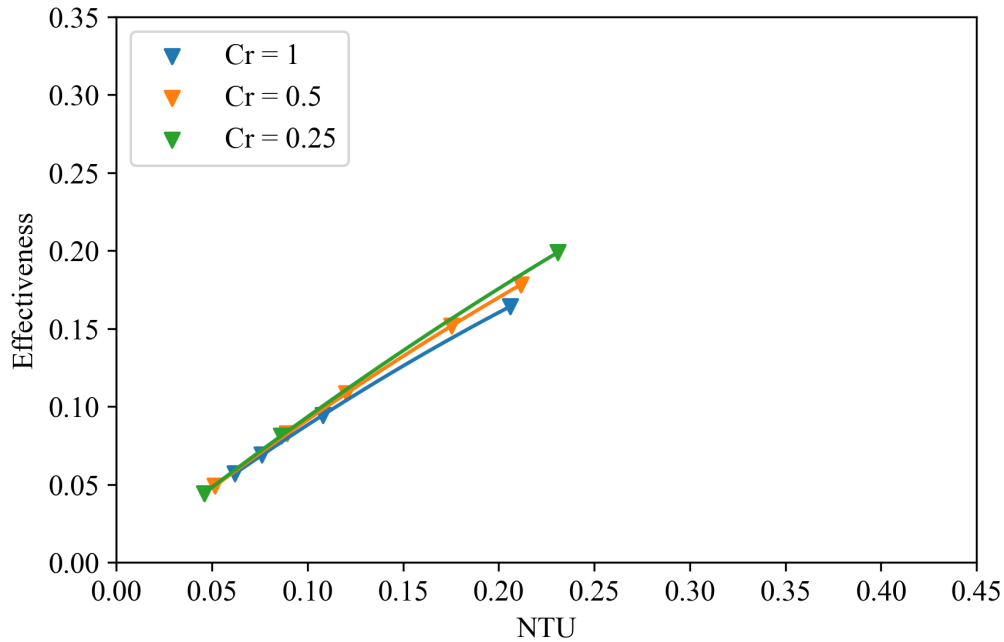


Figure 54: The effectiveness vs NTU trend follows the appropriate pattern, additionally the effectiveness and NTU for the circular HX are significantly lower than the values for the oval twisted design.

As shown in Figure 54, the circular geometry HX presents correct trends in effectiveness vs NTU. This same trend is found in Figure 55 and is intuitive. When Figures 54 and 55 are compared it is evident that the oval twisted geometry produces much higher values for both NTU and Effectiveness with increases up to 48% and 41% respectively.

4.6.5 Simulation and Experiment Comparison

A brief comparison was made between the CFD results and the experimental results. Though some values matched well between the CFD and experimental results not all parameters matched with satisfying results. Having high confidence in the experimental measurements it was deemed that insufficient work was conducted to ensure CFD accuracy. The CFD work fulfilled its crucial role in refining both the HX design and flow parameters. Further investigations and considerations must be made to accurize the CFD results. These plots, though largely inconclusive are presented in Appendix C.

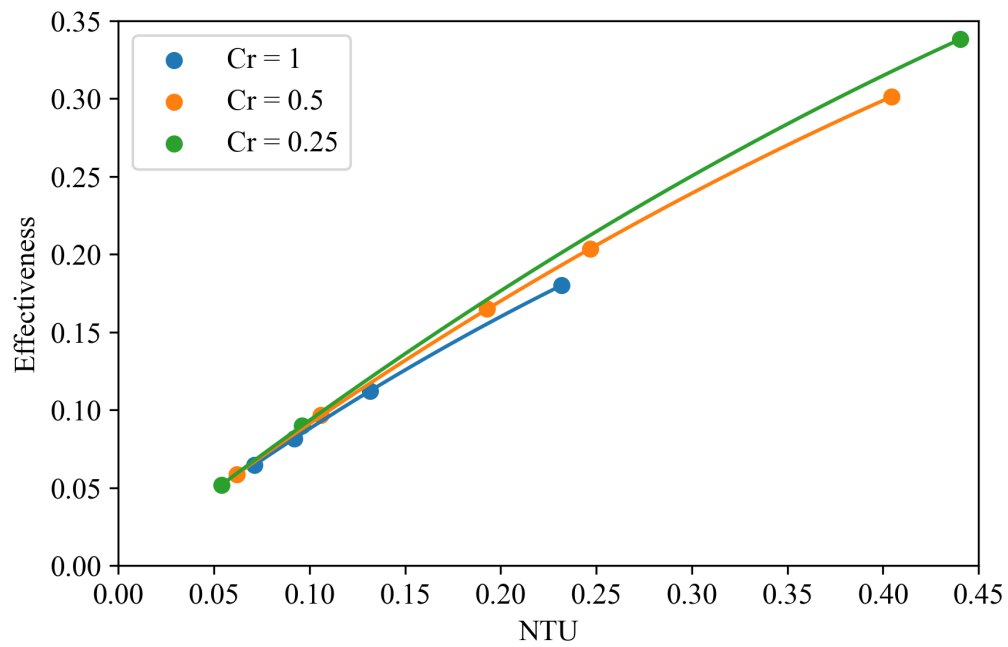


Figure 55: The increase in effectiveness for the oval twisted geometry shown here is 9 - 41% greater than circular counterpart. Further it also present NTU values 11 - 48% greater than circular design.

Chapter V: Conclusion and Future Work

Simulations were successfully used to define the flow parameters of the experiment. This stage included using simulations to refine the size, layout, and configuration of the two heat exchanger test sections. Through appropriate model selection and sensitivity study the flow rates and temperatures were defined to ensure that measurable temperature drops across the HXs would be obtained. The CFD work also played a critical role in refining the HX geometrical design. The facility was successfully designed and constructed to meet the experiment requirements. This included construction to various requirements including, the ability to operate at maximum and minimum temperatures of 80 and 20 °C respectively, monitor flowrate, record temperature, and monitor pressure. An uncertainty analysis was conducted and calculated that the uncertainty in wattage measurement is between 0.49% and 4.6% for the range of flow parameters. Similarly the uncertainty in Nu and heat transfer coefficient was calculated to be a minimum of 0.64% and a maximum of 5.6%. Though these values are quite low the facility does have inherent weaknesses, one such weakness that may be resolved in the future is the considerable noise in the low flow rate range below 0.38 *kg/s*. As a result the direct measurement of flow rate was not a viable option. Calibration curves were developed by taking manual readings at various flowrate settings. These curves were used to define flowrate motor settings for the duration of the tests. Though this method works it is not preferable, further electrical engineering work to mitigate signal noise or the acquisition of different flowmeters should be completed in the future.

The main purpose of the project was fulfilled, high fidelity experimental data for two cross flow plate type HXs was obtained. The first HX acted as a baseline measurement and consisted of a HX with circular cross section flow tubes. The second consisted of an identical HX with oval twisted flow tubes. The findings for heat transfer performance are best summarized in Figure 51 where the oval twisted heat exchanger in balanced flow conditions outperforms the circular counter parts in overall heat transfer coefficient, Nu, and

wattage. The performance increase in U , Nu , and q ranges between 1.1 and 1.25 times greater than unity indicating superior heat transfer. Similarly in imbalanced flow conditions improvements in wattage range between 0% - 19.7% while improvements in Nu range between 0% and 19.2%. All of these improvements occurred from Re numbers ranging from 1250 - 10,000 in the cold working fluid and from 3550 - 28,300 in the hot working fluid. The entropy generation was also considered and calculated and yielded entropy generation numbers N_{s1} between approximately 0.52 and 0.7 for the circular geometry and between approximately 0.4 and 0.68 for the oval twisted geometry. These calculations indicate a decrease in entropy generation number of up to 24% at high Re flowrates. This implies that the oval twisted geometry not only outperforms the circular design in heat transfer but that it also experiences reduced losses due to entropy generation. Lastly, the relationship between effectiveness and number of transfer units was investigated. The oval twisted design displays increases in effectiveness over the circular counterpart these increases between 9% and 41%, similar increases in NTU range from 11% - 48%.

Future Work

The facility constructed for these experiments proved easy to operate and was able to maintain considerably accurate HX inlet temperatures. There are however further controls that may be implemented to improve the fidelity of the data produced with the system. New flowmeters which have maximum flowrate reading ranges closer to the facility limitations would improve the ability to measure flowrate. Noise reduction filters should be investigated for the measurement of flowrate to improve accuracy. Computer controlled flow control valves should be used in strategic locations to regulate flowrates and temperatures. One area which would benefit highly from the use of a single computer controlled valve is the industrial cold water supply, this would allow the operator to control the secondary loop fluid temperature with greater accuracy.

A comparison between the numerical investigation and the experimental data was conducted though is only reported upon briefly. Though the CFD work played a key role in

design refinement and defining test parameters further work must be done to accurize the numerically generated data. Further works may completed concerning this design and aspects of this HX. Work may be conducted on pitch optimization for the oval twisted tubes. This may be further studied by investigating geometrical concerns for flow optimization where tube spacing, inlet layout, flow directions, and flow guide vanes are included. As with all heat transfer studies, further investigations may be made where flow parameter ranges are increased, this could include lower and higher Re , or the widening of inlet temperature ranges. Studies including fouling should also be considered to determine cost benefits for this design where manufacturing costs and heat transfer enhancements may then be compared to HX lifetime.

References

- [1] Piyush Sabharwall et al. Process Heat Exchanger Options for the Advanced High Temperature Reactor. Tech. rep. Idaho National Laboratory, 2011. url: <https://inldigitallibrary.inl.gov/sites/sti/sti/5144345.pdf>.
- [2] Yitung Chen Steven R. Sherman. HX Testing Requirements and Facility Needs for the NHI/NGNP Project. Tech. rep. Savannah River National Laboratory, Apr. 2008. url: <https://art.inl.gov/NGNP/INL%20Documents/Year%202008/HX%20Testing%20Requirements%20and%20Facility%20Needs%20for%20the%20NHI-NGNP%20Project.pdf>.
- [3] Luai M. Al-Hadhrami, Aftab Ahmad, and Abdullah Al-Qahtani. “Performance analysis of heat exchangers of an existing naphtha hydrotreating plant: A case study”. In: Applied Thermal Engineering 30.8 (2010), pp. 1029–1033. issn: 1359-4311. doi: <https://doi.org/10.1016/j.applthermaleng.2010.01.017>. url: <https://www.sciencedirect.com/science/article/pii/S135943111000030X>.
- [4] Alfa Laval. How Does a Plate Type Heat Exchanger Work. Apr. 2023. url: <https://www.alfalaval.my/products/heat-transfer/plate-heat-exchangers/gasketed-plate-and-frame-heat-exchangers/heat-exchanger/how-plate-heat-exchanger-work/>.
- [5] Shaukat Ali. “Pressure drop correlations for flow through regular helical coil tubes”. In: Fluid Dynamics Research 28.4 (Apr. 2001), pp. 295–310. doi: 10.1016/S0169-5983(00)00034-4. url: [https://doi.org/10.1016/S0169-5983\(00\)00034-4](https://doi.org/10.1016/S0169-5983(00)00034-4).
- [6] Scott Wahlquist et al. “Laminar Flow Heat Transfer in Helical Oval-Twisted Tube Heat Exchangers”. In: Frontiers in Heat and Mass Transfer (2021).
- [7] Jundika C. Kurnia, Benitta A. Chaedir, and Agus P. Sasmito. “Laminar convective heat transfer in helical tube with twisted tape insert”. In: International Journal of Heat

- and Mass Transfer 150 (2020), p. 119309. issn: 0017-9310. doi: <https://doi.org/10.1016/j.ijheatmasstransfer.2020.119309>. url: <https://www.sciencedirect.com/science/article/pii/S001793101935152X>.
- [8] Kim Leong Liaw, Jundika C. Kurnia, and Agus P. Sasmito. “Turbulent convective heat transfer in helical tube with twisted tape insert”. In: International Journal of Heat and Mass Transfer 169 (2021), p. 120918. issn: 0017-9310. doi: <https://doi.org/10.1016/j.ijheatmasstransfer.2021.120918>. url: <https://www.sciencedirect.com/science/article/pii/S0017931021000211>.
- [9] Jundika C. Kurnia, Agus P. Sasmito, and Arun S. Mujumdar. “Evaluation of the heat transfer performance of helical coils of non-circular tubes”. In: Journal of Zhejiang University-SCIENCE A 12.1 (Jan. 2011), pp. 63–70. issn: 1862-1775. doi: [10.1631/jzus.A1000296](https://doi.org/10.1631/jzus.A1000296). url: <https://doi.org/10.1631/jzus.A1000296>.
- [10] Y.M. Ferng, W.C. Lin, and C.C. Chieng. “Numerically investigated effects of different Dean number and pitch size on flow and heat transfer characteristics in a helically coil-tube heat exchanger”. In: Applied Thermal Engineering 36 (2012), pp. 378–385. issn: 1359-4311. doi: <https://doi.org/10.1016/j.applthermaleng.2011.10.052>. url: <https://www.sciencedirect.com/science/article/pii/S1359431111006041>.
- [11] Mohamed H. Mousa, Nenad Miljkovic, and Kashif Nawaz. “Review of heat transfer enhancement techniques for single phase flows”. In: Renewable and Sustainable Energy Reviews 137 (2021), p. 110566. issn: 1364-0321. doi: <https://doi.org/10.1016/rser.2020.110566>. url: <https://www.sciencedirect.com/science/article/pii/S1364032120308509>.
- [12] Jose L. Fernández and Robert Poulter. “Radial mass flow in electrohydrodynamically enhanced forced heat transfer in tubes”. In: International Journal of Heat and Mass Transfer 30.10 (1987), pp. 2125–2136. issn: 0017-9310. doi: <https://doi.org/10.1016/j.ijheatmasstransfer.1987.10.010>.

- 1016/0017-9310(87)90091-3. URL: <https://www.sciencedirect.com/science/article/pii/0017931087900913>.
- [13] Mohammad Goharkhah et al. “Convective heat transfer characteristics of magnetite nanofluid under the influence of constant and alternating magnetic field”. In: *Powder Technology* 274 (2015), pp. 258–267. issn: 0032-5910. doi: <https://doi.org/10.1016/j.powtec.2015.01.031>. url: <https://www.sciencedirect.com/science/article/pii/S0032591015000479>.
- [14] Habib Aminfar, Mousa Mohammadpourfard, and Yousef Narmani Kahnamouei. “A 3D numerical simulation of mixed convection of a magnetic nanofluid in the presence of non-uniform magnetic field in a vertical tube using two phase mixture model”. In: *Journal of Magnetism and Magnetic Materials* 323.15 (2011), pp. 1963–1972. issn: 0304-8853. doi: <https://doi.org/10.1016/j.jmmm.2011.02.039>. url: <https://www.sciencedirect.com/science/article/pii/S0304885311001491>.
- [15] Aliakbar Izadi et al. “MHD enhanced nanofluid mediated heat transfer in porous metal for CPU cooling”. In: *Applied Thermal Engineering* 168 (2020), p. 114843. issn: 1359-4311. doi: <https://doi.org/10.1016/j.applthermaleng.2019.114843>. url: <https://www.sciencedirect.com/science/article/pii/S1359431119333204>.
- [16] Tatsuo Nishimura and Shigeki Matsune. “Vortices and wall shear stresses in asymmetric and symmetric channels with sinusoidal wavy walls for pulsatile flow at low Reynolds numbers”. In: *International Journal of Heat and Fluid Flow* 19.6 (1998), pp. 583–593. issn: 0142-727X. doi: [https://doi.org/10.1016/S0142-727X\(98\)10005-X](https://doi.org/10.1016/S0142-727X(98)10005-X). url: <https://www.sciencedirect.com/science/article/pii/S0142727X9810005X>.
- [17] Hamed Khosravi-Bizhaem, Abbas Abbassi, and Amir Zivari Ravan. “Heat transfer enhancement and pressure drop by pulsating flow through helically coiled tube: An experimental study”. In: *Applied Thermal Engineering* 160 (2019), p. 114012. ISSN:

1359-4311. doi: <https://doi.org/10.1016/j.applthermaleng.2019.114012>. url: <https://www.sciencedirect.com/science/article/pii/S1359431119325001>.

- [18] D.X. Jin, Y.P. Lee, and D.-Y. Lee. “Effects of the pulsating flow agitation on the heat transfer in a triangular grooved channel”. In: *International Journal of Heat and Mass Transfer* 50.15 (2007), pp. 3062–3071. issn: 0017-9310. doi: <https://doi.org/10.1016/j.ijheatmasstransfer.2006.12.001>. url: <https://www.sciencedirect.com/science/article/pii/S0017931007000038>.
- [19] Mohamed S. El-Genk and Timothy M. Schriener. “A Review and Correlations for Convection Heat Transfer and Pressure Losses in Toroidal and Helically Coiled Tubes”. In: *Heat Transfer Engineering* 38.5 (2017), pp. 447–474. doi: 10.1080/01457632.2016.1194693. eprint: <https://doi.org/10.1080/01457632.2016.1194693>. url: <https://doi.org/10.1080/01457632.2016.1194693>.
- [20] Aiwu Fan et al. “A numerical study on thermo-hydraulic characteristics of turbulent flow in a circular tube fitted with conical strip inserts”. In: *Applied Thermal Engineering* 31.14 (2011), pp. 2819–2828. issn: 1359-4311. url: <https://www.sciencedirect.com/science/article/pii/S1359431111002596>.
- [21] Jian Guo et al. “A numerical study on heat transfer and friction factor characteristics of laminar flow in a circular tube fitted with center-cleared twisted tape”. In: *International Journal of Thermal Sciences* 50.7 (2011), pp. 1263–1270. issn: 1290-0729. doi: <https://doi.org/10.1016/j.ijthermalsci.2011.02.010>. url: <https://www.sciencedirect.com/science/article/pii/S1290072911000512>.
- [22] P. Promvong and S. Eiamsa-ard. “Heat transfer behaviors in a tube with combined conical-ring and twisted-tape insert”. In: *International Communications in Heat and Mass Transfer* 34.7 (2007), pp. 849–859. issn: 0735-1933. url: <https://www.sciencedirect.com/science/article/pii/S0735193307000723>.

- [23] S. Suresh, K.P. Venkitaraj, and P. Selvakumar. “Comparative study on thermal performance of helical screw tape inserts in laminar flow using Al₂O₃/water and CuO/water nanofluids”. In: *Superlattices and Microstructures* 49.6 (2011), pp. 608–622. issn: 0749-6036. doi: <https://doi.org/10.1016/j.spmi.2011.03.012>. url: <https://www.sciencedirect.com/science/article/pii/S0749603611000486>.
- [24] Mohamed Moustafa Abdelhalim Ahmed Eid et al. “Passive heat transfer augmentation in conduits by surface modification: a review”. In: *Journal of Thermal Analysis and Calorimetry* 147.24 (Dec. 2022), pp. 14601–14620. issn: 1588-2926. doi: [10.1007/s10973-022-11642-8](https://doi.org/10.1007/s10973-022-11642-8). url: <https://doi.org/10.1007/s10973-022-11642-8>.
- [25] Ali K . Abdul Razzaq and Khudheyer Mushatet. “A Review Study for a Twisted Tube Heat Exchanger”. In: *Journal of Nanofluids* 12 (Dec. 2022), pp. 299–317. doi: [10.1166/jon.2023.1926](https://doi.org/10.1166/jon.2023.1926).
- [26] Xiang-hui Tan et al. “3D numerical simulation on the shell side heat transfer and pressure drop performances of twisted oval tube heat exchanger”. In: *International Journal of Heat and Mass Transfer* 65 (2013), pp. 244–253. issn: 0017-9310. doi: <https://doi.org/10.1016/j.ijheatmasstransfer.2013.06.011>. url: <https://www.sciencedirect.com/science/article/pii/S001793101300478X>.
- [27] Junlin Cheng, Zuoqin Qian, and Qiang Wang. “Analysis of heat transfer and flow resistance of twisted oval tube in low Reynolds number flow”. In: *International Journal of Heat and Mass Transfer* 109 (2017), pp. 761–777. issn: 0017-9310. doi: <https://doi.org/10.1016/j.ijheatmasstransfer.2017.02.061>. url: <https://www.sciencedirect.com/science/article/pii/S0017931016331441>.
- [28] Xiang-hui Tan et al. “Experimental and numerical study of convective heat transfer and fluid flow in twisted oval tubes”. English. In: *International Journal of Heat and Mass Transfer* 55.17-18 (2012), pp. 4701–4710. doi: [10.1016/j.ijheatmasstransfer.2012.04.030](https://doi.org/10.1016/j.ijheatmasstransfer.2012.04.030).

- [29] Li Zhang, Sheng Yang, and Hong Xu. “Experimental study on condensation heat transfer characteristics of steam on horizontal twisted elliptical tubes”. In: *Applied Energy* 97 (2012). *Energy Solutions for a Sustainable World - Proceedings of the Third International Conference on Applied Energy*, May 16-18, 2011 - Perugia, Italy, pp. 881–887. issn: 0306-2619. doi: <https://doi.org/10.1016/j.apenergy.2011.11.085>. url: <https://www.sciencedirect.com/science/article/pii/S0306261911007914>.
- [30] Chao Luo et al. “Heat Transfer Enhancement in a Novel Annular Tube with Outer Straight and Inner Twisted Oval Tubes”. In: *Symmetry* 12.8 (2020). issn: 2073-8994. doi: 10.3390/sym12081213. url: <https://www.mdpi.com/2073-8994/12/8/1213>.
- [31] Amin Ebrahimi and Ehsan Roohi. “Numerical Study of Flow Patterns and Heat Transfer in Mini Twisted Oval Tubes”. In: *International Journal of Modern Physics C* 26 (Dec. 2015), p. 1550140. doi: 10.1142/S0129183115501405.
- [32] An-Ning Guo and Liangbi Wang. “Parametrization of secondary flow intensity for laminar forced convection in twisted elliptical tube and derivation of loss coefficient and Nusselt number correlations by numerical analysis”. In: *International Journal of Thermal Sciences* 155 (Sept. 2020), p. 106425. doi: 10.1016/j.ijthermalsci.2020.106425.
- [33] P. Promthaisong, W. Jedsadaratanachai, and S. Eiamsa-ard. “3D Numerical study on the flow topology and heat transfer characteristics of turbulent forced convection in spirally corrugated tube”. In: *Numerical Heat Transfer, Part A: Applications* 69.6 (2016), pp. 607–629. doi: 10.1080/10407782.2015.1069670. eprint: <https://doi.org/10.1080/10407782.2015.1069670>. url: <https://doi.org/10.1080/10407782.2015.1069670>.
- [34] Xiuzhen Li et al. “Thermal-Hydraulic Characteristics of Twisted Elliptical Tube Bundle in Staggered Arrangement”. In: *Journal of Thermal Science* 30.6 (Nov. 2021),

pp. 1925–1937. issn: 1993-033X. doi: 10.1007/s11630-021-1450-3. url: <https://doi.org/10.1007/s11630-021-1450-3>.

- [35] Huaduo Gu et al. “Influence of alternating V-rows tube layout on thermal-hydraulic characteristics of twisted elliptical tube heat exchangers”. In: *International Journal of Heat and Mass Transfer* 159 (2020), p. 120070. issn: 0017-9310. doi: <https://doi.org/10.1016/j.ijheatmasstransfer.2020.120070>. url: <https://www.sciencedirect.com/science/article/pii/S0017931020330064>.
- [36] Huaduo Gu et al. “Performance investigation on twisted elliptical tube heat exchangers with coupling-vortex square tube layout”. In: *International Journal of Heat and Mass Transfer* 151 (2020), p. 119473. issn: 0017-9310. doi: <https://doi.org/10.1016/j.ijheatmasstransfer.2020.119473>. url: <https://www.sciencedirect.com/science/article/pii/S001793102030065X>.
- [37] Shijie Liu et al. “Experimental investigation on shell-side performance of a novel shell and tube oil cooler with twisted oval tubes”. In: *International Journal of Thermal Sciences* 152 (2020), p. 106290. issn: 1290-0729. doi: <https://doi.org/10.1016/j.ijthermalsci.2020.106290>. url: <https://www.sciencedirect.com/science/article/pii/S1290072919317089>.
- [38] Frank P. Incropera et al. *Fundamentals of Heat and Mass Transfer*. Frank P. Incropera ... [et al.]. 6th ed. John Wiley and Sons Inc., 2006. isbn: 978-0-471-45728-2.
- [39] John E. Hesselgreaves, Richard Law, and David A. Reay. “Chapter 3 - The Heat Exchanger as Part of a System: Exergetic (Second Law) Analysis”. In: *Compact Heat Exchangers (Second Edition)*. Ed. by John E. Hesselgreaves, Richard Law, and David A. Reay. Second Edition. Butterworth-Heinemann, 2017, pp. 91–127. isbn: 978-0-08-100305-3. doi: <https://doi.org/10.1016/B978-0-08-100305-3.00003-3>. url: <https://www.sciencedirect.com/science/article/pii/B9780081003053000033>.

- [40] Jundika C. Kurnia et al. “Improved design for heat transfer performance of a novel phase change material (PCM) thermal energy storage (TES)”. In: *Applied Thermal Engineering* 50.1 (2013), pp. 896–907. issn: 1359-4311. doi: <https://doi.org/10.1016/j.applthermaleng.2012.08.015>. url: <https://www.sciencedirect.com/science/article/pii/S1359431112005376>.
- [41] “Procedure for Estimation and Reporting of Uncertainty Due to Discretization in CFD Applications”. In: *Journal of Fluids Engineering* 130.7 (July 2008). 078001. issn: 0098-2202. doi: 10.1115/1.2960953. eprint: https://asmedigitalcollection.asme.org/fluidsengineering/article-pdf/130/7/078001/5491455/078001_1.pdf. url: <https://doi.org/10.1115/1.2960953>.
- [42] Tsan-Hsing Shih et al. “A new k-epsilon eddy viscosity model for high reynolds number turbulent flows”. In: *Computers and Fluids* 24.3 (1995), pp. 227–238. issn: 0045-7930. doi: [https://doi.org/10.1016/0045-7930\(94\)00032-T](https://doi.org/10.1016/0045-7930(94)00032-T). url: <https://www.sciencedirect.com/science/article/pii/004579309400032T>.
- [43] F. R. Menter. “Two-equation eddy-viscosity turbulence models for engineering applications”. In: *AIAA Journal* 32.8 (1994), pp. 1598–1605. doi: 10.2514/3.12149. eprint: <https://doi.org/10.2514/3.12149>. url: <https://doi.org/10.2514/3.12149>.
- [44] J. Rotta. “Statistische Theorie nichthomogener Turbulenz”. In: *Zeitschrift für Physik* 129.6 (Nov. 1951), pp. 547–572. issn: 0044-3328. doi: 10.1007/BF01330059. url: <https://doi.org/10.1007/BF01330059>.
- [45] National Instruments. Ni-9214 Specifications. Apr. 2023. url: <https://www.ni.com/docs/en-US/bundle/ni-9214-specs/page/specifications.html>.
- [46] National Instruments. Ni-9207 Specifications. Apr. 2023. url: <https://www.ni.com/docs/en-US/bundle/ni-9207-specs/page/specs.html>.

Appendix A: Mass Balance Data

Table 6: Mass balance values for Volume 1 and Volume 2 with total inlet flow rates of 0.03149 and 0.2519 kg/s respectively for the circular cross-section HX.

Volume 1					Volume 2				
#	Inlet (kg/s)	Outlet (kg/s)	% of Total	Mass Balance	#	Inlet (kg/s)	Outlet (kg/s)	% of Total	Mass Balance
1	0.00189	0.00189	6.0%	0.12%	17	0.03130	0.03117	12.4%	0.42%
2	0.00189	0.00189	6.0%	0.11%	18	0.02860	0.02866	11.4%	0.21%
3	0.00189	0.00187	6.0%	1.34%	19	0.04038	0.04034	16.0%	0.11%
4	0.00186	0.00187	5.9%	0.62%	20	0.02586	0.02577	10.3%	0.34%
5	0.00192	0.00193	6.1%	0.66%	21	0.02508	0.02503	10.0%	0.17%
6	0.00205	0.00205	6.5%	0.25%	22	0.04063	0.04060	16.1%	0.08%
7	0.00218	0.00218	6.9%	0.01%	23	0.02867	0.02862	11.4%	0.17%
8	0.00197	0.00197	6.3%	0.05%	24	0.03061	0.03052	12.2%	0.28%
9	0.00201	0.00202	6.4%	0.31%					
10	0.00217	0.00216	6.9%	0.29%					
11	0.00204	0.00206	6.5%	0.54%					
12	0.00191	0.00192	6.1%	0.43%					
13	0.00187	0.00187	5.9%	0.22%					
14	0.00185	0.00186	5.9%	0.70%					
15	0.00193	0.00192	6.1%	0.35%					
16	0.00188	0.00188	6.0%	0.05%					

Table 7: Mass balance values for Volume 1 and Volume 2 with total inlet flow rates of 0.2519 and 0.03149 kg/s respectively for the oval twisted HX.

Volume 1					Volume 2				
#	Inlet (kg/s)	Outlet (kg/s)	% of Total	Mass Balance	#	Inlet (kg/s)	Outlet (kg/s)	% of Total	Mass Balance
1	0.01528	0.01511	6.1%	1.05%	17	0.00393	0.00389	12.5%	1.03%
2	0.01585	0.01585	6.3%	0.00%	18	0.00393	0.00391	12.5%	0.53%
3	0.01556	0.01562	6.2%	0.37%	19	0.00402	0.00405	12.8%	0.77%
4	0.01537	0.01539	6.1%	0.15%	20	0.00382	0.00381	12.1%	0.19%
5	0.01523	0.01532	6.0%	0.61%	21	0.00379	0.00382	12.0%	0.57%
6	0.01592	0.01588	6.3%	0.27%	22	0.00407	0.00407	12.9%	0.06%
7	0.01669	0.01688	6.6%	1.14%	23	0.00390	0.00386	12.4%	0.81%
8	0.01568	0.01561	6.2%	0.48%	24	0.00383	0.00379	12.1%	0.81%
9	0.01514	0.01554	6.0%	2.64%					
10	0.01666	0.01674	6.6%	0.50%					
11	0.01588	0.01577	6.3%	0.69%					
12	0.01569	0.01552	6.2%	1.08%					
13	0.01551	0.01556	6.2%	0.34%					
14	0.01561	0.01546	6.2%	0.94%					
15	0.01570	0.01556	6.2%	0.87%					
16	0.01431	0.01424	5.7%	0.45%					

Table 8: Mass balance values for Volume 1 and Volume 2 with total inlet flow rates of 0.03149 and 0.2519 kg/s respectively for the oval cross-section HX..

Volume 1					Volume 2				
#	Inlet (kg/s)	Outlet (kg/s)	% of Total	Mass Balance	#	Inlet (kg/s)	Outlet (kg/s)	% of Total	Mass Balance
1	0.00194	0.00193	6.2%	0.55%	17	0.03121	0.03109	12.4%	0.41%
2	0.00196	0.00196	6.2%	0.00%	18	0.03091	0.03070	12.3%	0.67%
3	0.00194	0.00194	6.1%	0.18%	19	0.03369	0.03339	13.4%	0.89%
4	0.00193	0.00193	6.1%	0.03%	20	0.03002	0.02993	11.9%	0.28%
5	0.00193	0.00193	6.1%	0.25%	21	0.03019	0.03024	12.0%	0.16%
6	0.00198	0.00198	6.3%	0.01%	22	0.03368	0.03375	13.4%	0.22%
7	0.00201	0.00201	6.4%	0.01%	23	0.03067	0.03069	12.2%	0.07%
8	0.00198	0.00198	6.3%	0.30%	24	0.03125	0.03113	12.4%	0.39%
9	0.00194	0.00195	6.1%	0.90%					
10	0.00201	0.00201	6.4%	0.10%					
11	0.00198	0.00192	6.3%	3.03%					
12	0.00193	0.00192	6.1%	0.26%					
13	0.00192	0.00192	6.1%	0.13%					
14	0.00193	0.00191	6.1%	0.92%					
15	0.00191	0.00190	6.1%	0.41%					
16	0.00190	0.00190	6.0%	0.25%					

Appendix B: Flowrate Approximation Code

```
1 '''
2 IHX test facility flowrate approximation code
3
4 Written by: Kyle Schroeder
5 April 2023
6
7 This code takes the operators manual calibration measurements at the low
   and high operating temperatures and
8 conducts linear interpolation to approxiamte the VFD Hz setting for a
   desired fluid temperature and flowrate setting.
9 The operator must input new calibration data in the section idicated below
   titled "User Inputs".
10
11 Upon operation of the code the user must select the desired loop, input
   temperature, desired flowrate, and
12 select 'ok'. An updated plot will appear indicating the operating point
   parameters based on the users
13 selections.
14 '''
15
16 import numpy as np
17 from matplotlib import use as use_agg
18 from matplotlib.backends.backend_tkagg import FigureCanvasTkAgg
19 import matplotlib.pyplot as plt
20 import PySimpleGUI as sg
21 plt.rcParams['font.family']='Times New Roman'
22
23 ##### User Inputs #####
24 op_temp1 = 20 #
   this is the temperature of the loop when the measurements below were
```

```

    recorded
25 Hz = [3,7,15,30,60] #
    These are the discrete Hz which the flowrates were measured at
26 Primary = [0.5536587,1.50222,3.440909,7.34146,15.5225] #
    The reseptive flowrates for the primary loop
27 Secondary = [0.4219512,1.257777,3.104545,6.28536,11.03] #
    The reseptive flowrates for the secondary loop
28
29 op_temp2 = 80 #
    this is the temperature of the loop when the measurements below were
    recorded
30 Hz_high = [3,7,60] #
    These are the discrete Hz which the flowrates were measured at
31 Primary_high = [0.595238095, 1.514285714, 13.00952381] #
    The reseptive flowrates for the primary loop
32 Secondary_high = [0.547619048, 1.452380952, 10.25238095] #
    The reseptive flowrates for the secondary loop
33
34 ##### Storage Arrays #####
35 Hz_ = np.linspace(min(Hz),max(Hz),100)
36 new_fit = np.zeros(len(Hz_))
37
38 ##### Curve Fits #####
39 Primary_fit = np.poly1d(np.polyfit(Hz,Primary,2))
40 Secondary_fit = np.poly1d(np.polyfit(Hz,Secondary,2))
41
42 Primary_fit_high = np.poly1d(np.polyfit(Hz_high,Primary_high,2))
43 Secondary_fit_high = np.poly1d(np.polyfit(Hz_high,Secondary_high,2))
44
45 ##### Functions #####
46 def pack_figure(graph, figure):
47     canvas = FigureCanvasTkAgg(figure, graph.Widget)
48     plot_widget = canvas.get_tk_widget()

```

```

49     plot_widget.pack(side='top', fill='both', expand=1)
50     return plot_widget
51
52 def plot_figure(a,b):                                     #
    Function for updating the plot in the GUI
53     plt.rcParams['font.family']='Times New Roman'
54     fig = plt.figure(1)                                # Active an existing figure
55     ax = plt.gca()
56     ax.cla()
57     plt.scatter(Hz,Primary,label='Primary {} \u2103'.format(op_temp1))
58     plt.scatter(Hz_high,Primary_high,label = 'Primary {} \u2103'.format(
op_temp2),color = '#1f77b4',marker = 'v')
59     plt.scatter(Hz,Secondary,label='Secondary {} \u2103'.format(op_temp1))
60     plt.scatter(Hz_high,Secondary_high,label = 'Secondary {} \u2103'.
format(op_temp2),color = '#ff7f0e',marker = 'v')
61     plt.plot(Hz_,Primary_fit(Hz_))
62     plt.plot(Hz_,Secondary_fit(Hz_))
63     plt.plot(Hz_,Primary_fit_high(Hz_),color = '#1f77b4')
64     plt.plot(Hz_,Secondary_fit_high(Hz_),color = '#ff7f0e')
65     plt.plot(Hz_,new_fit,color = 'red', linestyle = 'dotted')
66     plt.scatter(a,b,label = 'Setting',color = 'red')
67     plt.plot(array1,array2, color = 'red', linestyle = 'dotted')
68     plt.plot(array3,array4, color = 'red', linestyle = 'dotted')
69     plt.xlabel('VFD Pump Setting (Hz)')
70     plt.ylabel('Flowrate (GPM)')
71     plt.xlim(0,1.1*max(Hz))
72     if max(Primary)>max(Secondary):
73         plt.ylim(0,1.1*max(Primary))
74     else:
75         plt.ylim(0,1.1*max(Secondary))
76     plt.legend()
77     plt.savefig('example_fig.png',dpi=300)
78     fig.canvas.draw()                                # Render figure into canvas

```

```

79
80 ##### User Interface #####
81
82 use_agg('TkAgg')
83 input1 = 0
84 output1 = 0
85
86 layout1 = [ [sg.Text('Select Loop of Interest:')] ,
87             [sg.Checkbox('Primary Loop',key='p1')] ,
88             [sg.Checkbox('Secondary Loop',key='s1')] ,
89             [sg.Text('Enter Fluid Temperature:'),sg.InputText(key='TEMP')
90             ],
91             [sg.Text('Enter Desired GPM:'), sg.InputText(key='INPUT')],
92             [sg.Text('GPM:'),sg.Text(key='Hz_OUT'),sg.Text('Hz:'),sg.Text(
93             ' ',expand_x=True,key='OUT')],
94             [sg.Button('Ok'), sg.Button('Cancel')],
95             [sg.Graph((640, 480), (0, 0), (640, 480),key='Graph')]]
96
97 window = sg.Window('Hz Calculator',layout1,size=(715,500),finalize=True)
98         # initializes GUI window
99
100 graph1 = window['Graph']
101 plt.ioff()
102 fig1 = plt.figure(1)
103 ax1 = plt.subplot(111)
104 pack_figure(graph1, fig1)
105
106 while True:
107     # window logic for manipulating user inputs
108     event, values = window.read()
109     if event == sg.WIN_CLOSED or event == 'Cancel': # if user closes
110     window or clicks cancel
111         break

```

```

107     if event == 'Ok':
108         temp_ratio = (float(values['TEMP'])-op_temp1)/(op_temp2-op_temp1)
109         if values['p1']==True and values['s1']==True:
110             window['s1'].update(value=False)
111             window['p1'].update(value=False)
112             window['OUT'].update(value = 'Please select only one Loop ')
113         elif values['p1']==True:
114             for i in range(len(Hz_)):
115                 # Linear interpoation using the users temp
116                 new_fit[i] = temp_ratio*(Primary_fit(Hz_[i])-
Primary_fit_high(Hz_[i]))+Primary_fit_high(Hz_[i])
117                 new_fit_poly = np.poly1d(np.polyfit(new_fit,Hz_,2))
118                 Hz_1 = new_fit_poly(float(values['INPUT']))
119                 window['OUT'].update(value = Hz_1)
120         elif values['s1']==True:
121             for i in range(len(Hz_)):
122                 new_fit[i] = temp_ratio*(Secondary_fit(Hz_[i])-
Secondary_fit_high(Hz_[i]))+Secondary_fit_high(Hz_[i])
123                 new_fit_poly = np.poly1d(np.polyfit(new_fit,Hz_,2))
124                 Hz_1 = new_fit_poly(float(values['INPUT']))
125                 window['OUT'].update(value = Hz_1)
126
127
128         output1 = float(values['INPUT'])
129
130         array1 = [0,Hz_1]
131         array2 = [output1,output1]
132         array3 = [Hz_1,Hz_1]
133         array4 = [0,output1]
134
135         window['Hz_OUT'].update(value = values['INPUT'])
136         plot_figure(Hz_1,output1)
137
138 window.close()

```

Appendix C: Simulation and Experiment Comparison Plots

Imbalanced Flow

The CFD data and experiment data do not match with successful confidence as shown in Figures 56 - 59. In all cases the CFD data over anticipates the improvement in heat transfer performance for imbalanced flow conditions. Though some of the trends set forth in the experiment do match the CFD approximations, further inaccuracies are present in the CFD work. This is likely due to losses and or flow conditions which are accounted for inadequately in the CFD simulations. Further work should be conducted ensuring model selection, mesh sizing, and physics parameters are sufficiently refined to capture the real world flow phenomena.

Balanced Flow

The CFD data and experiment data do not match with successful confidence as shown in Figures 60 - 63. In all cases the CFD data over anticipates the improvement in heat transfer performance for balanced flow conditions. Though some of the trends set forth in the experiment do match the CFD approximations, further inaccuracies are present in the CFD work. This is likely due to losses and or flow conditions which are unaccounted for in the CFD simulations. Further work should be conducted ensuring model selection, mesh sizing, and physics parameters are sufficiently refined to capture the real world flow phenomena.

Entropy

The CFD data and experiment data do not match with successful confidence as shown in Figures 64 and 65. In all cases the CFD data under predicted the losses due to entropy in the HX. This is likely due to losses and or flow conditions which are unaccounted for in the CFD simulations. Further work should be conducted ensuring model selection, mesh sizing,

and physics parameters are sufficiently refined to capture the real world flow phenomena.

Number of Transfer Units

The CFD data and experimental data match with successful confidence as shown in Figures 66 and 67. This indicates good agreement in the trend of NTU vs Effectiveness for both the CFD and experimental work. It should be noted though that the CFD simulations over predicted the effectiveness NTU trends for the circular geometry and under predicted the effectiveness NTU trends for the oval twisted geometry. This shows that the oval twisted HX produces much higher values for effectiveness and NTU than anticipated.

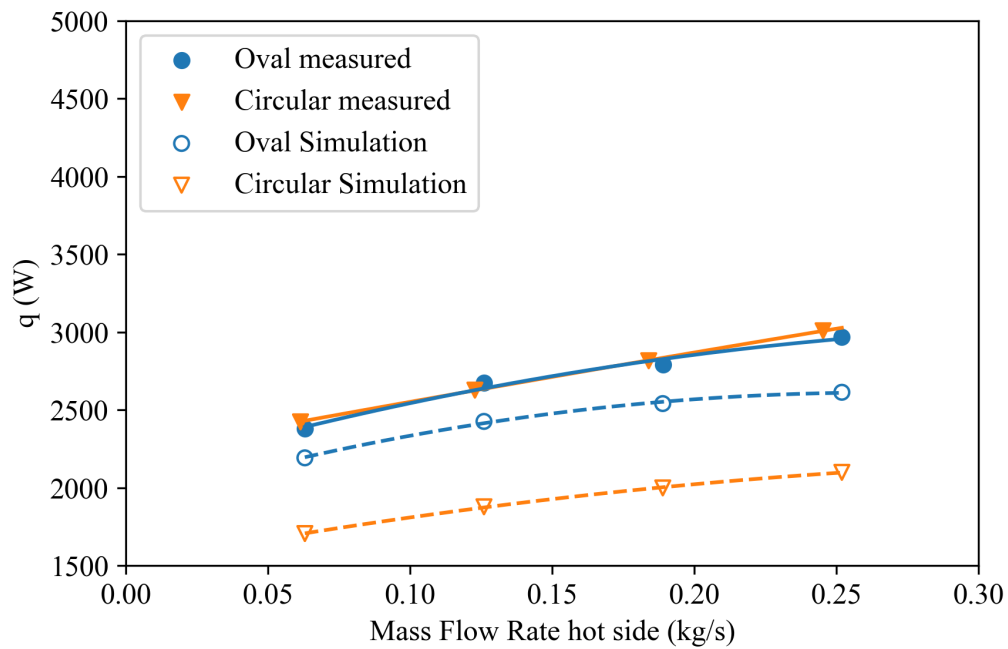


Figure 56: The cold side of the HX is fixed at 0.03149 kg/s while the hot side is swept. The predicted wattage and increased performance assumed in the simulation does not match the measured values.

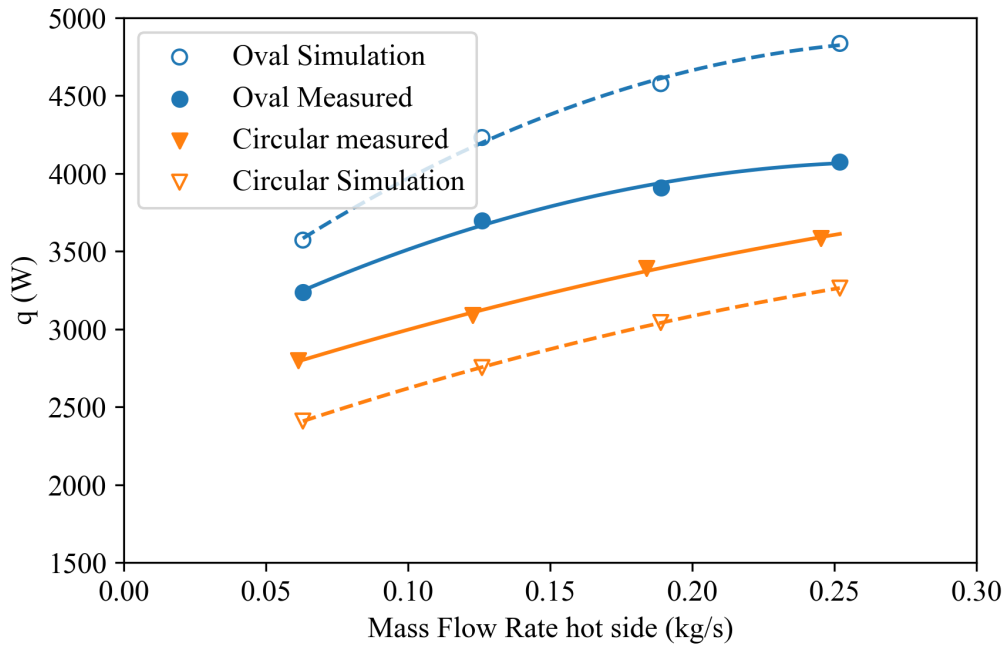


Figure 57: The cold side of the HX is fixed at 0.252 kg/s while the hot side is swept across the flow regime. The predicted wattage and increased performance assumed in the simulation does not match the measured values, however there is still marked performance increase for the oval twisted type HX.

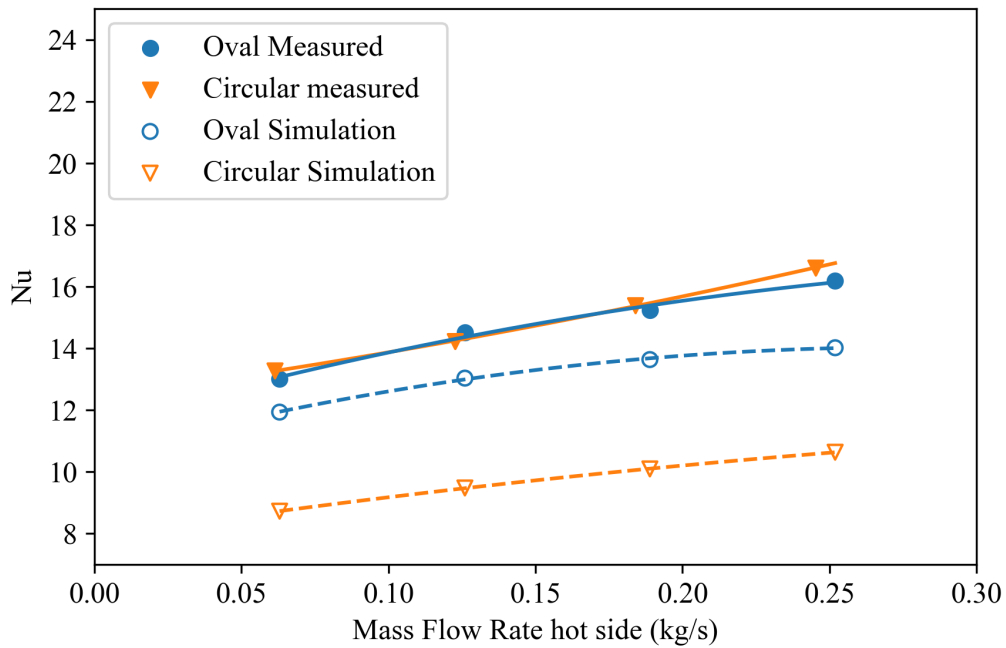


Figure 58: The cold side of the HX is fixed at 0.0315 kg/s while the hot side is swept. Between HXs the experiment shows no change in Nu given these flow conditions.

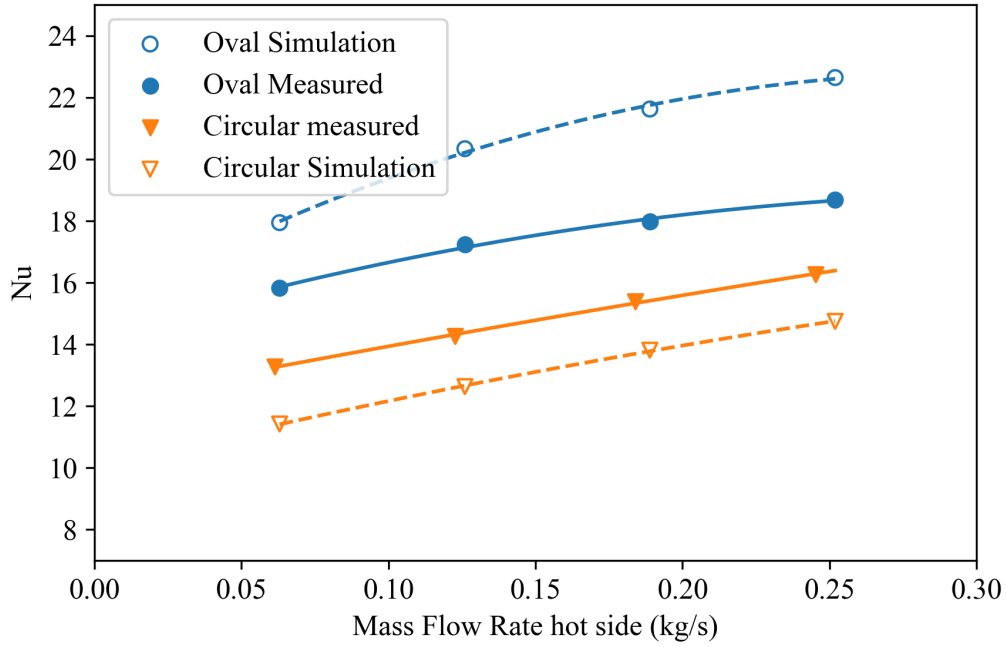
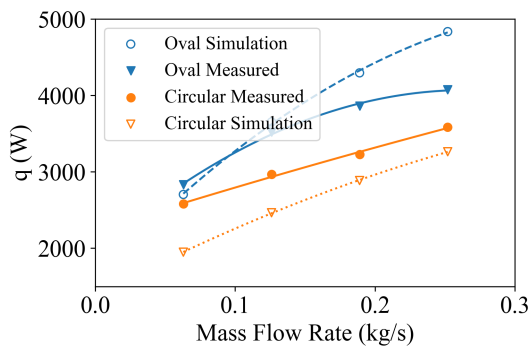
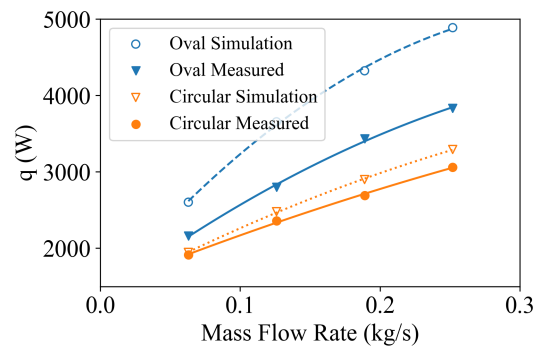


Figure 59: The cold side of the HX is fixed at 0.252 kg/s while the hot side is swept. Though the simulation does not match the measured values there is still marked improvement in Nu for the oval twisted type HX.

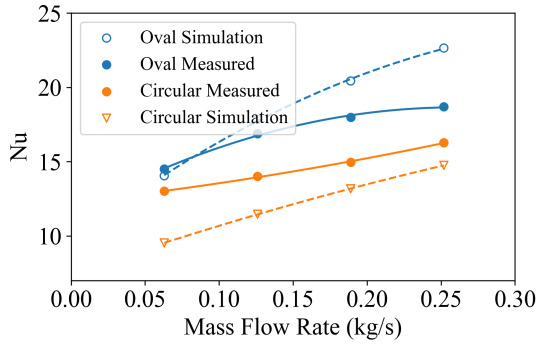


(a) The cold side wattage for both circular and oval twisted geometries.

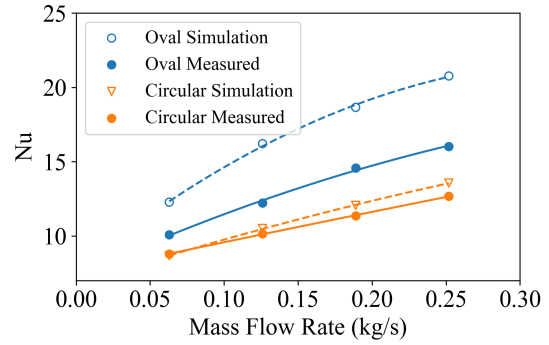


(b) The hot side wattage for both circular and oval twisted geometries.

Figure 60: The difference in measured wattages for the hot and cold side of the HX is apparent in the experiment data while not present in the simulation. Further work must be performed to capture this phenomena in the CFD simulations.



(a) The cold side Nu for both circular and oval twisted geometries.



(b) The hot side Nu for both circular and oval twisted geometries.

Figure 61: The difference in measured Nu for the hot and cold side of the HX is apparent in the experiment data while not present in the simulation. Further work must be performed to capture this phenomena in the CFD simulations.

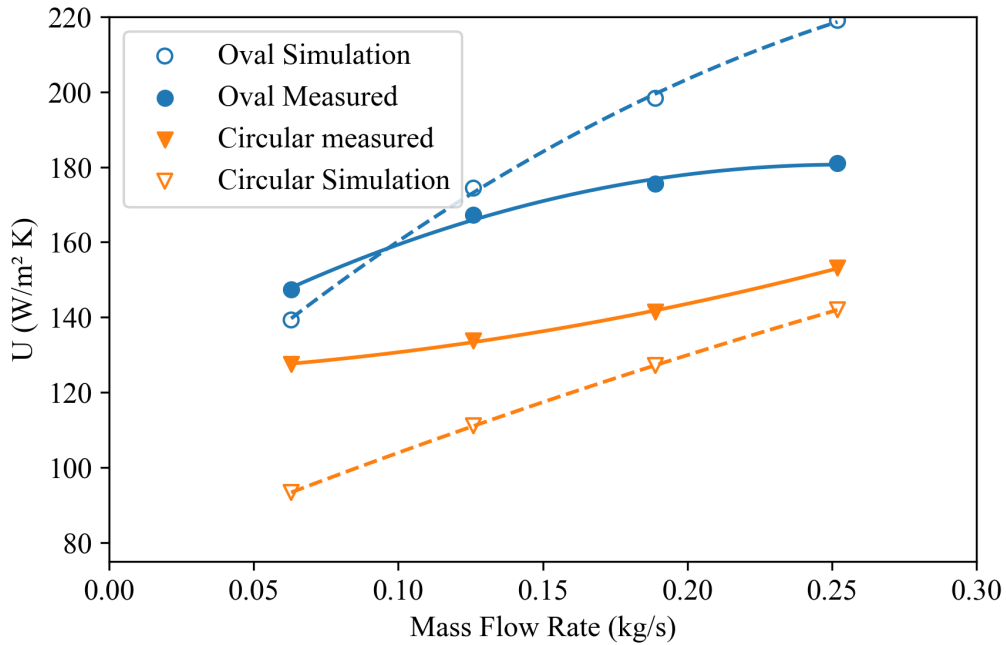


Figure 62: The values obtained for overall heat transfer coefficient in the experiment and simulation do not match with high confidence. The trend in heat transfer coefficient between the data sets does not appear to match in characteristic shape indicating that real-life losses that occur in the experiment are not accounted for in the simulation.

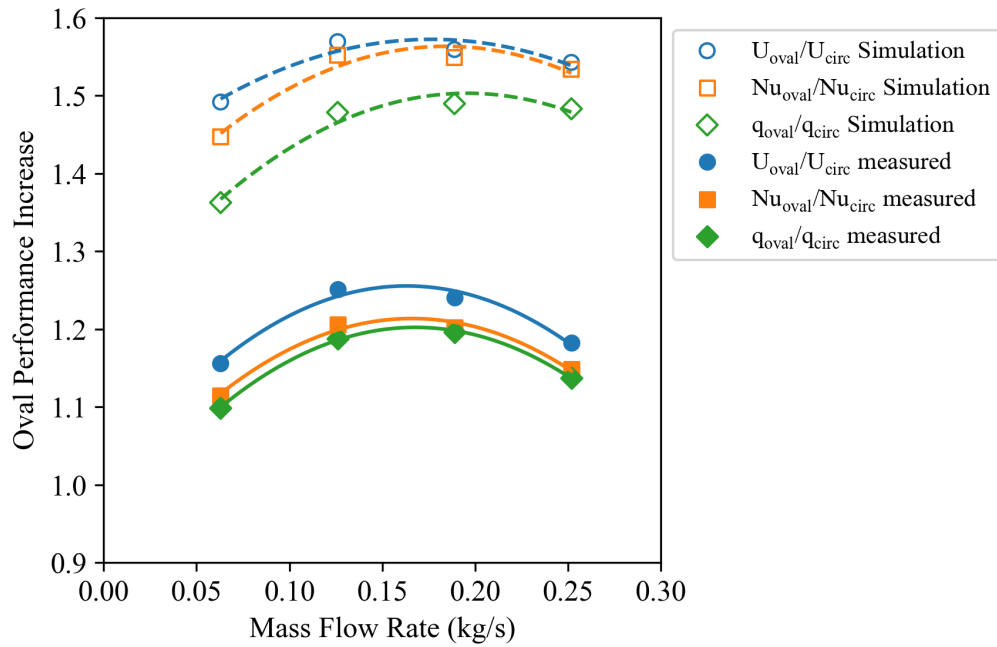


Figure 63: The trends in performance increase between the simulation and the experiment are similar with the most drastic improvement occurring at approximately 0.17 and 0.18 kg/s for the measured and simulated data sets respectively.

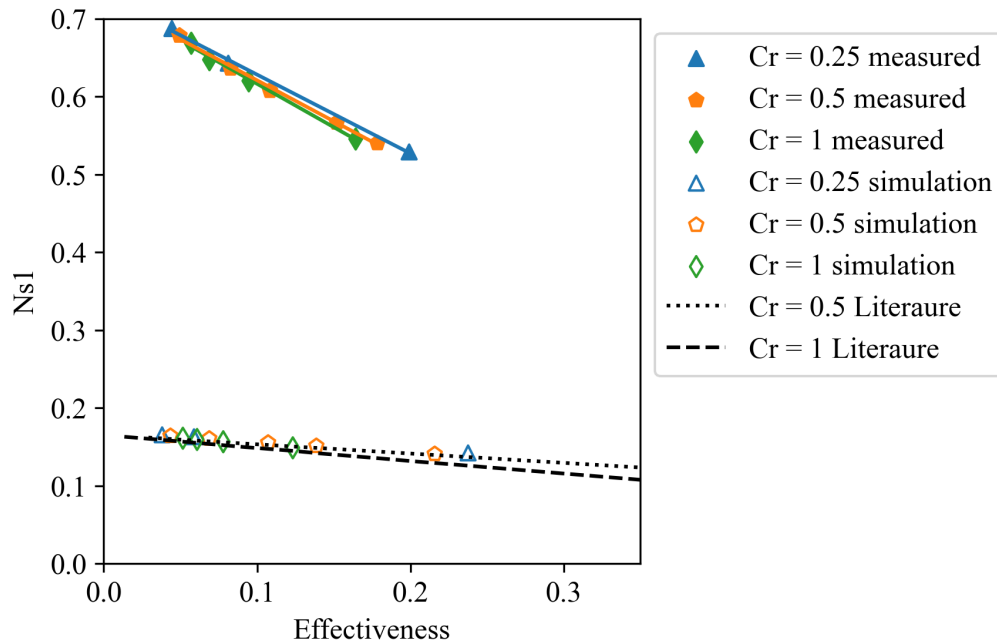


Figure 64: The calculated entropy generation numbers for the circular HX experiment are significantly higher than the CFD results. This indicates that real-life losses are not adequately accounted for in the CFD work.

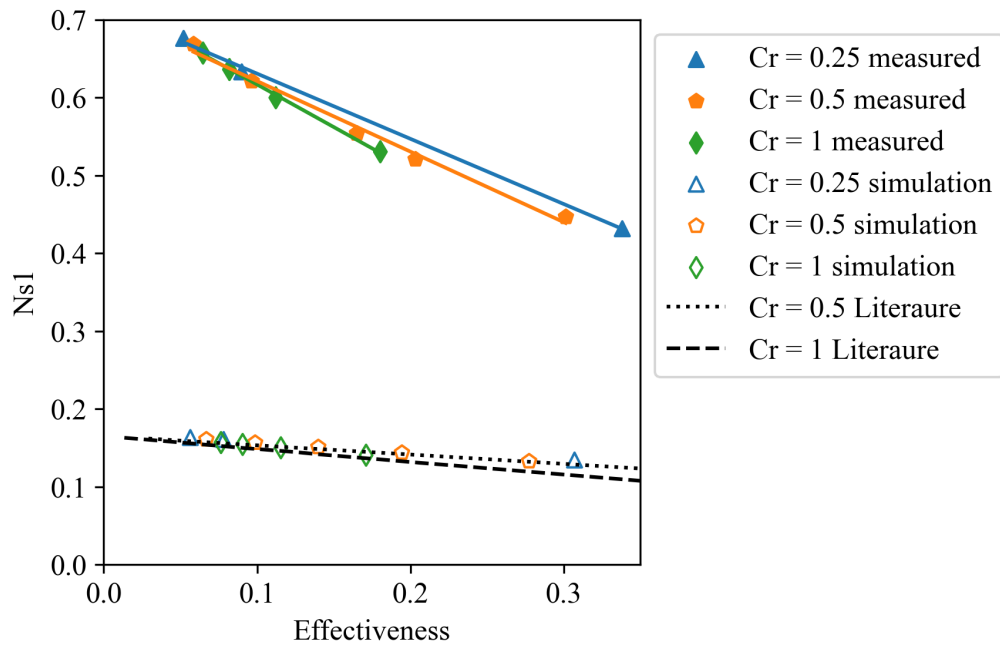


Figure 65: The calculated entropy generation numbers for the oval twisted HX experiment are significantly higher than the CFD results. This indicates that real-life losses are not adequately accounted for in the CFD work.

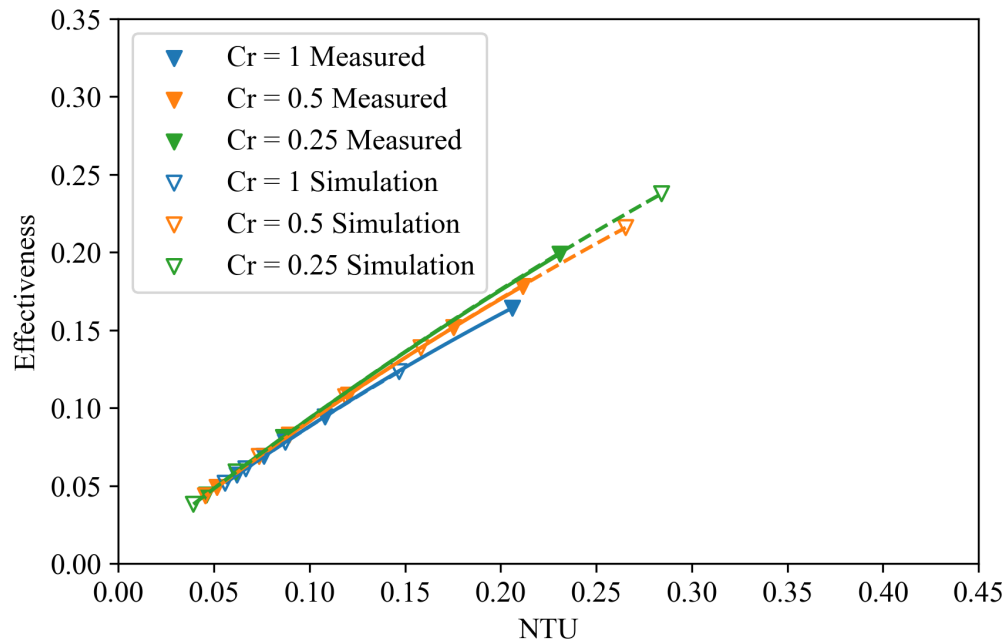


Figure 66: The effectiveness vs NTU curves for the circular geometry HX follow the same trends set forth in the CFD work. The CFD data over approximates the improvement in effectiveness vs NTU curves.

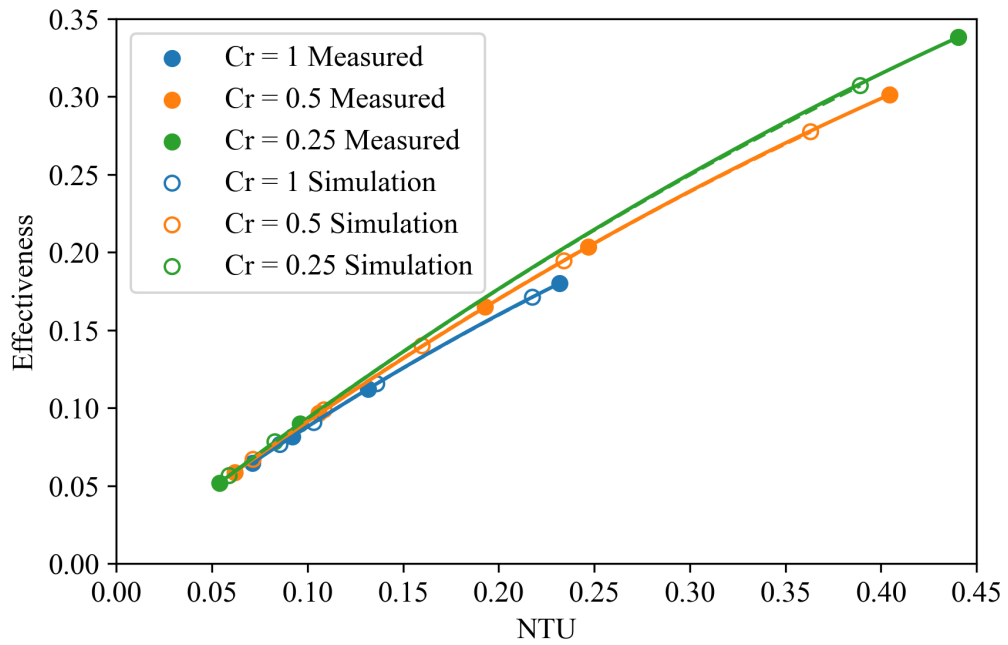


Figure 67: The effectiveness vs NTU curves for the oval twisted geometry follow the same trends set forth in the CFD work. The CFD data under approximates the improvement in effectiveness vs NTU curves.